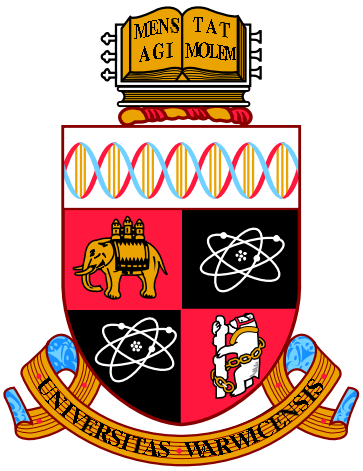

Medical Image Segmentation using Edge-Based Active Contours

by

Alaa Omar Khadidos

Thesis

Submitted to the University of Warwick

for the degree of

Doctor of Philosophy

Department of Computer Science

August 2016

THE UNIVERSITY OF WARWICK

Abstract

The main purpose of image segmentation using active contours is to extract the object of interest in images based on textural or boundary information. Active contour methods have been widely used in image segmentation applications due to their good boundary detection accuracy. In the context of medical image segmentation, weak edges and inhomogeneities remain important issues that may limit the accuracy of any segmentation method formulated using active contour models. This thesis develops new methods for segmentation of medical images based on the active contour models. Three different approaches are pursued:

The first chapter proposes a novel external force that integrates gradient vector flow (GVF) field forces and balloon forces based on a weighting factor computed according to local image features. The proposed external force reduces noise sensitivity, improves performance over weak edges and allows initialization with a single manually selected point.

The next chapter proposes a level set method that is based on the minimization of an objective energy functional whose energy terms are weighted according to their relative importance in detecting boundaries. This relative importance is computed based on local edge features collected from the adjacent region inside and outside of the evolving contour. The local edge features employed are the edge intensity and the degree of alignment between the images gradient vector flow field and the evolving contours normal.

Finally, chapter 5 presents a framework that is capable of segmenting the cy-

toplasm of each individual cell and can address the problem of segmenting overlapping cervical cells using edge-based active contours. The main goal of our methodology is to provide significantly fully segmented cells with high accuracy segmentation results.

All of the proposed methods are then evaluated for segmentation of various regions in real MRI and CT slices, X-ray images and cervical cell images. Evaluation results show that the proposed method leads to more accurate boundary detection results than other edge-based active contour methods (snake and level-set), particularly around weak edges.

Acknowledgments

The journey of completing my PhD research has significant influences on my life. It taught me the meaning of responsibility and perseverance. This journey was made possible because of the support, guidance and encouragement I got from many individuals.

I would like to thank all the people who contributed in some way to the work described in this thesis. First and foremost, I thank my academic advisors, Professor Chang-Tsun Li and Dr. Victor Sanchez, for accepting me into their group. During my studies, they supporting my attendance at various conferences, engaging me in new ideas, demanding a high quality of work in all my endeavors and for being a great friends. Additionally, I would like to thank my committee members Professor Nasir Rajpoot and Professor Tony Pridmore.

I would also like to thank the colleagues at the University of Warwick, Dr. Yu guan, Dr. Xingjie Wei, Dr. Yi Yao,Dr. Ruizhe Li, Mr. Ning Jia, Mr. Xin Guan,Mr. Xufeng Lin, Mr. Qiang Zhang, Mr. Roberto Leyvac, Mr. Shan Lin, Mr. Ching-Chun Chang and Mr. Bo Wang for their support they gave me during all these years.

A special acknowledgments go to Dr. Alia Alfi. I have always been able to turn to you when I have needed a listening ear, a dissenting opinion, or someone to gauge the spiciness of some food. Our friendship was strong before and I hope it will continue to be as strong in the future. My deepest gratitude goes to Ms. Olfat Mirza, Mr. Ayman Qahmash, Mr. Mazen Alzaydi and Dr. Daniel onah, you have all become my best friends. We have seen and helped each other through both good times and bad. I will always remember the great conversations we had over lunch.

ACKNOWLEDGMENTS

Furthermore, I would like to thank my friend Dr. Khaled Alyoubi for all the times we spent together in the UK.

A special thank go to my mother Ms. Foziyah Algamdi. You have encouraged my academic interests from day one, even when my curiosity led to incidents that were kind of hard to explain. Thank you. I also owe a great thank to my twin bother Dr. Adil Khadidos for his unconditional support during the last four years and at any stage of my life so far, understanding and encouragement throughout my life. My warmest thanks to the rest of my family.

I would like to dedicate this work to those who left a deep touch in my life. Their love, constant support and encouragement made me what I am.

Declarations

I hereby declare that this dissertation entitled ***Medical Image Segmentation using Edge-Based Active Contours*** is an original work and has not been submitted for a degree or diploma or other qualification at any other University

Coventry, United Kindom.

Contents

List of Tables

List of Figures

LIST OF FIGURES

Abbreviations

MRI	Magnetic Resonance Imaging
CT	Computed Tomography
GVF	Gradient Vector Flow
PCM	Possibilistic C-Means
FCM	Fuzzy C-Means
CN-GGVF	Component-Normalized Generalized-GVF
SGVF	Sigmoid Gradient Vector Flow
GVC	Gradient Vector Convolution
PDE	Partial Differential Equations
PBLS	Phase-Based Level Set
HAC	Harmonic Active Contours
LLIF	Local Likelihood Image Fitting
CoD	Centers of Divergence
PIG	Poisson Inverse Gradient
BGrad	Balloon and Image Gradient
DSC	Dice Similarity Coefficient
JC	Jaccard Coefficient
RD	Reaction Diffusion
LSD	Level Set Diffusion

ABBREVIATIONS

DRLSE	Distance Regularized Level Set Evolution
LSF	Level Set Function
SDF	Signed Distance Function
Pap	Papanicolaou
HPVs	Human Papillomaviruss
EENCC	Edge-Enhancement Nucleus and Cytoplast Contour
MSER	Maximally Stable Extremal Regions
EDF	Extended Depth of Field
FOVs	Different Fields of View
TP	True Ppositive
FN	False Negative
FP	False Positive

Chapter 1

Introduction

The aim of computer vision is to enable computers to see and sense like a human. Research related to computer vision started in 1970s, and it is still being investigated today as a relatively new discipline. Computer vision is considered a branch of artificial intelligence which intends to simulate human behaviour. This gives computer systems the ability to perform functions which normally require human intelligence, such as learning and problem solving. Researchers in the field of artificial intelligence have attempted to integrate computer science and cognitive psychology. Due to the difficulty of integrating human intelligence and cognitive psychology, a computation stream offers an alternative path to more intelligent machine behaviour.

Computer vision overlaps with other fields such as pattern recognition, image processing, image analysis and computer graphics. Although there is no clear distinction between image processing, image analysis, and computer vision, they are usually viewed as being on a processing continuum in hierarchical form. The processing on the lower level of this hierarchy involves simple operations such as contrast enhancement, noise filtering, and image sharpening, and the inputs and outputs of this level are images. The mid-level processing includes image analysis or image understanding, which involves segmentation and pattern classification [1]. On this level, the input is an image, and the outputs are characteristics extracted from the input image. These characteristics can be edges, contours or identities of

individual objects. Algorithms such as object recognition, segmentation, image coding and robot vision are found on the highest level of the processing hierarchy. The algorithms used in training a system to recognise or classify an object are considered to be computer vision [1].

The number of publications about computer vision is regularly increasing. In industry, computer vision is frequently used for supporting a manufacturing process, especially in quality control. Other applications of computer vision are, for example, surveillance, image databases, virtual reality, robotics, and security. Perhaps one of the most important uses of computer vision is in medical image analysis. Here the image could be in the form of magnetic resonance imaging (MRI), computed tomography (CT), x-ray, ultrasound images, and so on. This thesis will offer a detailed discussion about the technologies used in image segmentation and with propose novel segmentation methods based on active contours.

1.1 Image Segmentation

Image segmentation is a long standing problem in computer vision. In most image segmentation tasks, individual objects need to be separated from the image. The description of those objects then can be transformed into a form suitable for computer processing. The method of image segmentation is to organise the image content into semantically related groups, which are connected and homogenous according to some properties such as texture, colour and intensity.

Two main approaches exist in image segmentation, the edge-based segmentation and region-based segmentation. Edge-based segmentation is able to partition an image on the basis of discontinuities among various sub-regions, while region-based segmentation does a similar function based on the uniformity of a desired property within a sub-region. Figure 1.1 shown an example of region-based and edge-based segmentation.

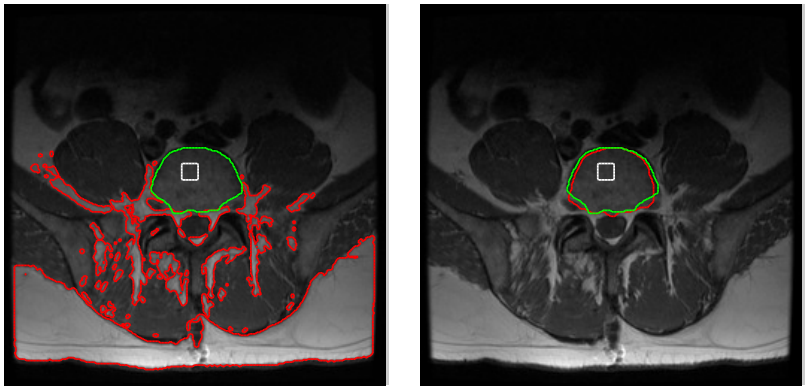

(a) (b)

Figure 1.1: An MRI slice of an abdominal axial cross sectional view of human body. (a) Example of Region-based segmentation obtained by Kimmel [67]. (b) Example of Edge-based segmentation obtained by the proposed method in Chapter 3 . The white curves denote the initial contours, the red curves represent the final contour and the green curves represent the ground truth.

1.1.1 Edge-based Segmentation

Edge-based segmentation looks for discontinuities with regard to the intensity of the image. The precise meaning of this process is more edge detection or boundary detection rather than the literal meaning of image segmentation. The boundary between two regions with relatively distinct properties can be defined as an edge. The presumption behind edge-based segmentation is that all sub-regions within a certain image are uniform so that the change between two sub-regions can be determined on the basis of discontinuities alone. Despite this presumption being invalid, region-based segmentation, discussed in the following section, presents more reasonable segmentation results.

Essentially, the concept behind a majority of edge-detection techniques is the computation of a local derivative operator. The gradient vector of an image $I(x, y)$, given by:

$$\nabla I = \begin{bmatrix} \partial I/\partial x \\ \partial I/\partial y \end{bmatrix}, \tag{1.1}$$

where this is obtained by the partial derivatives $\partial I/\partial x$ and $\partial I/\partial x$ for all pixel locations. The local derivative operation can be performed by convolving an image with kernels, as shown in Figure 1.2.

(a) (b)

Figure 1.2: Examples of gradient kernels along: (a) vertical direction, (b) horizontal direction.

The first derivative magnitude is provided by:

$$|\nabla I| = \sqrt{(\partial I/\partial x)^2 + (\partial I/\partial y)^2}. \tag{1.2}$$

The Laplacian operator of an image function $I(x, y)$ is the sum of the second-order derivatives, defined as:

$$\nabla^2 I = \frac{\partial^2 I}{\partial^2 x} + \frac{\partial^2 I}{\partial^2 y}. \tag{1.3}$$

The overall utilisation of the Laplacian operator is in determining the location of edges with the use of zero-crossings [2]. One of the disadvantages of the gradient operation is the noise sensitivity, and as a second-order derivative, the Laplacian operator is even more sensitive to noise. A different option here is to convolve the image with a Laplacian operator of a Gaussian (LoG) function [3]. Thus the two-dimensional Gaussian function can be given by:

$$G(x, y) = \frac{1}{2\pi\sigma^2} \exp(-\frac{x^2 + y^2}{2\sigma^2}), \tag{1.4}$$

where σ is the standard deviation. The LoG function produces smooth edges as the Gaussian filtering provides a smoothing effect [3].

Only those images that have a sharp intensity transition and a comparatively low level of noise are able to facilitate edge detection using gradient operations.

As a result of its sensitivity to noise, a smoothing operation is usually required as a pre-processing technique to eliminate the noise; consequently, the smoothing effect blurs the edge information. However, the computational cost of the edge detector techniques for edge-based segmentation is relatively low compared to other segmentation methods. This is because the computation can be done by a local filtering operation.

1.1.2 Region-based Segmentation

Region-based segmentation looks for equality inside a sub-region based on a desired property (e.g., colour, texture, and intensity). Clustering techniques, which is based on pattern classification, have similar objectives and can be applied for region-based segmentation. [4].

A technique that is used to merge pixels or small sub-regions into more substantial sub-regions is referred to as region growing [5]. Pixel aggregation, for example, is the simplest implementation of this approach [2]. This approach begins with a series of seed points, and these seed points grow by appending neighbouring pixels if they satisfy the given criteria. An example of pixel aggregation is shown in Figure 1.3.

$\underline{8}$	7	2
9	6	1
$\underline{2}$	3	4

(a)

8	8	2
8	8	2
2	2	2

(b)

Figure 1.3: Pixel aggregation: (a) Image with seeds underlined, (b) segmentation result with $\tau = 3$.

Segmentation begins with two initial seeds and then the regions grow if they satisfy the criterion:

$$|I(x, y) - I(seed)| < \tau. \tag{1.5}$$

Regardless of the simple nature of the algorithm, a number of essential and funda-

mental issues exist within region growing. These include selecting the initial seed and relevant properties to grow the regions. The selection of the initial seeds can often be based on the nature of applications or images. For instance, the region of interest is usually brighter than the background. In such a situation, the selection of the brighter pixels as the initial seeds presents the most sensible choice. However, region-based segmentation may produce over-segmented or poor segmentation results.. This mainly due to over-merging the sub-regions with blurry boundaries.

The problem to be solved determines the level of segmentation needed. Usually, the segmentation stops when the region of interest in the application has been detached. As a result of the property of this problem dependence, autonomous segmentation becomes one of the most difficult tasks in image analysis. The segmentation problem is even more complicated when the image is subject to noise or poor resolution. Image segmentation can proceed in three different ways:

1. **Manual segmentation**: This can be done manually by grouping a number of pixels which shared the same intensity. However, if the image is large, then this task become a very time-consuming method. Alternatively, marking the contours of the objects which can be done from the keyboard or the mouse with higher speed but less accuracy. All manual techniques are time-consuming, and human resources are expensive. Geometrical shapes, like squares or ellipses, are useful to approximate the boundaries of the objects. This has been applied for medical purposes; however, the approximations may not be very good.

2. **Automatic segmentation**: This refers to the processes whereby segment boundaries which are allocated automatically by a segmentation algorithm (program). Most algorithms in this category require prior information to carry out the segmentation, and this prior information must be available to the computer program. The resulting boundaries from the program may not be exactly accurate, especially if the training data was sparse.

3. **Semiautomatic segmentation**: This combines the advantages of both manual and automatic segmentation. By giving some initial information about the structures. This includes, for example, thresholding, clustering and active contour methods.

1.2 Medical Image Segmentation

Recent improvements in a wide range of medical imaging technologies have defined anatomical structures and changed how we view the pathological events in the body. Ultrasound X-ray, MRI, nuclear medicine, among other medical imaging technologies captures the structural inside the body in 2D or tomographic 3D images and provide functional information for diagnosis, treatment planning and other purposes. To improve workflow efficiency and to achieve compatibility between imaging systems and other information systems in healthcare environments a standard called Digital Imaging and Communications in Medicine (DICOM) standard is created as the international standard for communication of biomedical diagnostic and therapeutic information in disciplines that use digital images and associated data.

The raw form of medical images is represented by arrays of numbers in the computer, where each layer of this array shows different types of body tissue. Processing and analysis of raw images facilitate the process of extracting meaningful quantitative information to aid diagnosis. Identifies the boundary of objects such as organs or abnormal regions in images is a fundamental problem in medical image analysis. Having segmented organs helps for detecting volume change and shape analysis which it necessary for making a precise therapy treatment plan.

Various segmentation methods have been proposed for image segmentation such as: Thresholding, region growing, edge detection, Markov Random Fields (MRF), graph cut, active contour (or deformable), level sets. Also, significant extensions of these frameworks proposed to improve the efficiency, applicability and accuracy. Among these methods, active contour models have been widely used in

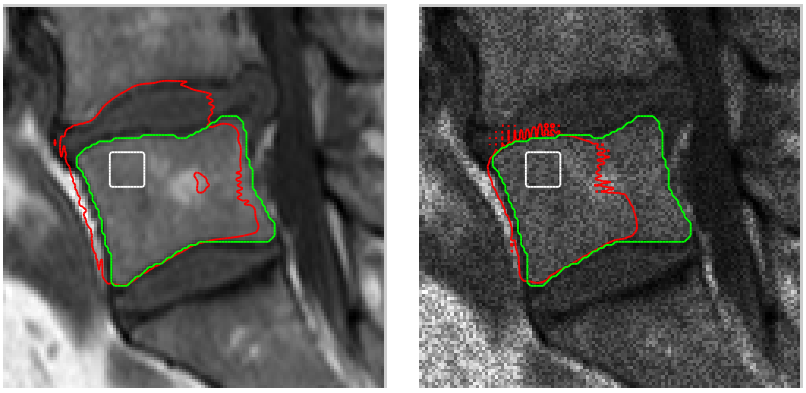

(a) (b)

Figure 1.4: Segmentation results on a MRI slice of a spinal cord. (a) Segmentation result of image with weak edges. (b) Segmentation result of image with high level of noise. The white curves denote the initial contours, the red curves represent the final contour and the green curves represent the ground truth.

medical image segmentation. The active contour model is connectivity-preserving which makes it applicable to the image segmentation problems [6]. Active contours originally proposed by Kass et al. [7] in 1988. Essentially, active contours start with an initial boundary represented in the form of a closed curve. This curve is modified iteratively by inflation or deflation operations according to the application desired. The motion that occurs on the curve by the inflation or the deflation operations is called contour evolution. Those operations are performed by the minimization of an energy function.

Despite intensive research in medical image segmentation using active contours, however, there are still many situations where active contour fail to converge to the desired boundary, especially when the amount of image clutter and noise is high. In such cases, segmentation accuracy may be improved by manually initializing the curve very close to the objects boundary. Depending on the region to be segmented, this initialization process may require the selection of several initial points or snake elements, which may become a tedious and error-prone process in medical images. Also, weak edges, inhomogeneities, limited capture range, and contour leakage have a negative impact on active contour performance and remain important

issues that may hinder the accuracy of any segmentation method formulated using active contour [see Figure 1.4].

1.3 Contributions of Thesis

This thesis proposes novel edge-based active contour methods for medical images that can detect objects' boundaries even when the background has noise or the object is delimited by a mostly weak boundary. The proposed active contour methods are aimed at providing robust segmentation results for complicated cases with non-uniform backgrounds.

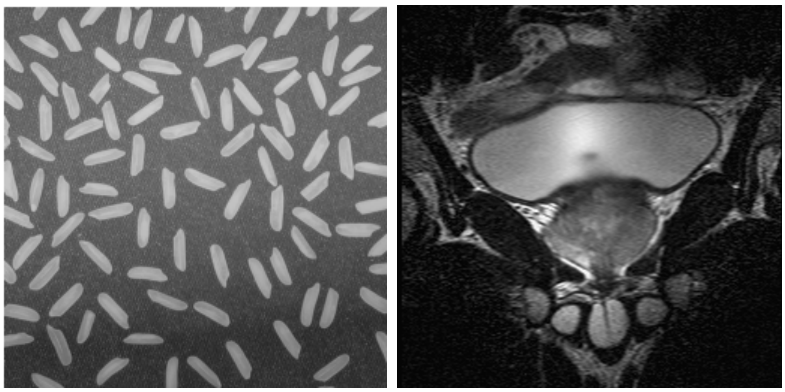

(a) (b)

Figure 1.5: (a) Grey-Scale Image showing a cluster of bacteria present in a fluid having non- uniform texture, darker at the bottom and brighter on the top and center portions. (b) MRI of the pelvis with a slowly varying background variation.

The main contributions are summarised in details as follows:

1. We propose a novel external force, which integrates a gradient vector flow (GVF) field force and a balloon force. This external force is insensitive to snake initialization and may prevent snake leakage. We also propose a mechanism to automatically terminate the contour's deformation. Evaluation results on real MRI and CT slices show that the proposed approach attains higher segmentation accuracy than snakes using traditional external forces, while allowing initialization using a limited number of selected points.

2. Motivated by the previous contribution which deforms the contour using a weighting function based on local image features. We propose a level set method for segmentation of medical images with noise and weak edges. The proposed level set evolution is based on the minimization of an objective energy functional whose energy terms are weighted according to their relative importance in detecting boundaries. This relative importance is computed based on local edge features collected from the adjacent region located inside and outside of the evolving contour. The local edge features employed are the edge intensity and the degree of alignment between the image's gradient vector flow field and the evolving contour's normal. Novelties about how local edge information is used in our method are as follows:

   (a) Our method measures the alignment between the evolving contour's normal direction of movement and the image's gradient in the adjacent region located inside and outside of the evolving contour. This measurement is often used as an additional energy term in the energy functional.

   (b) Our method also considers the average edge intensity in the adjacent region located inside and outside of the evolving contour. This allows us to minimize the negative effect of weak edges on the segmentation accuracy.

   (c) Our method uses all of the collected local edge information to compute a single value that serves as a weight to control the influence of forces. This minimizes leakage in areas where weak edges exist.

   We evaluate the proposed method for segmentation of various regions in real MRI and CT slices, as well as Xray images. Evaluation results show that the proposed method leads to more accurate boundary detection results than other edge-based level set methods, particularly around weak edges.

3. We propose a framework capable of segmenting the cytoplasm of each indi-

vidual cell and dealing with the problem of segmenting overlapping cervical cells using edge-based active contours. The main goal of our methodology is to provide significantly fully segmented cells with high accuracy. Due to the challenges involved in delineating cells with severe overlap and poor contrast, most current methods fail to offer a complete segmentation. Although the previous contributions provided promising results in segmenting medical images, however, we can not apply them directly to overlapping cells. Instead, we explore another way of applying edge-based active contour. The proposed framework initially performs a segmentation to cell clumps. Then cell segmentation is performed using a patch-based active contour.

The proposed framework uses a patch-based approach where an active contour detects, on a patch-by-path basis, the cytoplasm boundary of each overlapping cell. It also uses a supervised classifier to separate cell clumps from the background and to detect the nuclei of each cell in each clumps. The centriod of each detected nuclei is used to define the major possible region of each cell in the clump. Then, the framework proceeds to allocate the cytoplasm region of each cell. The active contour within the patch is deformed under the influence of GVF forces computed based on local edge features collected from the patch region. Experimental results showed that the proposed framework outperforms other state-of-the-art approaches, in terms of segmentation accuracy

1.4 Thesis Outline

The thesis is organized into 6 Chapters. In each chapter, a review of related techniques is presented. The individual chapters of this thesis are structured as follows:

- Chapter 2 provides an overview of popular methods and techniques given the problem of object segmentation.

- Chapter 3 presents active contours based on weighted gradient vector flow and balloon forces for medical image segmentation. Experimental results are presented and the performance of this method is compared to related states-of-art segmentation algorithms.

- Chapter 4 presents weighted level set evolution based on local edge features for medical image segmentation. Experimental results of this method are presented and the performance of this method is compared to related stats-of-art segmentation algorithms.

- Chapter 5 presents a patch-based segmentation framework for cervical cell images using local information for overlapping cervical cells. Experimental results are presented and the performance of this method is compared to related states-of-art segmentation algorithms.

- Chapter 6 concludes the thesis.

1.5 List of Publications

The list of publication arising from my PhD research on medical image segmentation using edge-based active contours is as follows:

1. A. Khadidos, V. Sanchez and C.-T. Li, "Contours Based on Weighted Gradient Vector Flow and Balloon Forces for Medical Image Segmentation," in Proc. IEEE International Conference on Image Processing, Paris, France, 27 - 30 Oct 2014.

2. A. Khadidos, V. Sanchez and C.-T. Li, "Active Contours with Weighted External Forces for Medical Image Segmentation," in Proc. 18th Annual Conference in Medical Image Understanding and Analysis (MIUA), London, UK, 9 - 11 Jul 2014.

3. A Khadidos, V. Sanchez, and C-T Li, Weighted Level Set Evolution Based on Local Edge Features for Medical Image Segmentation, IEEE Transactions on Image Processing (accepted and to appear in 2017).

4. A. Khadidos, V. Sanchez and C.-T. Li, "Patch-based Segmentation of Overlapping Cervical Cells Using Active Contour with Local Edge Information," in Proc. IEEE International Conference on Acoustics, Speech and Signal Processing, New Orleans, USA, 5 - 9 March 2017.

The chapters of this thesis are related to the aforementioned papers, as listed in Table 1.1.

Table 1.1: Thesis chapters and the corresponding publications.

Thesis Chapters	**Cameras**	**Content**
Chapter 3	Paper 1	Contours Based on Weighted Gradient Vector Flow and Balloon Forces for Medical Image Segmentation
Chapter 3	Paper 2	Active Contours with Weighted External Forces for Medical Image Segmentation
Chapter 4	Paper 3	Weighted Level Set Evolution Based on Local Edge Features for Medical Image Segmentation
Chapter 5	Paper 4	Patch-based Segmentation of Overlapping Cervical Cells Using Active Contour with Local Edge Information

Chapter 2

Literature Review

2.1 Image Understanding

An image can be represented with a three dimensional matrix $w \times h \times n$, where w and h denote the width and height of an image, and n is the number of channels in an image (i.e., red, green, and blue). In this thesis, the images are represented in grey levels. The total pixel count of an image is defined as $w \times h$. Image understanding problems are primarily focused on the areas of object detection, segmentation, and class segmentation. A brief summary of these areas is provided in the following subsections.

2.1.1 Object Detection

The location of a target object within the data of an image is part of the object detection process. Indeed, the process of object detection compares the image or part of an image to a model that contains prior knowledge concerning the target object. The mapping and counting of such targeted objects within the dataset can be obtained using detection points. Of all the various approaches, the simplest is template matching [8]. Herein templates that represent a target object in a number of different configurations, scales, and orientations are convolved over the original data so that a similarity measure can be carried out. Furthermore, a threshold is then applied to the subsequent similarity measure in order to provide detection points. Though the

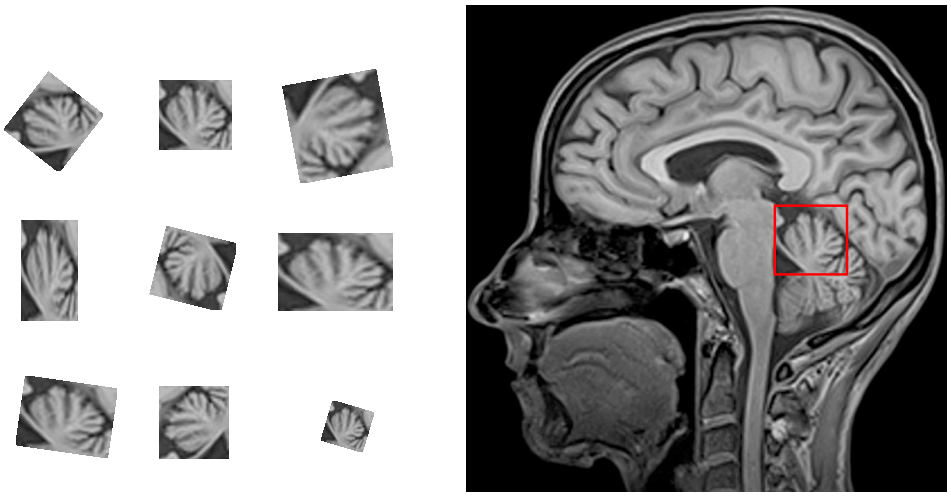

(a) (b)

Figure 2.1: (a) Templates of a target object in different scales and orientations. (b) Electronic board image where the red box locates the targeted object.

application of the temple matching approach is elementary and straightforward, it proves efficacious for certain applications, it may also be inefficient because of the large size of the search space. Example of template matching algorithm is show in Figure 2.1. Another approach is to select a set of features that are able to differentiate the target object and then extract these features from the image and utilise a classifier for the detection stage. Compared to the template matching approach, this process is more robust, although the classifier training process and feature selection are generally required for each new application or dataset [9].

2.1.2 Object Segmentation

The aim of object segmentation is to separate those objects of interest from any background scenes. In this manner, segmentation takes place with the grouping of those pixels that share similar characteristics. Segmentation methods vary from completely basic, such as the utilisation of the thresholding [10], clustering [11], and region growing [12], to methods that consider spatial characteristics through the explicit modelling of object boundaries [13, 14]. An example of image segmented by

a thresholding method is shown in Figure 2.2.

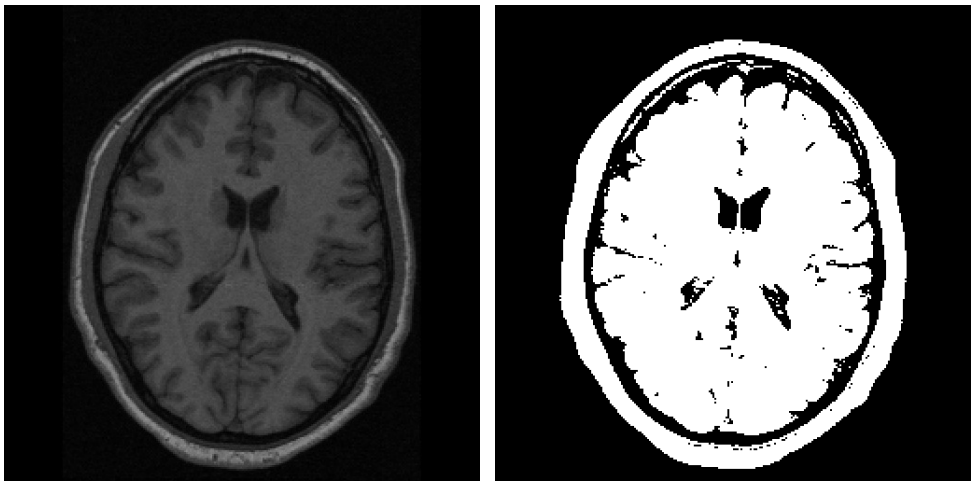

(a) (b)

Figure 2.2: (a) MRI image of the brain. (b) The binary segmentation image obtained by a thresholding method.

The performance of a segmentation algorithm is highly dependent on the feature that is mainly utilised to identify the target object; this is considered application and data dependent [1]. Object segmentation can be performed in a semi-automated fashion by requesting the user provide the initial labels or fully-automated using pre-trained algorithms that are able to autonomously perform the segmentation [15, 16]. More information is contained in object segmentation than in object detection points, which allow further assessment of object segments. For instance, rather than detecting individuals, human segments permit the recognition of human identity and tracking [17]. Vehicle matching [18] can be implemented rather than estimating the traffic volume and rather than counting the tree crowns, tree crown delineation allows further analysis for species classification [19, 20].

Figure 2.3 shows an image segmented using a Bayes algorithm.

2.1.3 Object Class Segmentation

The aim of object class segmentation is to assign semantic labels to each pixel in the image. The task of object class segmentation is achieved with the use of pre-trained

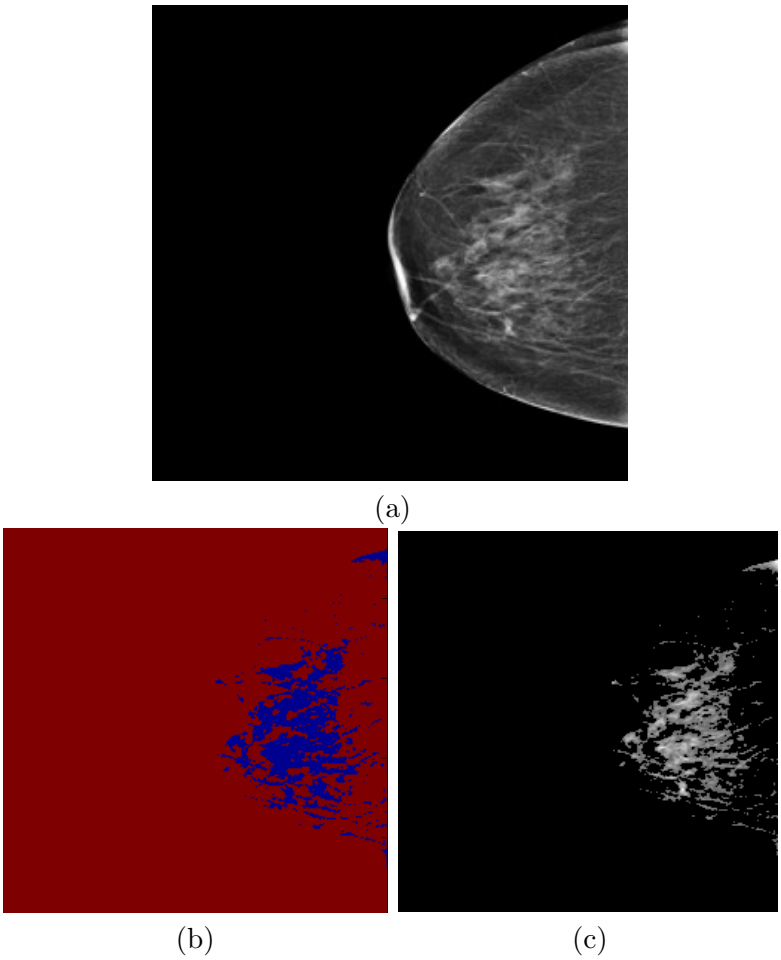

Figure 2.3: (a) A mammogram image of a dense breast. (b) The cluster of fibroglandular tissue region obtained by Bayes algorithm. (c) Segmented fibroglandular tissue.

algorithms, and, as part of the algorithm design stage, the features must be carefully selected to best discriminate the various classes. The most common and general features used are colour, shape, and texture [21]. To improve the performance in specific applications, more features, such as object detector responses, super-pixel properties, and object correlations, can also be used [16, 22, 23]. However, deciding which feature descriptors should be used and how important the features are among each other is a difficult task. This task can be done with experiments and the application of cross validations [23–25], although this process needs to be repeated

for different datasets.

2.2 Image Segmentation: Methods

Image segmentation has been a well-researched field in the past. Indeed, thousands of segmentation techniques have been proposed so far there, yet there is no a single technique which can be used for any type of images. Therefore, based on the characteristics of the image a particular segmentation technique is used [26]. This section briefly reviews the general concepts of existing image segmentation methods.

2.2.1 Clustering

Clustering is the most common form of unsupervised learning, in which classification is done between pixels, and those pixels are grouped to form clusters. Each cluster is a collection of similar pixels, and those that are dissimilar belong to different clusters. The clusters are formed under certain criteria, such as texture, colour, and size. The similarity measure and its implementation play a major role in the quality of the results of the clustering methods.

2.2.2 Region Growing

In region growing algorithms, the growth of a region takes place whenever its interior is homogeneous based on certain features, such as colour, texture, or intensity. In implementation, the strategy follows typical region growing in which the region grows by adding similar neighbours. Region growing [27] is one of the simplest algorithms for region-based segmentation. The traditional implementation begins by selecting an initial point. This is usually called a seed pixel. Based on a certain homogeneity criterion, the region grows by adding similar neighbouring pixels. The size of the region is then increased step by step. Deciding whether a pixel belongs to the growing region or not is heavily based on pixel homogeneity. Edge map of the region can also provide additional criteria such as the condition of the contour pixel

when deciding to aggregate it. The process of growing reaches the boundary of the region when there is no pixel aggregated, and the growth of the region is going to stop.

2.2.3 Split-and-Merge Algorithms

Unlike the previous method, region merging methods address the problem of image segmentation from the bottom up, where each pixel in the image is considered to be a seed point. In the case of two neighbouring pixels being similar enough according to some criterion, they will merge into a single region. Similarly, if two adjacent regions share the same properties, they will be merged into one region. This process is repeated until merging becomes impossible.

2.2.4 Watershed

The watershed algorithm [28, 29] is a morphology-based segmentation method [30–32]. The watershed transform is one of popular segmentation methods and was initially proposed by Digabel and Lantuejoul [33]. Watershed transformation methods concede the image as a topographical map with mountains or valleys, where the intensity of a pixel is treated as its altitude. The high-value regions appear as mountains, and the low value regions appears as valleys. The map is then flooded with its local minima. Each water basin fills up from its minima and the dam is formed where two basins converge. Once the water reaches the level of the highest peak, the flooding process is then stopped. The set of all dams defines the so-called watershed.

2.2.5 Graph Partitioning Methods

Graph-based approaches have been widely used in the last decade. This approach considers the image segmentation as a graph partition problem, where an image is represented as a weighted undirected graph. Each node of the graph represents the image pixel and each edge represents a pair of nodes. The similarity measurement

between pairs of nodes is called weight. To group the pixels, a graph partition is sought to separate the nodes into a disjoint set, so that the similarity among the nodes in the set is high, while the similarity across different sets is low.

2.2.6 Active Contours (Deformable Models)

Deformable models are one of the most used methods in medical image segmentation. A deformable model can be described as a technique for defining region boundaries by using curves or surfaces close to the edges that deform under the effect of forces. Deformable models, including active contours (2-D) and active surfaces (3-D) are closed contours or surfaces which are able to expand or contract over time, within an image, and conform to specific image features [34].There are two main techniques of deformable models in the literature, parametric active contours and geometric active contours. The parametric model represents curves and surfaces explicitly in their parametric forms during deformation. The geometric model is based on the theory of curve evolution in time, according to intrinsic geometric measures of the image, and is numerically implemented via level set algorithms. As image segmentation methods, there are two types of active contour models based on the force that evolves the contours: edge- and region-based. Edge-based active contours, are based on the image gradient, using edge detector output to deform the contour toward the object boundary. This model is closely related to the edge-based segmentation which have been discussed in section 1.1.1. Region-based active contours, instead of searching geometrical boundaries, using statistical information of image intensity within a region.This model is closely related to the region-based segmentation methods which have been discussed in section 1.1.2.

2.2.6.1 Snakes

The first model of active contour was proposed by Kass *et al.* [7]. The algorithm is called “snakes” because the contour motion during the evolution toward the object

resembles snake movement. Let us define a contour parameterized by arc length s as

$$C(s) = \{(x(s), y(s)) : 0 \leq s \leq L\}, R \rightarrow \Omega_I \tag{2.1}$$

where L denotes the length of the contour, Ω_I denotes the entire domain of an image $I(x, y)$ and $C(s)$ is a curve sampled and represented by a set of discrete points, these sample points are referred to as snake elements. $x(s)$ and $y(s)$ are a continuous function representing the value of x and y coordinates. Note that the scalar parameter s is between 0 and 1, i.e. the first point in a planar curve is represented as $x(0), y(0)$, while the last point is represented as $x(1), y(1)$. For closed curves the case is different, the first and last points are the same i.e. $x(0) = x(1)$ and $y(0) = y(1)$.

The main principle behind snakes is to model the movement of a dynamic curve towards an object's boundary under the influence of internal and external forces. The internal forces depend on the shape of the contour, where the external forces depends on image properties i.e. gradient. An energy function $E_{snake}(C)$ can be defined on the contour such as:

$$E_{snake}(C) = E_{int} + E_{ext} \tag{2.2}$$

where E_{int} and E_{ext} respectively denote the internal energy and external energy. Internal forces control the smoothness of the curve, while external forces lead the curve to the boundary until convergence is achieved.

The internal energy function determines the regularity of the curve. A common choice for the internal energy is a quadratic functional given by:

$$E_{int} = \int_0^1 (\alpha \left|C'(s)\right|^2 + \beta \left|C''(s)\right|^2) ds \tag{2.3}$$

where α and β are weighting parameters that control the snake's tension and rigidity, respectively. C' and C'' are the first and second derivative of C. The external energy

term which controls the contour evolution depending on the image $I(x, y)$, be defined as:

$$E_{ext} = \int_0^1 E_{img}(C(s))ds \tag{2.4}$$

where $E_{img}(x, y)$, denotes a scalar function defined on the image plane. Therefore the image information, such as edges, attracts the snake toward object boundaries. A common example of the edge attraction function is a function of image gradient, given by

$$f(x, y) = |\nabla [G_\sigma(x, y) * I(x, y)]|^2 \tag{2.5}$$

where G_σ denotes a 2D Gaussian filter [see Equation 1.4] with standard deviation σ, $*$ denotes a linear convolution, ∇ denotes the gradient operator and $I(x, y)$ denotes the image.

In numerical experiments, a set of snake elements are defined in the initial stage on the image plane and then the next position of those elements is determined by the external energy. The connected elements of a snake are considered as the contour. Basic form of snake is shown in Figure 2.4.

There are number snakes elements in the image, those elements form a contour around the object. The snakes elements are initialized at further distance from the boundary of the object. Then, each point moves towards the optimum coordinates, where the energy function converges to the minimum. The snake points eventually stop on the boundary of the object.

Due to the wide variety of object shapes, there are still many situations where snakes fail to converge to the desired boundary, especially when the amount of image clutter and noise is high [35]. In such cases, segmentation accuracy may be improved by manually initializing the curve very close to the object's boundary. Depending on the region to be segmented, this initialization process may require

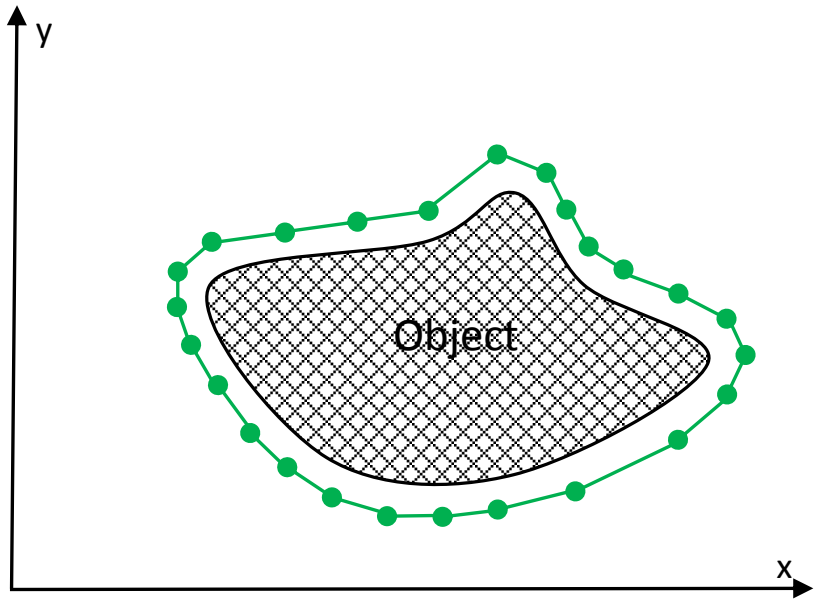

Figure 2.4: Basic form of Snakes. The green dotes represent the snake elements while the green line represents the contour.

the selection of several initial points or snake elements, which may become a tedious and error-prone process, particularly in medical images.

The classical snake limitations, such as noise sensitivity and initialization sensitivity, motivated other snake variations to be introduced. [36–38], including segmentation of medical images [39–41]. The work of Cohen [37] represents one of the initial solutions, which consists of employing an external force to guide the snake to the object's boundary in a similar way a balloon inflates or deflates. These *balloon forces* have been proved to improve convergence when the snake is initialized far from the desired boundary. However, if the strength of the balloon forces is too high, the snake may not detect weak edges resulting in snake leakages. Another important solution is the one proposed by Xu *et al.*, which introduces the gradient vector flow (GVF) field as an external force. The GVF force increases the capture range of the snake, allowing it to conform to concave boundaries. This external force, however, may still fail to accurately converge to the desired boundary if the levels of noise in the image are high [42].

After the introduction of the GVF force, important work has been done to further improve the convergence of snakes. In [35], Zhu *et al.* propose the gradient and direction vector flow (G&DVF) external force, which integrates the GVF field and prior directional information manually provided by the user. In [43], Qin *et al.* propose a new external force called the component-normalized generalized-GVF (CN-GGVF), which improves the detection of concave regions and long and thin indentations.

Yao *et al.* [44] propose the sigmoid gradient vector flow (SGVF) external force, which is obtained by convolving the original image with a sigmoid function before computing the GVF field. This external force, which features a reduced noise sensitivity, is capable of minimizing snake leakages.

Other important solutions that improve convergence of snakes for medical image segmentation include the work in [40, 41]. In [40], Wu *et al.* propose the gradient vector convolution (GVC) field as an external force, which is calculated by convolving the gradient map of an image with a defined kernel. This method is, however, limited to segmenting specific anatomical regions such as the left ventricle in cardiac MRI. Zhang *et al.* [41] propose improvements to the GVF snake by using a combination of balloon and tangential forces. This method is, however, very sensitive to a set of parameters.

The majority of external forces proposed in [35,40,41,43,44] still require that the initial snake be placed close to the desired boundary to improve segmentation accuracy, especially in cases where the amount of image clutter and noise is high, such as in medical images. This inevitably involves manually selecting several initial snake elements. Moreover, they may still fail to accurately drive the snake to the desired boundary around weak edges [45]. However, the most important limitation of snakes is the difficulty in dealing with topological changes during the deformation, such as splitting or merging. This is a useful property for segmenting multiple objects with one curve or segmenting an object with unknown topology. In this

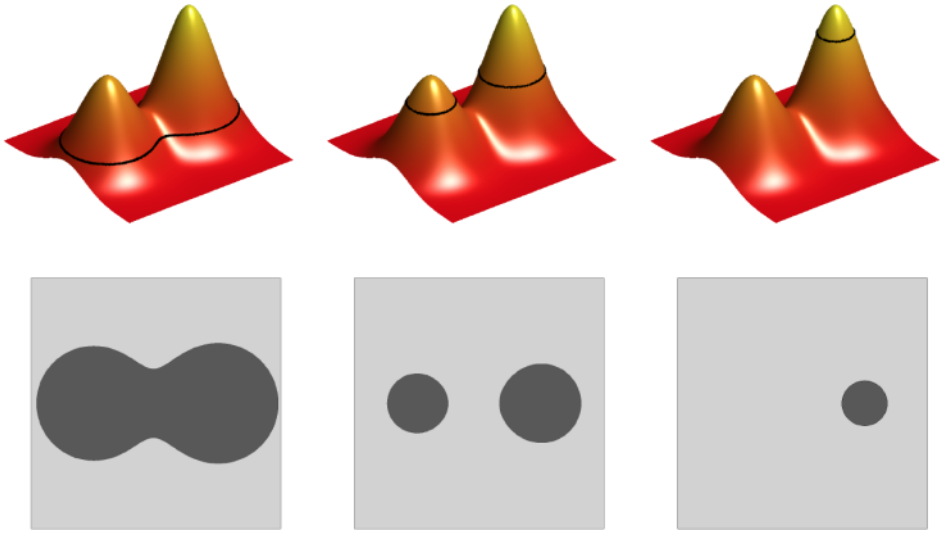

Figure 2.5: : Level set method: (top row) the evolution of the level set function; (bottom row) the evolution of the zero level curve of the corresponding level set function in top row [51].

context some researchers proposed a deformable surfaces for volume segmentation using an efficient reparameterization mechanism to adopts the topology changes during the curve evolution [46, 47].

2.2.6.2 Level-Set

Despite the excellent performance of snakes, however, it has some intrinsic drawbacks, for example, their limitation to adapt to topological changes, especially if the evolution involves splitting or merging the contour; their inability to detect convex contours; their sensitivity to the initialization position [48]; and their high dependency on parametrization. Level set theory has given a solution for this problem [49]. Moreover, it is easy for implementation and lack of parameterization [50].

Geometric, or level set methods, represents the contour of an object as the zero-level set of a higher dimensional function. The 2D contour of an object on image plane is updated when its 3D surface is evolved. The main advantage of level set methods is the flexibility dealing with complex curve behavior, namely the merging and splitting of the contour.

Osher *et al.* [49] propose a level set method which implicitly represents the curve as the zero level of the level set ϕ of a high dimensional function. In parametric active contour models, the contour is represented by a closed planar parametric curve $C(s)$. The curve's normal is defined by $\vec{N} = \{-y_s(s), x_s(s)\}$, where the subscripts denote derivatives, such that the curve's tangent is given by $C_s = \{x_s, y_s\} = \{dx(s)/ds, dy(s)/ds\}$. The deformable curve may then be represented implicitly via a two-dimensional $\phi(x, y)$ defined on the image plane. The function $\phi(x, y)$ is called level set function or the zero level, of $\phi(x, y)$ is defined as the contour, such as

$$C = \{(x, y) : \phi(x, y) = 0\}, \forall (x, y) \in \Omega_I \tag{2.6}$$

where Ω_I denotes the entire image plane. Figure 2.5 shows the evolution of a level set function. While the level set function $\phi(x, y)$ deforms from its initial position, the corresponding set of contours propagates outwards. With this definition, the evolution of the contour is equivalent to the evolution of the level set function i.e. $C(s, t) : [0, 1] \times R^2$, where $t \in [0, \infty)$ is an artificial time generated by the evolution of the initial curve $C_0(s)$ in its inward normal direction $\vec{N}$. For $t > 0$, the curve's evolution equation is given by:

$$C_t = F\vec{N} \tag{2.7}$$

where F is a force function [52]. A formulation of contour evolution using the gradient magnitude of $\phi(x, y)$ was initially proposed by Osher and Sethian [49,53,54], given by

$$\frac{\partial \phi(x, y)}{\partial t} = |\nabla \phi(x, y)| \left(F + \epsilon \kappa(\phi(x, y))\right) \tag{2.8}$$

where ϵ controls the balance between the regularity and robustness of the contour evolution and F represents a constant speed term that pushes or pulls the contour and is often computed based on the curvature:

$$\kappa = \mathbf{div}(\nabla\phi / |\nabla\phi|) \tag{2.9}$$

where $\mathbf{div}(\cdot)$ is the divergence operator [50, 52]. The main purpose of the curvature term is to control the regularity of the contours as the internal energy E_{int} term does in the classic snakes model.

Another form of contour evolution was proposed by Chan and Vese [55]. The length of the contour $|C|$ can be approximated by a function of $\phi(x, y)$ [56, 57], such as

$$Length\{\phi = 0\} = \int_{\Omega_I} H(\phi(x, y)) \, |\nabla\phi| \, dxdy \tag{2.10}$$

where H is the Heaviside function.

$$H(x, y) = \begin{cases} 1, & if \phi > 0 \\ 0, & if \phi \geq 0 \end{cases} \tag{2.11}$$

Since the unit step function produces either 0 or 1 based on on the sign of the input, the derivative of the unit step function produces nonzero only where $\phi = 0$. As a result, the integration shown in Equation (2.10) is equivalent to the length of contours on the image plane. Parameterizing the descent directions by an artificial time t is given by

$$\frac{\partial\phi(x, y)}{\partial t} = \delta(\phi(x, y))k(\phi(x, y)) \tag{2.12}$$

where $\delta(\cdot)$ denotes the derivative of $H(\cdot)$. The contour deforms by the equation above which can be interpreted as the motion by mean curvature minimizing the length of the contour. Therefore, Equation (2.8) is considered as the motion motivated by PDE, while Equation (2.12) is considered as the motion motivated by energy minimization.

Edge-based Active Contours

Most edge-based active contour models consist of two main terms: the regularity term and edge detection term. The regularity term defines the shape of contours, while the edge detection term attracts the contour towards the edges.

Edge-based active contour model was proposed by Caselles *et al.* [48] adding an additional term to the speed function shown in Equation (2.8). This term, which added by Caselles *et al.* , speeds the deformation process of the contour and vanishes when the contour reaches to the object boundary. Similar model proposed by Malladi *et al.* [50, 58] and is given by

$$\frac{\partial \phi(x,y)}{\partial t} = g(I(x,y))(\kappa(\phi(x,y) + F) \left|\nabla \phi(x,y)\right| \tag{2.13}$$

where $g \in [0,1]$ and it is given by

$$g \triangleq \frac{1}{1 + \left|\nabla G_\sigma * I\right|^2} \tag{2.14}$$

where Ω_I, G_σ is a Gaussian kernel with a standard deviation σ, and $*$ denotes a convolution operation. Function g usually takes smaller values at object boundaries than at smooth regions.

The speed of $g(I(x,y))(\kappa(\phi(x,y)) + F)$ moves the contours in the normal direction, and therefore stops on the object boundary, where g vanishes. The curvature term κ maintains the regularity of the contours, while the constant force term F speed the deformation process and evolve the contour toward the object boundary by minimizing the enclosed area [59].

Region-based Active Contours

The majority of edge-based segmentation method have stopping terms that depend on the edge of the object. In the case of noisy images, smoothing is performed on the image with a Gaussian distribution. This process might smooth weak edges

and make the models depending on gradients fail to find the contours. The active contours without edges do not depend on the edge of the object. Basically, this model separates the image into regions based on homogeneity of intensities. The

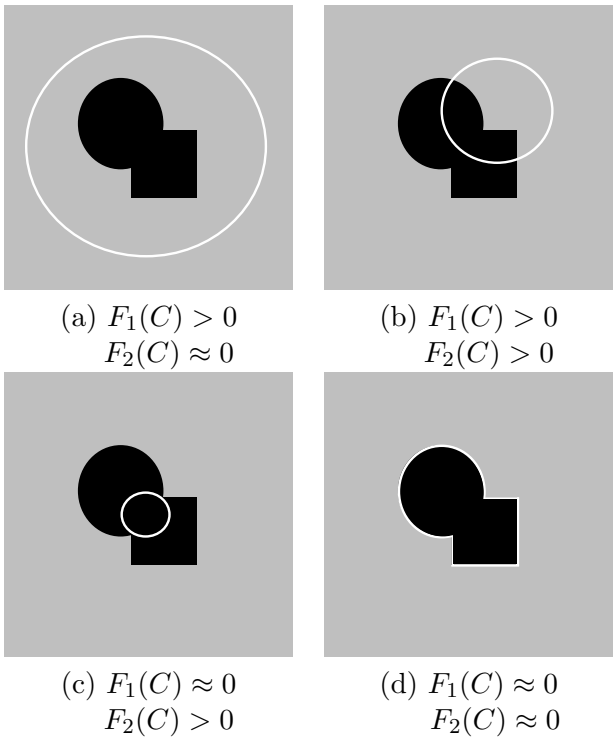

(a) $F_1(C) > 0$ $F_2(C) \approx 0$ (b) $F_1(C) > 0$ $F_2(C) > 0$

(c) $F_1(C) \approx 0$ $F_2(C) > 0$ (d) $F_1(C) \approx 0$ $F_2(C) \approx 0$

Figure 2.6: All possible cases in fitting a curve onto an object. : (a) the curve is outside of the object; (b) the curve is inside the object; (c) the curve contains both object and background; (d) the curve is on the object boundary [55].

region-based active contour models consist of two main terms regularity term and the energy minimization term, which searches for uniformity of a desired feature. The initial contours of region-based active contour can be located anywhere in the image.

Let C be the evolving curve and c_1 and c_2 two constants, representing the averages of u_0 inside and outside the curve C. Assume that u_0 is an image formed by two regions of approximatively piecewise-constant intensities, with distinct values u_0^i and u_0^o. The object to be segmented is represented by the region with the value u_0^i whose boundary is denoted by C_0. Therefore $u_0 \approx c_1$ inside C and $u_0 \approx c_2$ outside C. Considering the following fitting energy, formed by two terms:

$$F_1(C) + F_2(C) = \int_{inside(C)} |u_0 - c_1|^2 dxdy + \int_{outside(C)} |u_0 - c_2|^2 dxdy \qquad (2.15)$$

If the curve C is outside the object, then $F_1(C) > 0$ and $F_2(C) \approx 0$. If the curve is inside the object, then $F_1(C) \approx 0$ but $F_2(C) > 0$. Finally, the fitting energy will be minimized if the $C = C_0$ if the curve is on the boundary of the object. This is illustrated in Figure 2.6.

The energy function with regularizing terms is introduced as follows:

$$\begin{aligned} F(C, c_1, c_2) &= \mu \cdot length(C) + \upsilon \cdot area(insudeC) \\ &+\lambda_1 \int_{inside(C)} |u_0 - c_1|^2 dxdy + \lambda_2 \int_{outside(C)} |u_0 - c_2|^2 dxdy \end{aligned} \qquad (2.16)$$

where c_1 and c_2 are constants, and $\mu > 0$, $\upsilon \geq 0$, $\lambda_1, \lambda_2 > 0$ are fixed parameters. The *length* and *area* terms are regularization terms.

The results obtained by this method partitioned the image which is represented as a set of piecewise-constants, where each subset is represented as a constant. This approach has shown the fastest convergence speed in comparison to region-based active contours due to the simple representation.

Level set methods can be categorized into techniques based on partial differential equations (PDE) [60] or variational level sets [61]. The level set evolution (LSE) of PDE-based methods is mostly based on the geometric considerations of the motion equations [62]. On the other hand, the LSE of variational level set methods is mostly based on optimizing an objective energy functional defined on the level set [61]. Variational level set methods are therefore amenable to incorporating additional information in the LSE, such as region-based information [55,61], shape-prior information [63] and phase-based information [64], which usually gives rise to very accurate boundary detection results.

Recently, several authors have proposed variational level set methods that in-

corporate different image features into the energy functional. These methods, which have also been tested on medical images, aim at solving common issues that hinder segmentation accuracy, such as leakage around weak edges and high sensitivity to intensity inhomogeneities [60–62, 64–70]. For example, Kimmel [67] propose an active contour model with an energy functional that combines an alignment term that leads the curve to the boundary of the desired region. Specifically, the alignment term attempts to align the normal vector of the zero level set with the image's gradient. Although this alignment term leads to more accurate segmentation results, the method may fail to accurately drive the zero level set to the desired boundary around weak edges due to the fact that the gradient of the image around weak edges is relatively small [69].

Belaid *et al.* [64] propose a phase-based level set (PBLS) method for segmentation of medical images with high levels of noise and weak edges. In their approach, the authors construct a speed term based on two phase features: local phase, which is derived from the monogenic signal; and local orientation, which measures the alignment between the local image orientations and the contour's normal direction of movement. Although PBLS has shown to perform very well in the presence of weak edges, it requires careful tuning of the parameters. [71].

Estellers *et al.* [69] propose a segmentation method based on the geometric representation of images as 2D manifolds embedded in a higher dimensional space. Their method, termed harmonic active contours (HAC), aligns the image's gradient with the gradient of the level set function for all the level sets. This results in an objective functional that is able to exploit the alignment of the neighboring level sets to pull the contour to the right position. Although HAC has been shown to provide excellent segmentation results on medical images, it may perform poorly on images with several intensity inhomogeneities [72].

Zhou *et al.* [73] propose to combine an edge-based active contour model and region-based active contour model for segmentation of the left ventricle in cardiac

CT images. Based on the image gradient, their method adjusts the effect of the two models. Although this method shows good performance around weak edges, the results are highly dependant on the placement of the initial contour. Ji *et al.* [74] propose a local region-based active contour model for medical image segmentation that uses the spatially varying mean and variance of local intensities to construct a local likelihood image fitting (LLIF) energy functional. Their method performs well in images with low contrast and intensity inhomogeneities. However, as with other region-based active contour models, it assumes the existence of two well-differentiated regions, which may not always be true in medical images.

2.2.7 Deep Learning Active Contour

Deep learning is a growing trend in data analysis and has been termed recently as one of the breakthrough technologies [75]. Deep learning is a development of artificial neural networks, consisting of more layers that improved predictions from data and allow higher levels of abstraction [76]. Convolutional neural networks (CNNs) shown to be important tools for a broad range of computer vision tasks. Deep CNNs automatically learn high-level and mid-level abstractions obtained from images. Recent studies indicate that the generic descriptors extracted from CNNs are extremely effective in object recognition and localization in medical image analysis especially when applying other deep learning methodologies.

Ghesu *et al.* [77] proposed a combination of deep learning and marginal space learning for segmentation and object detection. This combination increased computational efficiency and led to reduction the mean segmentation error. Brosch *et al.* [78] addressed the problem of multiple sclerosis brain lesion segmentation on MRI by developing a 3D deep convolutional encoder network that combined deconvolutional pathways and interconnected convolutional. The deconvolutional pathway predicted the voxel-level segmentation, and the convolutional pathway learned higher level features. Pereira *et al.* [79] proposed a method use a deeper architec-

ture, intensity normalization and data augmentation for brain tumour segmentation on MRI. They used a different CNN architectures for low and high-grade tumours. Kallenberg *et al.* [80] proposed unsupervised feature learning for breast density segmentation and automatic texture scoring. The model learns features across multiple scales. Once the features are learned, they are fed to a simple classifier that is specific to two different tasks i) breast density segmentation, and ii) scoring of mammographic texture.

Deep learning have also been successfully applied to active contour models. For instance, Hoogi *et al.* [81] proposed an adaptive method to estimate the parameters for the level set energy functional separately over iterations. This method is a multi-stage process: First, CNN is used to identify the location of the zero level set contour in relation to the lesion. Second, the minimization of the cost function is done by an iterative process that considers the scale of the lesion, local and global texture statistics to re-estimated window size. Rupprecht *et al.* [82] proposed a novel method which combines a deep, patch-based representation with an active contour framework for interactive boundary extraction. A trained a class-specific CNN is used to predicts a vector pointing from the respective point on the evolving contour towards the closest point on the boundary of the object of interest. These predictions form a vector field which is then used for evolving the contour. Nago *et al.* [83] proposed automated segmentation approach for the endocardial and epicardial borders of the left ventricle (LV) from all slices of the end diastole (ED) and end systole (ES) cardiac phases of an MR cine study, where the ED and ES volumes are manually selected by the user. This approach combines an active contour model with a machine learning approach (deep belief network). This combination producing a methodology that needs small training sets and produces accurate segmentation results. Kainz *et al.* [84] proposed a method to segment glands in Hematoxylin-Eosin (H&E) stained histopathological images of colorectal cancer using deep CNN and total variation segmentation. Two deep CNN are trained as pixel classifiers to predict

glands (Object-Net) and gland-separating structures (Separator-Net) from the image. The CNN predictions are then regularized using a figure-ground segmentation based on weighted total variation to produce the final segmentation result.

Chapter 3

Active Contour Based on Weighted Gradient Vector Flow and Balloon

3.1 Introduction

Although image segmentation algorithms have been developed over decades it remains a complex and challenging task. A given segmentation method may perform well on one problem but it may not work in a different domain. It is very hard to achieve a general segmentation method that is universally applicable for range of different domains.

Deformable models is one of the most used methods in medical image segmentation. Deformable model can be described as a technique for defining region boundaries by using curves or surfaces close to the edges that deform under the effect of forces. Deformable models, including active contours (2-D) and active surfaces (3-D) are closed contours or surfaces which are able to expand or contract over time, within an image, and confirms to specific image features [34].

Active contours, or snakes, is a deformable model have been widely used for image segmentation purposes. However, high noise sensitivity and poor performance over weak edges are the most acute issues that hinder the segmentation accuracy

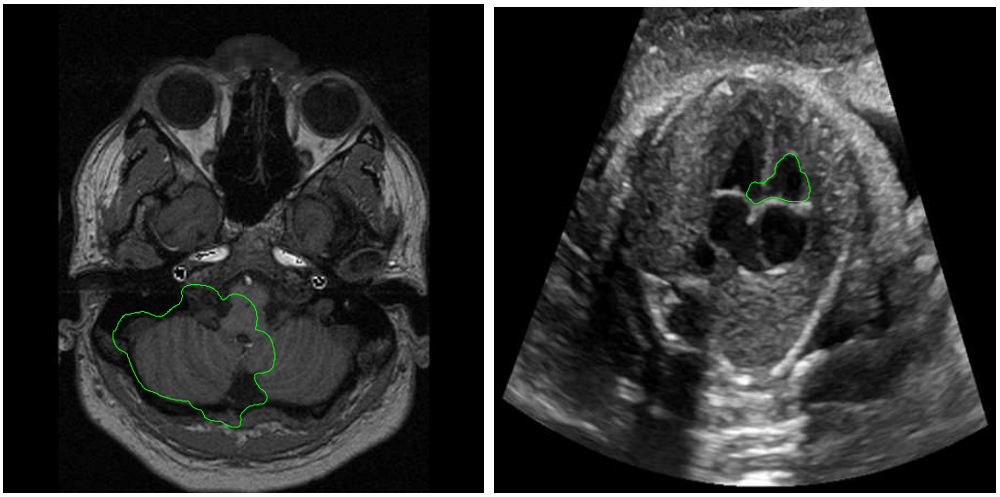

(a) (b)

Figure 3.1: Example of medical image segmentation with weak edges and using GVF active contour. (a) CT slice of skull. (b) 4 Chamber Heart Ultrasound.

of these curves, particularly in medical images as shown in Figure 3.1. In order to overcome these issues, this chapter propose a new external force that combines the advantages of balloon and GVF forces. Specifically, balloon force is employed to guide the snake to the object's boundary even in the presence of image clutter and noise; while a GVF force is employed to improve convergence to the object's boundary even around weak edges. The influence of these two types of forces on the snake's movement is controlled by using a weighting function based on local image features. The proposed external force minimizes snake leakages and considerably reduces the number of initial snake elements, making it suitable for segmentation of medical images with little manual intervention.

The rest of the chapter is organized as follows. Section 3.2 reviews the basic concepts of snakes. Our proposed external force is detailed in Section 3.3. Experimental results for segmentation of real medical images are presented in Section 3.4. Finally, a summary presented in Section 3.5.

3.2 Background

Parametric deformable models represent curves or surfaces in parametric form. The parametric models can be described with two main formulations; formulation of minimizing energy and formulation of dynamic force. The formulation of minimizing energy search for a parametric curve that minimizes a weighted sum of internal energy and external energy. Internal energy controls the smoothness of the curve, while external energy is defined in the image domain and it takes smaller values at smooth regions than object boundaries where the gradient at the edge is high. When internal and external energies are equal, the total energy minimization occurs.

A snake is a curve, first proposed by Kass *et al.* [7], this curve is sampled and represented by a set of discrete points, these sample points are referred to as snake elements [see Equation (2.1)] . After the curve has been defined, the curve has to be placed near to the boundary of area of interest. Now, a process has to be performed on the curve which makes the curve deform or evolve and this process is called curve evolution [42]. Curve evolution is an iterative computation that makes the curve slide in the selected area on the image. The initialized curve will be pushed by special forces to the object boundary. The curve will stop moving once it reaches the boundary. Based on (2.3) and (2.4) a curve evolves to an object's boundary by minimizing the following energy function:

$$E_S(C) = \frac{1}{2}\int_0^1 (\alpha\left|C'(s)\right|^2 + \beta\left|C''(s)\right|^2)ds + \int_0^1 E_{ext}(C(s))ds \tag{3.1}$$

The first integrand in Equation (3.1) is referred to as the internal energy, which controls the smoothness of C, while the second integrand is referred to as the external energy, which attracts C towards the object's boundary. The internal energy of the snake consist of C' and C'' which are the first and second derivative. The first derivative provides the amount of changes of coordinate locations or length of the curve, which means the longitudinal contraction of the curve. The parameter

α controls the contraction of the curve and makes the snake act like an elastic string. Large values of α means large contraction of the snake in the direction of the force [85]. Therefore, α represents the elasticity coefficient. The second derivative provides the amount of the curvature. The coefficient β regulates the rate of change of the curve in the normal direction of its borders. This term makes the snake act like a rigid string. This means that the curve maintains the smoothness but does not contract. A high value of β makes the curve hard and resists bending, while small values allow the curve to develop a corner.

The external energy is usually defined as the negative intensity of the image edge map f, i.e., $E_{ext}(x, y) = -f(x, y)$, which is usually given by (2.5). The minimization of E_S can be achieved by evolving the snake dynamically as a function of parameter s and artificial time t as follows:

$$C(s,t) = \Big[\alpha C''(s,t) - \beta C''''(s,t)\Big] - \nabla E_{ext} \tag{3.2}$$

where the first term and the second term are called the internal force, F_{internal}, and the external force, $F_{external}$, respectively.

3.2.1 External Forces

External forces can be divided into dynamic forces and static forces [36]. Dynamic forces, e.g., balloon forces, depend on the snake itself and change as the snake deforms. Static forces, e.g., GVF forces, are computed from the image and do not change as the snake deforms.

Balloon Force

Balloon forces are computed iteratively and may have an inflation or deflation effect on the snake depending on the snake's initial position with respect to the desired boundary. These forces are represented as:

$$F_{balloon} = k\boldsymbol{n}(s) \tag{3.3}$$

where $\boldsymbol{n}(s)$ is a unit vector normal to the snake at snake element C_n, and k is the force strength. The sign of k is responsible for inflation (+) or deflation (-). Although active contours based on balloon force deforms in areas with small or zero gradient magnitude, however, balloon force still has some limitation such as a leakage around weak edges. Another limitation of snakes using balloon force is that the snake initialization must be either inside or outside the desired object, which requires prior knowledge of object location [86].

Gradient Vector Flow

The model that was proposed by Cohen [37] has solved some problems of the original model, but segmenting the area that has a concavity remains a problem. Therefore, Xu *et al.* [36] propose a gradient vector flow (GVF) that expands the capture range and forces the snake into the concave regions.

GVF forces are derived from the diffusion of the gradient vectors of the image edge map. Let $\mathbf{v}(x, y) = [u(x, y), \nu(x, y)]$ denote the GVF field, which is set to minimize the following energy function:

$$E_{GVF}(\mathbf{v}) = \iint \mu|\nabla\mathbf{v}|^2 + |\nabla f|^2|\mathbf{v} - \nabla f|^2 dxdy \tag{3.4}$$

where ∇f is the edge map defined in (2.5). The first term in (3.4) is used to smooth the vector field $\mathbf{v}$, which has the main effect of increasing the capture range of the force field, where μ is a smoothness regularization parameter. The second term is the data fidelity term that makes $\mathbf{v}$ equal to the gradient vector of the edge map (∇f) where $(|\nabla f|)$ is relatively large, and thus preserves edge information. The parameter μ is a regularization parameter governing the trade-off between the first term and the second term [87]. This parameter is set according to the amount of noise in the image. It cannot restrain noise effectively, if there is a lot of noise in the image [88]. Energy minimization of (3.4) is achieved by satisfying the following Euler equations:

$$\begin{aligned} \mu\nabla^2 u - (u - f_x)({f_x}^2 + {f_y}^2) = 0 \\ \mu\nabla^2 \nu - (\nu - f_y)({f_x}^2 + {f_y}^2) = 0 \end{aligned} \tag{3.5}$$

where ∇^2 is the Laplacian operator. Note that the second term of equation 3.5 is zero in homogeneous regions because the gradient of $f(x, y)$is zero. Therefore, u and ν are each determined by Laplacian equation resulting in a sort of filling information in that area directed to the boundaries of the region.

Replacing the external force in the dynamic snake equation of (3.2) by $\mathbf{v}(x, y)$ yields:

$$C_t(s, t) = \alpha C_{ss}(s, t) - \beta C_{ssss}(s, t) + \mathrm{v}(x, y) \tag{3.6}$$

Note that although the capture range of GVF is in general large, methods using this external force exclusively may fail if the snake is initialized far from the desired boundary using a relatively small initial curve (see Figure 3.2). The GVF field around such small initial snakes may not point towards the desired boundary due to the high levels of noise and clutter. An initial snake closer to the boundary may increase segmentation accuracy in this case.

Vector Field Convolution

Vector field convolution (VFC) [86] is a static external force field computed by convolving the edge map with a prefixed vector kernel. VFC provides a large capture range as GVF and the ability to capture concavities, but the difference here is that the VFC has superior noise robustness and less computational cost. The prefixed vector kernel defined as $\boldsymbol{k}(x, y) = [u_k(x, y), \nu_k(x, y)]$ where all vectors point to the origin of the kernel as shown in Figure 3.3.

$$\boldsymbol{k}(x, y) = m(x, y) \times \mathbf{n}(x, y) \tag{3.7}$$

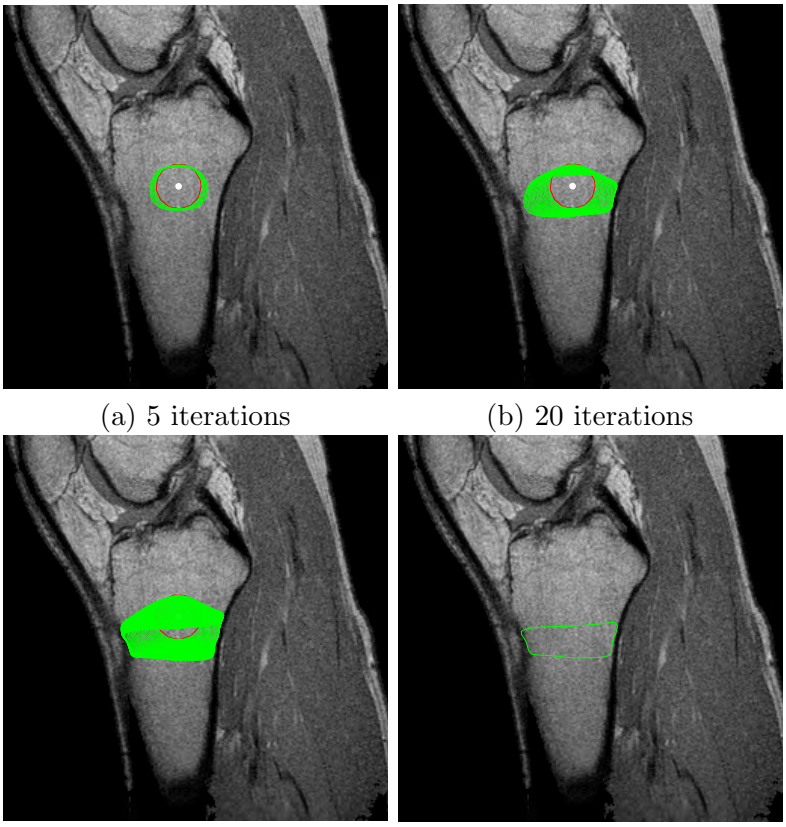

(a) 5 iterations (b) 20 iterations

(c) 60 iterations (d) Final result

Figure 3.2: A GVF snake that fails if initialized by a small curve far from the desired boundary. The green represents deformation process, white dot represents the manually selected initial position, the red curve represents the initial snake

where $m(x, y)$ is the magnitude of the vector at (x, y) , and $\mathbf{n}(x, y)$ is the unit vector pointing to the origin. The origin is located in the center of kernel matrix.

The VFC external force field $\boldsymbol{V}_{vfc}(x, y) = [u_{vfc}(x, y), \nu_{vfc}(x, y)]$ is given by calculating the convolution of the vector field kernel $k(x, y)$ and the edge map $f(x, y)$.

$$\boldsymbol{V}_{vfc}(x, y) = f(x, y) \times \boldsymbol{k}(x, y) \tag{3.8}$$

Since the edge map $f(x, y)$ has large values near to the edges, those edges contribute more to the VFC force field than do the homogeneous regions.

The VFC depends on the choice of the vector field kernel magnitude $m(x, y)$.

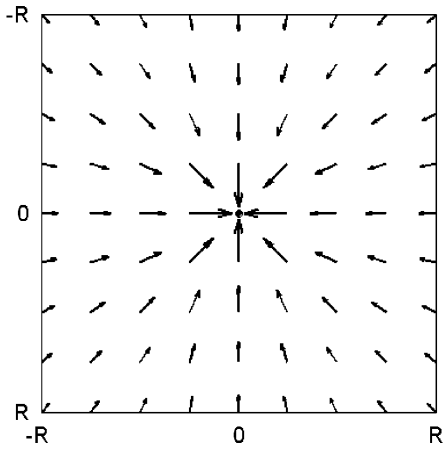

Figure 3.3: Example discrete vector field kernel [86]

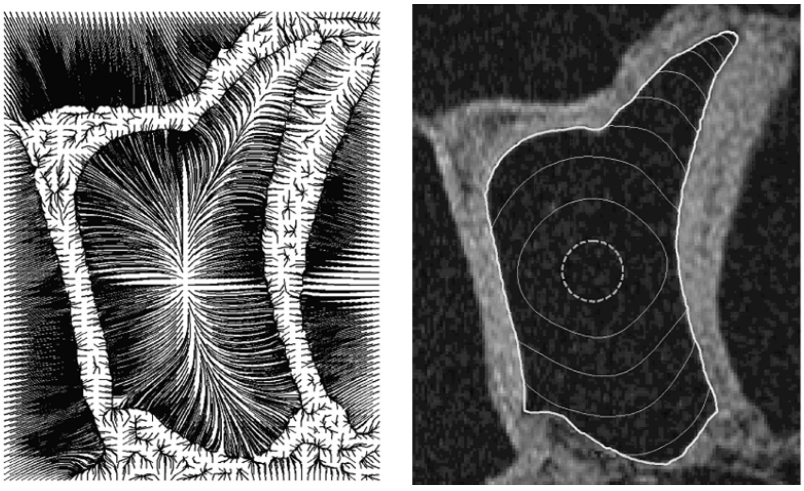

(a) (b)

Figure 3.4: (a) The streamlines of VFC field, (b) snake deformation using VFC [86].

As areas far away from the edges should have less influence, thus the magnitude should be a decreasing function of distance from the origin [42]:

$$m(x, y) = (r + \varepsilon)^{-\gamma} \tag{3.9}$$

where γ is a non-negative parameter and is used to control the rate of decrease in the magnitude, and $r = \sqrt{x^2 + y^2}$ is the distance from the origin. Parameter ε, is a positive constant used to prevent division by zero at the origin. Given an initial contour as shown in Figure 3.4, the VFC external force field will guide the contour to the object boundary.

3.2.2 Active Contour Initialization

In most of active contours, the curve deformation is stopped by edges or noise. So if the initialization method can avoid noise, then the curve can deform easily without getting interrupted by noise. The options for active contour initialization can be categorized into manually initialized or automatically initialized. In manual initialization, usually, the user has to manually specify the initial contour, and this location has to be carefully chosen to achieve appropriate segmentation. This interaction is prone to error, takes a long time and is not feasible in applications with thousands of target objects [14]. This section will focus on two automatic initialization methods, Centers of Divergence (CoD) and Poisson inverse gradient (PIG).

Centers of Divergence (CoD)

The center of divergence (CoD) [89] method is used to initialize the contour in the best location automatically without user intervention. This approach places a contour as a small circle at the point of zero vector divergence within a given external force, such as GVF or VFC. However, CoD suffers from over-segmentation (initial number of contour). Over-segmentation requires a post-process to merge the

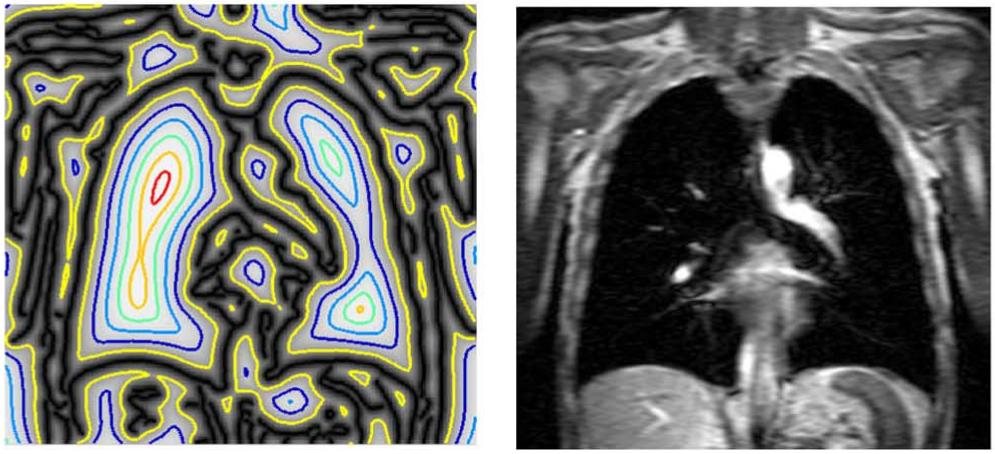

(a) (b)

Figure 3.5: (a) MR image slice of a human lung, (b) contours or isolines generated from the edge map by PIG [90]

regions and remove the pseudo boundaries.

Poisson Inverse Gradient (PIG)

The Poisson inverse gradient (PIG) [90] is another method of automatic initialization. This method estimates the energy field from a given external force field that is computed from the image. This energy provides isolines represented as closed contours as shown in Figure 3.5. The isoline with minimum energy level is the best position for active contour initialization, usually it is the one that is closest to the edges [91]. However, PIG may fail if the image suffers from weak edges.

3.3 The Proposed Method

The proposed external force is a weighted combination of balloon and GVF forces and aims at exploiting the advantages of each of these two types of forces. As described in section 3.2.1, the computation of the GVF force requires the computation of the gradient vector of the edge map, ∇f.

3.3.1 Edge Map

One of the important requirements for segmentation is that the edge must be accurately detected and the noise removed as much as possible from the scene. Edge map is very important for computing image forces like GVF and VFC.

In this work, the edge map $f(x, y)$ is computed by first calculating the eigenvalues and eigenvectors of the 2×2 Hessian matrix $HM_{x,y,L}$, for each pixel at position (x, y). The elements of $HM_{x,y,L}$ are the coefficients of the three detail sub-bands of the stationary wavelet transform (SWT) [92] decomposition of the image at level L, as follows:

$$HM_{x,y,L} = \begin{bmatrix} |V_{x,y,L}| & |D_{x,y,L}| \\ |D_{x,y,L}| & |H_{x,y,L}| \end{bmatrix} \tag{3.10}$$

where $V_{x,y,L}$, $H_{x,y,L}$ and $D_{x,y,L}$ are the coefficients of the vertical, horizontal and diagonal detail sub-bands, respectively, at pixel position (x, y) and decomposition level L. The largest absolute eigenvalue of $HM_{x,y,L}$, whose eigenvector represents the direction of highest curvature, is used as the intensity value of the edge information at position (x, y), so that $f(x, y) = \max(|e1_{x,y}|, |e2_{x,y}|)$, where $e1_{x,y}$ and $e2_{x,y}$ denote the two eigenvalues associated with $HM_{x,y,L}$. The edge map $f(x, y)$ is normalized to the range $[0, 1]$. Figure 3.6 shown an example of edge map obtained by SWT.

3.3.2 Proposed external Force

The proposed external force is then defined as follows:

$$F_{external} = (F_{Balloon} * (1 - \Omega)) + (F_{GVF} * \Omega) \tag{3.11}$$

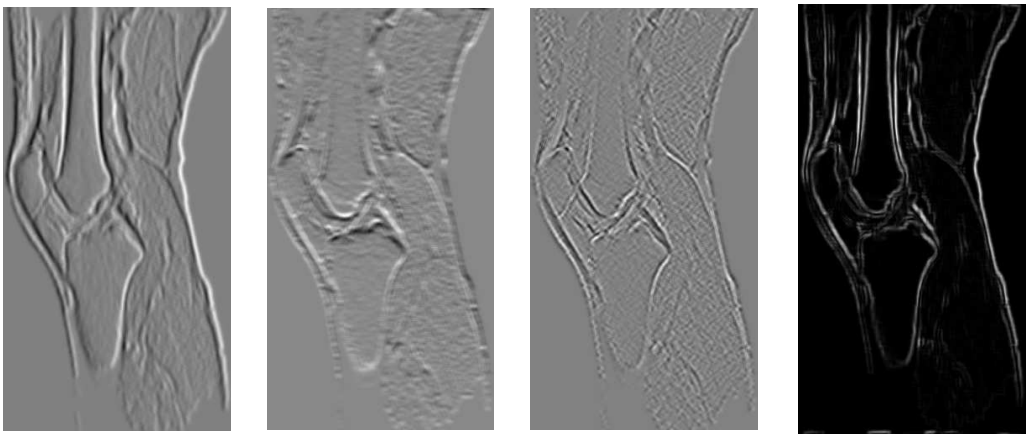

(a) (b) (c) (d)

Figure 3.6: (a),(b) and (c) are the horizontal, vertical and diagonal coefficients, respectively. (d) the edge map.

where F_{GVF} and $F_{Balloon}$ denote the GVF force and balloon force, respectively, and $\Omega \in [0, 1]$, is a weighting factor given by:

$$\Omega = \bar{h}^{(1-(\bar{AD}-\varepsilon))} \tag{3.12}$$

where $\bar{h} \in [0, 1]$ denotes the average value of $f(x, y)$ over a semi-circular region S centered at each snake element, and $\bar{AD} \in [0, 1]$ is the angular difference between the direction of the balloon force and the average direction of the GVF force field over a cone-shaped region T centered at each snake element. $\bar{AD} = 0$ represents 0 radians, while $\bar{AD} = 1$ represents π radians. The constant $\varepsilon = 0.001$ is used to prevent power by zero when $\bar{AD} = 1$. For each snake element at position (x, y), $\bar{h}$ is calculated as follows:

$$\bar{h}(x, y) = \frac{1}{N} \sum_{(i,j)\in S} h(i, j) \tag{3.13}$$

where N is the number of edge map pixels located in region S and h is the edge intensity at position (i, j), as illustrated in Figure 3.7.

For each snake element at position (x, y), $\bar{AD}$ is calculated as follows:

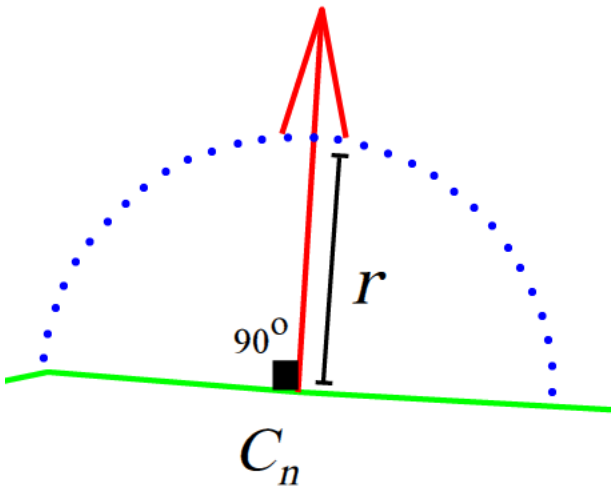

Figure 3.7: Region S for snake element C_n. The snake is represented in green. The red arrow represents the direction of the balloon force which is normal to the snake at element C_n. The blue dotted line represents region S of radius r.

$$\bar{AD}(x,y) = \frac{1}{M * \pi} \sum_{(i,j)\in T} \theta(i,j) \tag{3.14}$$

where M is the number of GVF field vectors in region T, θ is the angle between the GVF field vector at point (i,j) and the balloon force vector for snake element C_n at position (x,y). Region $T(x,y,sl,\varphi)$ is defined by a cone shape with its vertex in (x,y), where sl is the slant height of the cone and φ indicates the half of the cone angle. This is illustrated in Figure 3.8. Note that a cone-shaped region was chosen as opposed to a semi-circular region, such as region S, for two reasons. First, it allows analyzing the region located far from the snake element, which provides a better insight of the direction of the GVF field than the region close to the snake element. Second, it reduces the number of calculations since there are fewer points in total than a semi-circular region of equivalent size.

Note that the weighting function in Eq. (3.12) assigns different priorities to balloon and GVF forces according to local image features. These features are the average amount of edge information ($\bar{h}$) and average direction of the GVF field ($\bar{AD}$). It is important to mention that the simplest possible method to control the

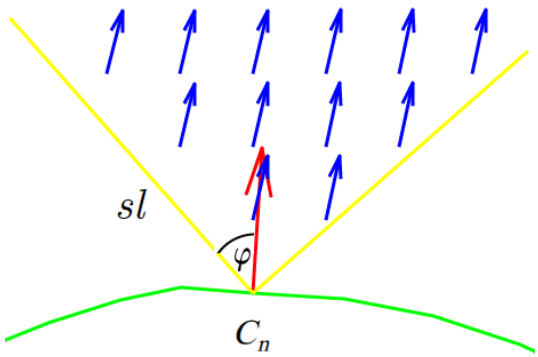

Figure 3.8: Region T for snake element C_n. The snake is represented in green. The red arrow represents the direction of the balloon force, which is normal to the snake at element C_n. Blue arrows represent the GVF field vectors within region T.

influence of balloon and GVF forces on the snake's movement is to use a thresholding approach based on $\bar{h}$ and $\bar{AD}$ values. However, the use of continuous functions, such as the one in Equation (3.12), where no hard decision is required, usually leads to better results [93]. Figure 3.9 shows the plot of Equation (3.12) for various values of $\bar{AD}$. It can be seen that Ω approaches 0 for small $\bar{h}$ values regardless of the $\bar{AD}$ value, i.e., when the snake is located in a smooth region. In this case, balloon forces are the main acting external forces driving the snake close to the object's boundary. It can also be seen that Ω approaches 1 in a linear fashion as $\bar{h}$ and $\bar{AD}$ increase, i.e., when the snake is located in a non-smooth region and its normal direction of growth does not coincide with the local average direction of the GVF field. In this case, GVF forces tend to be the main acting external forces, helping the snake conform to the object's boundary.

Therefore, Ω allows the snake to deform in smooth areas even if its normal direction of growth is opposite to the GVF force. This is particularly useful to initialize the snake with a very limited number of snake elements located far from the desired boundary. Figure 3.10(a) and 3.10(b) illustrate this case, where Ω approaches 0. Weight Ω also minimizes snake leakages around weak edges by averaging the amount of edge information and the direction of the GVF field over regions S and T, respectively. This is illustrated in Figure 3.10(c), where the value of Ω slowly

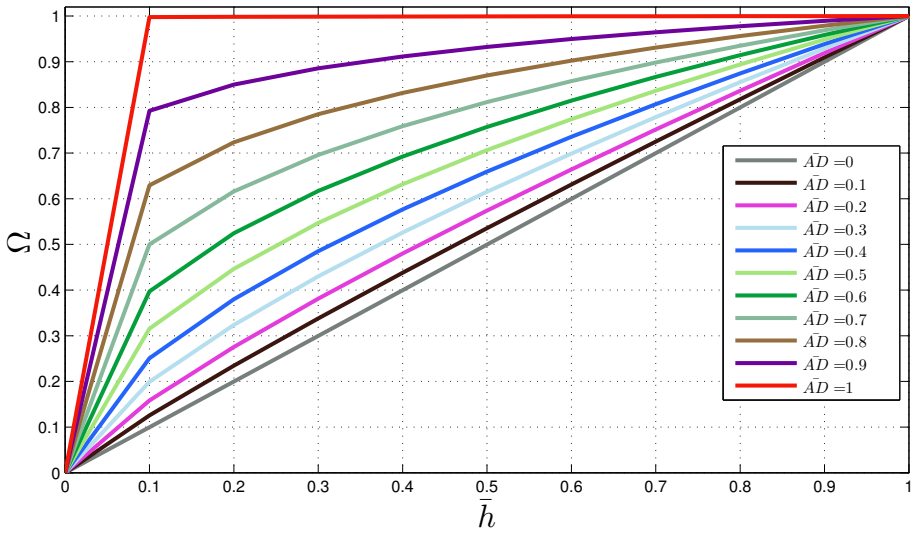

Figure 3.9: Value of Ω for different values of $\bar{h}$ and $\bar{AD}$.

approaches 1. Finally, Ω allows the snake to conform to the desired boundary by assigning a higher weight to the GVF force when edges are encountered. This is illustrated in Figure 3.10(d), where the value of Ω approaches 1.

3.3.3 Deformation Stopping Criteria

In classical snakes, the deformation process is usually performed over a fixed number of iterations, over which it is expected to achieve convergence, i.e., external forces are close to zero. For images with strong edges, this number of iterations may be easily determined empirically. However, for images with weak edges, this number should be carefully selected to prevent leakages [94]. This section proposes a mechanism to terminate the deformation process based on the percentage of snake elements labeled as *off*. A snake element is said to be *off* if no external force is acting on it. This usually occurs when the element encounters a strong edge, i.e., F_{GVF} is the main acting external force ($\Omega > 0.5$) and the overall strength of the GVF field around the element is close to zero. To this end, if $\Omega > 0.5$, Ω_b is computed in the same manner as Ω in Equation (3.12), but using regions S_b and T_b, as illustrated in Figure. 3.11. Then label a snake element as *off* and set its forces to zero if $(\Omega_b)^2 > \Omega > 0.5$.

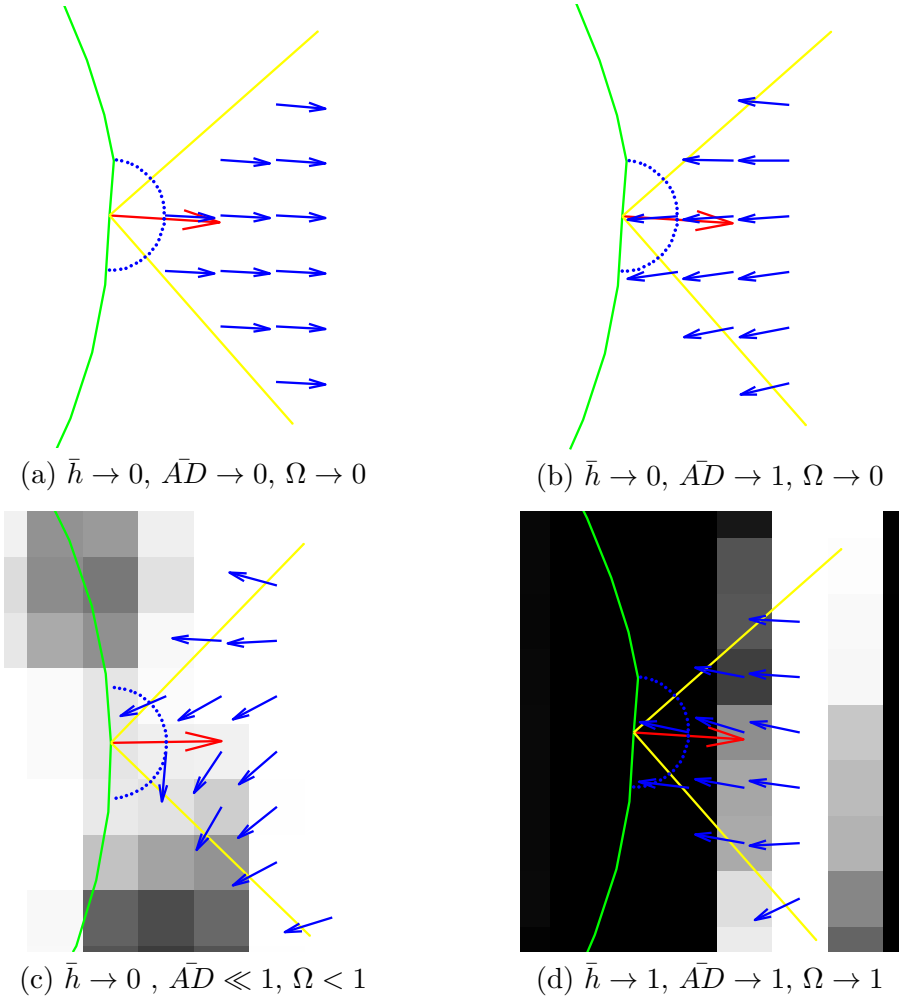

(a) $\bar{h} \to 0$, $\bar{AD} \to 0$, $\Omega \to 0$ (b) $\bar{h} \to 0$, $\bar{AD} \to 1$, $\Omega \to 0$

(c) $\bar{h} \to 0$, $\bar{AD} \ll 1$, $\Omega < 1$ (d) $\bar{h} \to 1$, $\bar{AD} \to 1$, $\Omega \to 1$

Figure 3.10: Direction of the GVF field within region T for different cases where the average amount of edge information ($\bar{h}$) varies within region S (the snake is represented in green and non-white pixels represent strong edge information). (a) The direction of the GVF field is similar to the normal direction of growth of the snake (red). (b) The direction of the GVF field is opposite to the normal direction of growth of the snake. (c) The direction of the GVF force field around weak edges. (d) The direction of the GVF force field around strong edges.

This condition allows determining if the overall strength of the GVF field around the element is close to zero, i.e., the GVF field has opposite directions in regions T and T_b. The squared value of Ω_b is used to prevent the element from *moving* past the edge. If the percentage of *off* snake elements is equal or greater than Q, the whole deformation process is terminated.

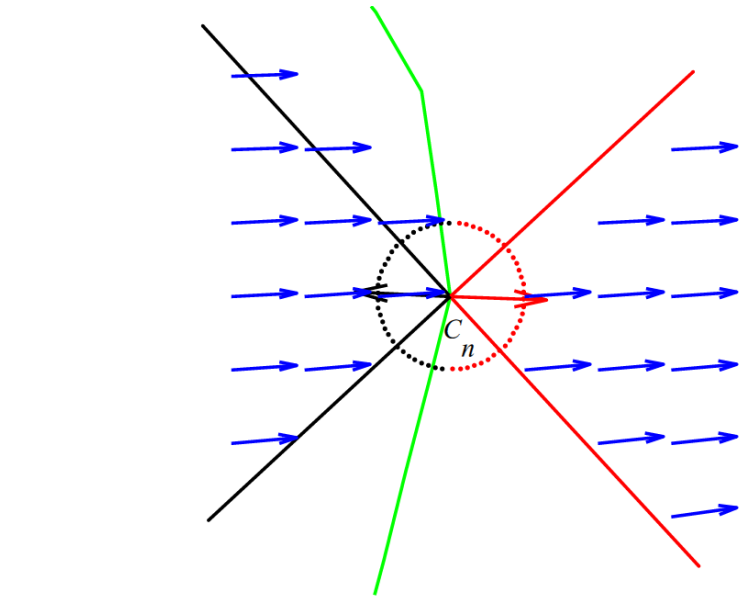

(a)

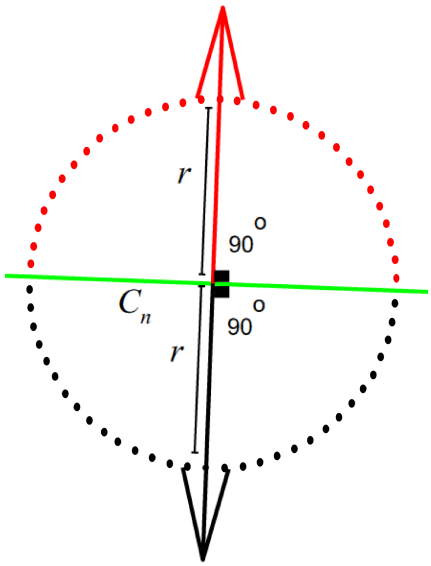

(b)

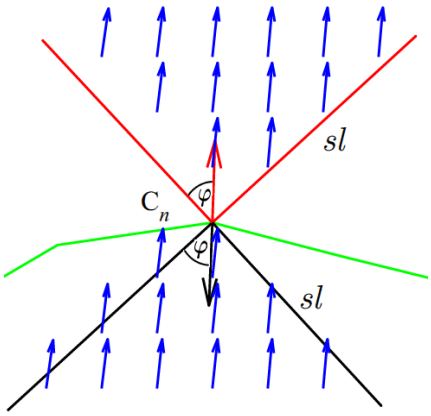

(c)

Figure 3.11: (a) Regions T and S (in red) used to compute Ω, and regions T_b and S_b (in black) used to compute Ω_b. (b) Dimension of regions S and S_b and of (c) regions T and T_b.

3.4 Experimental Results

This section presents several experiments on real slices of MRI and CT sequences to evaluate the performance of the proposed external force compared to snakes using three different external forces: a) GVF force exclusively [36], b) balloon and image gradient (BGrad) forces [43], and c) balloon or GVF forces based on thresholding (BGVFT). In method (c), the external force is either balloon or GVF based on the value of $\bar{h}$, which is computed as described in section 3.3.2.

In our experiments, images are preprocessed using histogram equalization to enhance edges. The edge map is computed as described in section 3.3.2 using the Haar filter with $L = 3$, which is the third level of decomposition. The value of $\alpha = 0$ and $\beta = 10$ is used to control the smoothness of the snake, and a value of $\mu = 0.2$ for the regularization parameter to compute the GVF field, as suggested in [36]. For our proposed external force, a radius $r = 1$ pixel is used for region S, an angle $\varphi = 45^o$ and $sl = 5$ pixels for region T. These values provide the best trade-off between capturing enough information about local image features and computational complexity. In all experiments, the snake is placed inside the desired region by manually selecting a single position. This single position is used as the center of an initial circular snake with a radius of 10 pixels.

Note that when computing the edge map $f(x, y)$ as described in section 3.3.2, the position of edges shifts by a number of pixels from their actual position in the original image. This shifting effect is a consequence of the redundant properties of the SWT and depends on the size of the filter [95, 96]. The amount of shifting Λ_L, in pixels locations, for L levels of decomposition using the Haar filter is given as follows:

$$\Lambda_L = \sum_{\ell=1}^{L} \Delta_{\ell-1:\ell} \tag{3.15}$$

$$\Delta_{L-1:L} = 2^{(L-3)} \times (d_0^{Lo} + 3d_0^{Hi} - 4) \tag{3.16}$$

where d_0^{Lo} and d_0^{Hi} denote the size of the low pass and high pass filters, respectively. For the Haar filter, $d_0^{Lo} = d_0^{Hi} = 2$. Therefore, the position of the final snake is shifted back according to Equation (3.15) in order to correctly position the snake on the desired boundary in the original image.

The detection accuracy of the evaluated external forces is measured by the Dice similarity coefficient (DSC) [97] and Jaccard coefficient (JC) [98] using manually annotated ground truth. The values of DSC and JC are within the range $[0, 1]$, where 1 indicates identical overlap and 0 indicates no overlap between regions inside the boundaries.

The DSC represents the ratio between the intersectional area of A and B and their summation area, i.e.,

$$DSC = \frac{2\,|A \cap B|}{|A| + |B|} \tag{3.17}$$

where A and B represent the segmented region and the ground truth, respectively, and $|\cdot|$ denotes the cardinal of a set. The value of DSC is within the range $[0, 1]$, where 1 indicates perfect overlap and 0 indicates no overlap, between A and B.

The JC measures similarity between finite sample sets, and is defined as the size of the intersection divided by the size of the union of the sample sets given by:

$$JC = \frac{|A \cap B|}{|A \cup B|} \tag{3.18}$$

The value of JC is within the range $[0, 1]$, where 1 indicates perfect overlap and 0 indicates no overlap between the sample sets.

Table 3.1 and Table 3.2 tabulate the DSC and JC values for different regions of MRI and CT slices. Images 1-3 represent three different regions on an MRI slice of a spinal cord, images 4 and 5 represent two regions on an MRI slice of a pelvis, images 6 and 7 represent two regions on an MRI slice of a knee, experiment 8 represents one region on a CT slice of a skull, and images 9 and 10 represent two regions on a CT slice of a spinal cord.

3.4.1 Experimental Results with Fixed Number of Iterations

In this experiment the number of iterations is equal for all evaluated external forces and is set to the number of iterations required by our proposed external force to achieve convergence. Results in Table 3.1 show that our approach achieves the highest accuracy for the most of the images. It is important to note that in some cases, the BGVFT snake achieves higher DSC and JC values than our approach for the same number of iterations (see images 6,7,10). In these cases, the selected threshold for the BGVFT snake effectively switches between GVF and balloon forces. However, note that the BGVFT does not converge in the tabulated number of iterations. In some cases, more iterations cause snake leakage in the BGVFT snake, unlike our approach which achieves convergence in less iterations and detects the boundary with high accuracy by automatically weighting the GVF and balloon forces according to local image features.

Visual results are shown in Figure 3.12. The GVF snake, which is represented in yellow, conforms to the desired boundary in most of the depicted cases. However, for the region in Figure 3.12 (a), this snake completely fails mainly due to the fact that the snake is initialized far from the boundary using a relatively small initial curve. Although the capture range of the GVF force is in general large, the direction of the GVF field around such small initial snakes may not point towards the desired boundary due to the high level of image noise and clutter. An initial snake closer to the desired boundary is necessary in this case to increase detection accuracy. The BGrad snake, which is represented in red, fails around weak edges causing snake leakages. This is mainly due to the fact that the balloon force is greater than the gradient force. As previously stated in [37], the strength of the balloon force should be manually selected to correctly detect weak edges. Note that our approach, which is represented in green, successfully conforms to the desired boundary with high accuracy for all depicted cases.

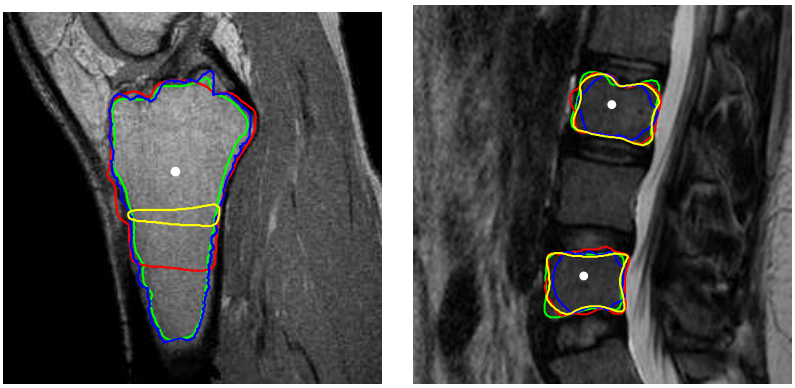

(a)

(b)

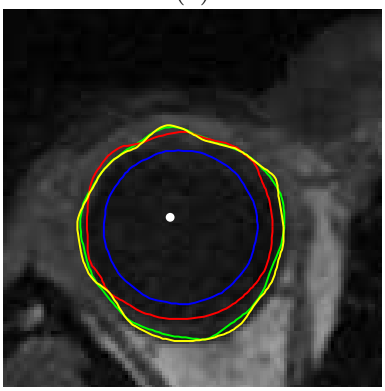

(c)

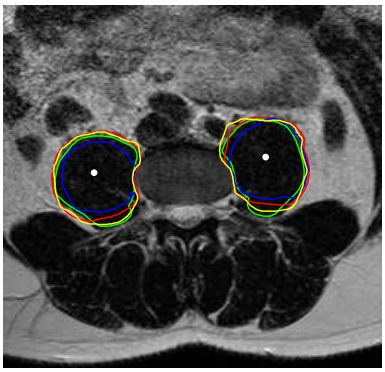

(d)

Figure 3.12: Final detected boundaries by the GVF snake (yellow), BGrad snake (red), BGVFT snake (blue) and our approach (green). The white dot inside each region represents the manually selected initial position for all evaluated snakes. (a) Image 6 - MRI slice of a knee. (b) Image 1 (upper region) and image 3 (lower region) - an MRI slice of a spinal cord. (c) Image 8 - a CT slice of a skull (left eye). (d) Image 4 (left region) and image 5 (right region)- an MRI slice of a pelvis.

Table 3.1: Detection accuracy of snakes using various external forces.

Image	GVF		BGrad		BGVFT		The Proposed approach		No. iterations
	DSC	JC	DSC	JC	DSC	JC	DSC	JC	
1	0.9342	0.8771	0.9024	0.8222	0.8944	0.8091	**0.9454**	**0.8890**	13
2	0.9474	0.9012	0.9193	0.856	0.9161	0.8452	**0.9513**	**0.9131**	13
3	0.9312	0.8727	0.8863	0.7962	0.9228	0.8551	**0.9483**	**0.9027**	14
4	0.9365	0.8801	0.9032	0.8244	0.9173	0.8477	**0.9586**	**0.9192**	15
5	0.9292	0.8685	0.9035	0.8241	0.9252	0.8614	**0.9541**	**0.9136**	16
6	0.0998	0.0523	0.8528	0.7433	**0.9423**	**0.8901**	0.9328	0.8724	44
7	0.0267	0.0126	0.6305	0.4603	**0.9557**	**0.915**	0.9262	0.8626	101
8	0.9545	0.9132	0.8846	0.7928	0.9051	0.8262	**0.9505**	**0.9041**	13
9	0.9245	0.8591	0.9191	0.8514	0.8962	0.8122	**0.9394**	**0.886**	8
10	0.8561	0.7487	0.8522	0.7424	**0.8943**	**0.8087**	0.8571	0.7508	27
Average	0.7536	0.6981	0.8651	0.7704	0.9166	0.8468	**0.9361**	**0.8810**	

3.4.2 Experimental Results with Proposed Stopping Criteria

Table 3.2 show the results where the number of iterations is equal for all evaluated methods and is set to the number of iterations required by our termination mechanism. The whole deformation process is terminated if more than Q =90% of the snake elements are labeled as *off*. The tabulated results show that our approach achieves the highest accuracy for the most of the images. Note that for images 8-9, the BGVFT snake achieves higher DCS and JC values than our approach for the same number of iterations. In these cases, the BGVFT snake effectively switches between GVF and balloon forces based on the selected threshold. However, the BGVFT snake, similarly to the GVF and BGrad snakes, requires manual selection of the number of iterations. More iterations may cause snake leakage, unlike our approach which terminates the deformation process when the majority of snake elements encounter strong edges.

Visual results for image 2 in Table 3.2 are shown in Figure 3.13. The BGrad snake conforms to the desired boundary with high accuracy (DSC=0.8969; JC=8130). However, for the same number of iterations required by our proposed approach, this snake does not reach the actual edge. More iterations may cause snake leakage around weak edges if the balloon force is greater than the gradient force. The GVF and BGVFT snakes result in leakages around weak edges. Our approach successfully conforms to the desired boundary with high accuracy.

Table 3.2: Detection accuracy of snakes using various external forces.

Image	GVF		BGrad		BGVFT		The Proposed approach		No. iterations
	DSC	JC	DSC	JC	DSC	JC	DSC	JC	
1	0.8716	0.7724	0.8795	0.7848	0.9341	0.8763	**0.9413**	**0.8902**	43
2	0.9329	0.8742	0.8969	0.8130	0.9368	0.8812	**0.9517**	**0.9079**	45
3	0.9041	0.8249	0.8840	0.7921	0.9374	0.8822	**0.9537**	**0.9115**	44
4	0.9311	0.8710	0.8676	0.7662	0.9365	0.8806	**0.9559**	**0.9154**	38
5	0.9345	0.8770	0.8493	0.7380	0.9612	0.952	**0.9631**	**0.9288**	43
6	0.1445	0.0779	0.8017	0.6691	0.9517	0.9078	**0.9643**	**0.9311**	96
7	0.0044	0.0022	0.6877	0.5240	0.8996	0.8174	**0.9709**	**0.9453**	171
8	0.9381	0.8834	0.9045	0.8256	**0.9568**	**0.9171**	0.9433	0.8926	45
9	0.9043	0.8253	0.8263	0.7040	**0.9393**	**0.8855**	0.9310	0.8709	26
10	0.9258	0.8619	0.6844	0.5202	0.9231	0.8541	**0.9426**	**0.8915**	60
Average	0.74913	0.68702	0.82819	0.7137	0.93765	0.88542	**0.95178**	**0.90852**	

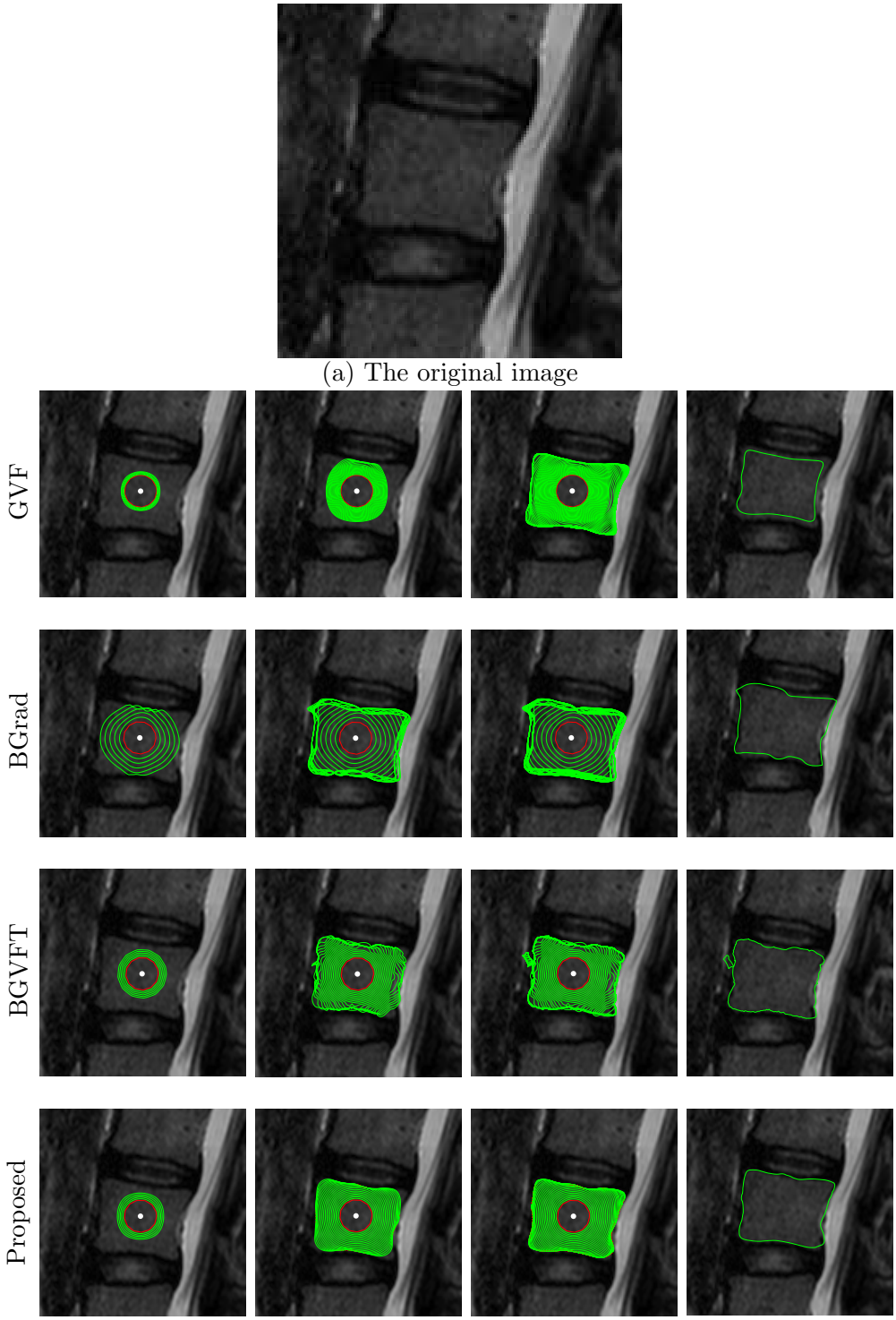

(a) The original image

(b) 5 iterations (c) 20 iterations (d) 60 iterations (e) Final result

Figure 3.13: Snake deformation process (green curves) for image 2. The white dot represents the manually selected initial position, the red curve represents the initial snake.

3.5 Summary

This chapter proposed a novel external force for parametric snakes that combines balloon and GVF forces. The external force uses a weighting factor to leverage the advantages of these two forces according to local image features. In smooth areas with little edge information, balloon forces guide the snake to the object's boundary, while in the presence of strong edge information GVF forces make the snake conform to the boundary. Our proposed approach is compared to snakes using GVF forces, balloon forces and a combination of GVF and balloon forces based on manual thresholding. Experimental results on real medical images show that the proposed approach outperforms methods based on traditional external forces, while offering the advantage of initializing the snake with a single manually selected point inside the desired region and terminating the deformation process automatically. However, this method has some limitations, such as, sensitivity to very high level of noise, to large broken edges or even no presence of edges.

Chapter 4

Weighted Level Set Evolution Based on Local Edge Features

4.1 Introduction

This chapter proposes a variational level set method that weights the level set evolution according to local image features in order to accurately drive the motion of the zero level set towards the desired boundary. This method is motivated by the proposed method in the previous chapter which deforms the contour using a weighting function based on local image features. More precisely, the proposed method in this chapter controls the influence of energy terms in the objective functional with a weighting function that takes into account two local image features: edge intensities and edge orientations. We employ the gradient vector flow (GVF) field of the image [35] as a measurement of local edge orientations.

Although other previously proposed methods also employ local features to control the contour's evolution [73, 99–101], the novelties about how local edge information is used in the proposed method are as follows:

1. The proposed method measures the average alignment between the normal direction of the evolving contour and the image's gradient in the adjacent region located inside and outside of the evolving contour. Other methods that also measure this alignment usually do this only in the region adjacent to the

evolving contour in the direction of movement. Moreover, this measurement is often used as an additional energy term in the energy functional. An example of such a method is the one proposed by Kimmel [67].

2. The proposed method also considers the average edge intensity in the adjacent region located inside and outside of the evolving contour. This allows to minimize the negative effect of weak edges on the segmentation accuracy.

3. The proposed method uses the collected local information to compute a single value that serves as a weight to control the influence of two main forces. This minimizes leakage in areas where weak edges exist. If the desired object is delimited by both weak and strong edges, this weight helps minimize the influence on weak edges if sufficient strong edges exist. As a consequence, the evolving contour tends to converge to the desired boundary even in areas where weak edges exit.

As mentioned in point (a), the method proposed by Kimmel [67] shares many similarities with the proposed method. This method also involves the alignment between the contour's normal and the image's gradient in the deformation process. This alignment is used to compute an additional force. One main disadvantage of using this extra force is that it can be sensitive to weak edges and non-smooth regions, in which the image's gradient may not follow a common direction. Another important difference of Kimmel's method with respect to ours is that it is based on a region-based model, where two regions are assumed to exist in the image.

Another method that also uses local information is the one proposed by Lankton *et al.* [99]. This method, which is region-based, models the foreground and background as constant intensities represented by their means. Local intensity information in this method is collected from various points along the evolving contour. Differently from our method, this method only employs intensity information as the local information. Another important difference is that it requires the user

to manually define a background region in order to help the contour to correctly segment the region of interest.

Jung *et al.* [100] propose a region-based active contour that employs local intensity information. This local information is collected from patches. Specifically, Jung's method uses a non-local energy that enforces non-local similarity of patches inside each region to be segmented. This patch comparison principle helps the active contour to optimize the homogeneity of each region. Employing patches, however, may lead to local energy measurements. Small patches give local intensity approximation but prevent the contour from moving when it entirely lies on a homogeneous area where local statistics on either side of the contour are the same. Choosing large patches, on the other hand, may lead to global intensity approximation, which usually produces results similar to the global intensity fitting energy [102].

Zhou *et al.* [73] propose a method that uses local information collected by a characteristic function that marks local regions in terms of a radius parameter. Differently from our method, which computes a single value, or weight, that represents the collected local information, Zhou's method does not take into account the overall effect of these locally collected information to drive the overall deformation of the contour. Differently from Zhou's method, our method averaging the inside and out side of the contour.

Xie's [101] method, which is edge-based, takes into account the magnetic interaction between the image's gradient and the contour. This is done by computing the dot product between the magnetic flux of the image and and bi-normal unit vector. The magnetic flux of the image is generated by using the gradient vectors at each pixel position, while the bi-normal unit vector is computed from the cross product of the level set normal and its tangent vector. The proposed method is similar to Xie's method in the sense that also takes into account the alignment between the contour's normal vector and the image's gradient. However, our method also considers the edge intensity information. Moreover, our method collects this

local information from the adjacent region located inside and outside of the evolving contour. This collected information, differently from Xie's method, is averaged into a single value that is used to weigh the importance of two main forces.

The performance of the proposed method has been tested on a great variety of challenging medical images from MRI and CT sequences featuring weak edges and intensity inhomogeneities. We also compare our method's performance to that of state-of-the-art level-set methods, specifically, reinitialization-free level set evolution via reaction diffusion (RD) [70], active contours based on gradient vector interaction and constrained level set diffusion (LSD) [101], distance regularized level set evolution (DRLSE) [103] and Kimmel's method [67]. Results show that our proposed method attains a high boundary detection accuracy, particularly in areas prone to leakage.

The rest of the chapter is organized as follows. Section 3.2 briefly reviews background information related to segmentation based on level set methods. Section 3.3 details our proposed method. Experimental results for segmentation of real medical images are presented Section 3.4. Finally we draw a summary in Section 3.5.

4.2 Background

The contour of zero level, defined in (2.6) is the border between a positive area and a negative area of $\phi(x, y)$. The level set function (LSF) ϕ of the contour C is given by the signed distance from the initial contour as:

$$\phi(x, y) = \pm d((x, y), C) \tag{4.1}$$

where $d((x, y), C)$ is the distance from point (x, y) to the contour C, and the sign indicates if the point (x, y) is inside $(+)$ or outside $(-)$ of C.

Let us consider a moving front represented implicitly by the zero level set of

an LSF $\phi(\mathbf{x}, t)$, such that $C(t) = \mathbf{x} \in R^2$, and it represented at any time t by

$$C(t) = \{\mathbf{x} \,|\phi\,(C(t), t) = 0\} \tag{4.2}$$

After taking the derivative of this moving front w.r.t t on both sides, the curve's evolution equation is expressed as $\phi_t + \nabla\phi \cdot C_t = \phi_t + \nabla\phi \cdot F\vec{N} = 0$ for $t > 0$, where $\nabla(\cdot)$ is a gradient operator. Since the normal of an LSF can be represented as $\vec{N} = \nabla\phi / |\nabla\phi|$, this curve evolution equation can be simplified to:

$$\phi_t = F\,|\nabla\phi| \tag{4.3}$$

where F represents a constant speed term that pushes or pulls the contour and is often computed based on the curvature.

Equation (4.3) represents the LSE equation of PDE-based level set methods. The LSE equation of variational level set methods is given by:

$$\phi_t = -E_\phi(\phi) = F\delta(\phi) \tag{4.4}$$

where $E_\phi(\phi)$ denotes the first variation of an energy functional, $\delta(\phi)$ is the Dirac delta function, and F is defined as before.

It is important to mention that during evolution, the LSF usually becomes too flat or too steep near the zero level set, resulting in numerical errors which may eventually destroy the stability of the evolution. A reinitialization procedure is therefore periodically employed to reshape the LSF to be a signed distance function (SDF) [52, 56, 60, 104]. This reinitialization procedure, however, may affect the numerical accuracy of the solution and increase computational complexity. To this end, a number of reinitialization-free variational level set formulations, which intrinsically maintain the regularity of the level set function during the level set evolution, have been proposed [70, 103]. For example, DRLSE proposed in [103] eliminates the need for re-initialization by defining an energy functional with a distance regulariza-

tion term that is able to maintain a desired shape of the LSF; particularly a signed distance profile near the zero level set. Other re-initialization free methods based on the principles introduced by DRLSE include the work of Yu *et al.* [105] and that of Prakash *et al.* [106].

In this work, a variational level set formulation is employed in which the LSE minimizes an objective energy functional that employs a distance regularization term based on that proposed in [103] . The next section details our proposed method.

4.3 Weighted Level Set Evolution

For medical image segmentation applications using variational level set methods, a variety of image information, such as intensity, edge or texture, can be used to define an objective functional. Here, edge information is employed as the main image feature that drives the evolving contour to the desired boundary. The edge indicator function (2.14) is used to acquire information about the intensities of edges. Based on g, the following basic energy functional for an LSF ϕ defined as:

$$\mathcal{E}(\phi) = \mathcal{R}(\phi) + Length(\phi) + Area(\phi) \tag{4.5}$$

where $\mathcal{R}(\phi)$ is the distance regularization term introduced in [103], and $Length(\phi)$ and $Area(\phi)$ are length and area energy terms, respectively. $Length(\phi)$ is related to the energy along the length of the evolving contour C, i.e., for the case where ϕ =0; while $Area(\phi)$ is related to the energy of the area inside of C, i.e., for the case where ϕ >=0 [see Equation (4.1)]. These two energy terms can be defined so that the overall energy is minimized at the desired boundaries according to the edge indicator in Equation (2.14):

$$Length\{\phi = 0\} = \int_{\Omega} g\delta(\phi)\,|\nabla\phi|\,d\mathbf{x} \tag{4.6}$$

and

$$Area\{\phi \geq 0\} = \int_{\Omega} gH(\phi)d\mathbf{x} \tag{4.7}$$

where H is the Heaviside function. Note that according to Equation (4.6)-(4.7), the minimization of the these two energy terms depends heavily on the amount of edge information in the image. The Dirac delta function δ in Equation (4.6) is used to compute a line integral of the edge indicator function g along the zero level set of ϕ. The Heaviside function in Equation (4.7), on the other hand, is used to compute the energy of the area inside the evolving contour C. $Length(\phi)$ is then minimized when the zero level set of ϕ is located at the object's boundary, while $Area(\phi)$ serves as a way to control the evolution speed of the zero level set. In smooth regions, $Area(\phi)$ speeds up the evolution. In regions with a high number of edges, $Area(\phi)$ slows down the evolution, which helps the contour to conform to the desired boundary. For cases in which the image comprises smooth regions delimited by strong edges, the minimization of the energy functional in Equation (4.5) provides excellent boundary detection results. However, for cases where the image comprises regions with intensity inhomogeneities or delimited by weak edges, such as in medical images, the evolution process may result in inaccurate boundary detection or leakages. In this work we interested in improving the accuracy of the evolution process in conforming to the desired boundaries in cases where edges are weak, and regions contain intensity inhomogeneities. To this end, a weighting function is proposed to assign different priorities to the area and length terms according to the image features of the adjacent region located inside and outside of C. These features are the average edge intensity, denoted by $\mathcal{I}$, and average difference between the direction of the image's GVF and the normal direction of movement of C, denoted by γ. Note that analyzing the adjacent region located both inside and outside of C provides an accurate insight of edges location, which helps the zero level set to accurately conform to the desired boundary [107].

The proposed length and area terms then include a weighting factor, ω, that determines their importance in locating the desired boundary according to local image features. These terms are defined as:

$$Length_2\{\phi = 0\} = \int_{\Omega} g(1 - \omega(\phi, k))\delta(\phi) \left|\nabla\phi\right| d\mathbf{x} \tag{4.8}$$

and

$$Area_2\{\phi \geq 0\} = \int_{\Omega} g\omega(\phi, k)H(\phi)d\mathbf{x} \tag{4.9}$$

where k is a constant that determines the size of the region adjacent to C from where local features are obtained. Weight $\omega(\phi, k)$ is given by:

$$\omega(\phi, k) = \mathcal{I}(\phi, k)^{(1-\gamma(\phi,k))} \tag{4.10}$$

where $\mathcal{I} \in [0, 1]$ is the average intensity of the edge indicator along $2k$ contours adjacent to C; $\gamma \in [-1, 1]$ is the inner product between the normal of C, $\vec{N} = \nabla\phi/\left|\nabla\phi\right|$, and the GVF field along $2k$ contours adjacent to C. A contour adjacent to C is calculated as follows:

$$\psi(\phi, m) = \delta(\phi)\left|\nabla\phi\right| + m\vec{N} \tag{4.11}$$

where $m \in \mathbb{Z}$ and its sign denotes if the adjacent contour is located outside $(+)$ or inside $(-)$ of C. Note that with the Dirac delta function, the term $m\vec{N}$ in Equation (4.11) results in a contour displaced from the zero level set of ϕ by m units in its normal direction. This is illustrated in Figure 4.1.

The average intensity of the edge indicator along the $2k$ adjacent contours is

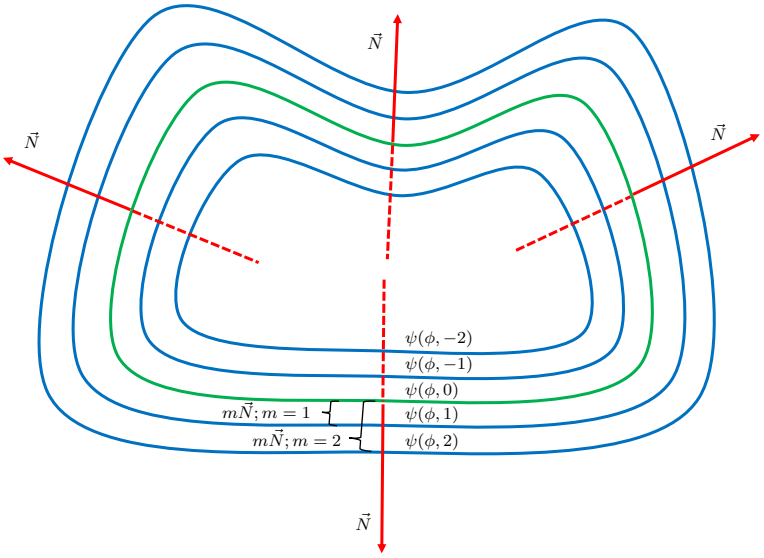

Figure 4.1: The green line represents the evolving contour C, i.e., the zero level set $\psi(\phi, 0)$. The blue lines represent the adjacent contours for $m = 1$, $m = -1$, $m = 2$ and $m = -2$, as specified in Equation (4.11)

calculated as follows:

$$\mathcal{I}(\phi, k) = \frac{1}{2k} \sum_{m=1}^{k} \left[\int_{\Omega} (1-g)\psi(\phi, m) d\mathbf{x} + \int_{\Omega} (1-g)\psi(\phi, -m) d\mathbf{x} \right] \tag{4.12}$$

Similarly to the length term in Equation (4.6), the integral in Equation (4.12) computes the line integral of the function $(1-g)$ along two contours adjacent to C; the first one located k units from C in its outside region, and the second one located k units from C in its inside region. Note that in Equation (4.12), the inverse value of the edge indicator g, i.e., $(1-g)$, is used to determine if the $2k$ adjacent contours are located in areas with strong edge information.

It is observed that the direction of the image's GVF field is a good estimator of the orientation and direction of edges [67]. Based on this observation, the alignment is calculated between the normal vector of C and the GVF field along the $2k$ adjacent contours , as illustrated in Figure 4.2. The average inner product γ is then calculated

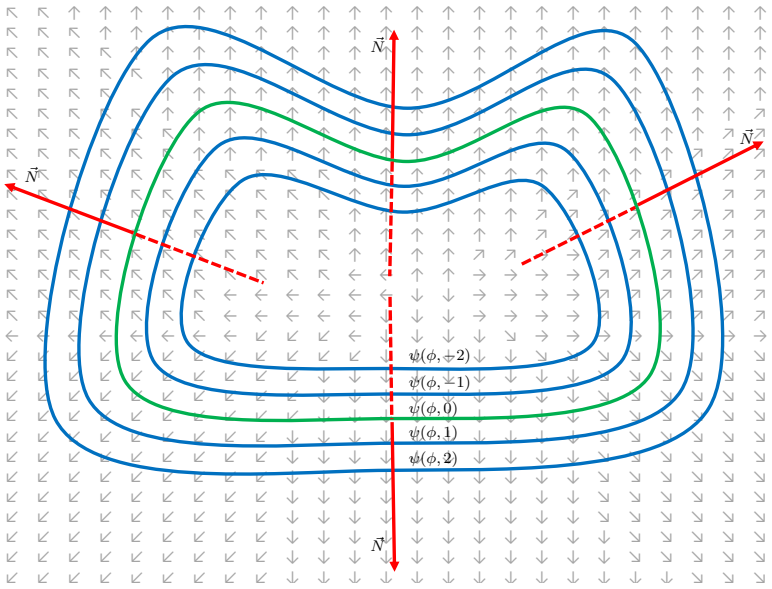

Figure 4.2: The red arrow represents the normal direction of movement of the evolving contour C. Gray arrows represent the GVF field vectors, $\vec{V}$. The figure shows the case of $k = 2$.

as follows:

$$\gamma(\phi,k) = \frac{1}{2k}\sum_{m=1}^{k}\left[\int_{\Omega}\left\langle \vec{N},\vec{V}\right\rangle \psi(\phi,m)d\mathbf{x} + \int_{\Omega}\left\langle \vec{N},\vec{V}\right\rangle \psi(\phi,-m)d\mathbf{x}\right] \tag{4.13}$$

where $\vec{V}$ denotes the image's GVF field. In this case, the integral in Equation (4.13) computes the line integral of the inner product between $\vec{N}$ and $\vec{V}$ along the contours adjacent to C. Note that γ results in values close to 1 when the normal vector of C aligns with $\vec{V}$.

By replacing $Length(\phi)$ and $Area(\phi)$ in Equation (4.5) with $Length_2(\phi)$ and $Area_2(\phi)$ as formulated in Eq (4.8) and (4.9), respectively, our proposed energy

functional is then defined as:

$$\mathcal{E}(\phi) = \mu \int_{\Omega} p(|\nabla\phi|)d\mathbf{x} + (1-\omega(\phi,k)) \int_{\Omega} g\delta(\phi)\,|\nabla\phi|\,d\mathbf{x} + (\omega(\phi,k)) \int_{\Omega} gH(\phi)d\mathbf{x} \tag{4.14}$$

where $\mu > 0$ is a constant, and $p(s) \triangleq \frac{1}{2}(s-1)^2$ is a potential (or energy density) function with a minimum point $s = 1$ that minimizes the distance regularization term $\mathcal{R}$ when $|\nabla\phi| = 1$ [103]. The energy functional in Equation (4.14) can then be minimized by solving a gradient flow as follows:

$$\frac{\partial\phi}{\partial t} = \mu\mathbf{div}(d_p(|\nabla\phi|)\nabla\phi) + (1-\omega(\phi,k))\delta(\phi)\mathbf{div}(g\frac{\nabla\phi}{|\nabla\phi|}) + \omega(\phi,k)g\delta(\phi) \tag{4.15}$$

where d_p is a function defined using the first derivative of $p(s)$ as $d_p(s) \triangleq \frac{p'(s)}{s}$ [103]. It is important to mention that in Equation (4.15), the weighting term $\omega(\phi,k)$, although expressed as a function of ϕ and k, results in a constant value in the range $[0,1]$. Consequently, it is regarded as a constant when computing the partial derivative with respect to time t. The weighting function $\omega(\phi,k)$ assigns different priorities to the length and area terms according to local image features. These features are the edge intensity, $\mathcal{I}$, and the degree of alignment, γ, between $\vec{V}$ and C's normal direction of movement. Figure 4.3 shows the plot of $\omega(\phi,k)$ for various values of $\mathcal{I}$ and γ. It can be seen that ω approaches 0 for large $\mathcal{I}$ values regardless of the value of γ, i.e., when the zero level set is located in a non-smooth region. In this case, the $Length_2$ term acts as the main energy driving the zero level set to the object's boundary. It can also be seen that ω approaches 1 for small $\mathcal{I}$ values regardless of the value of γ. In this case, the $Area_2$ term acts as the main energy driving the zero level set towards the object's boundary within a smooth region. For values of γ close to 1, the value of ω slowly decreases as $\mathcal{I}$ increases. In this

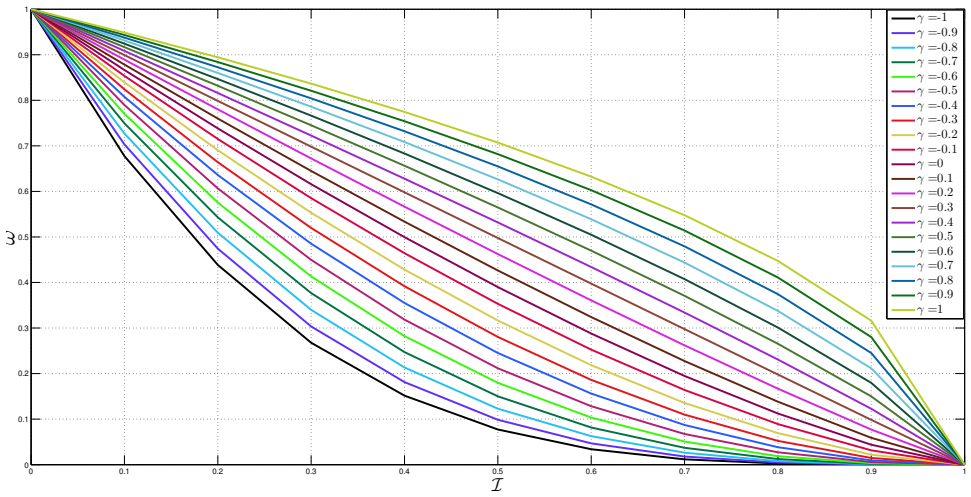

Figure 4.3: Value of ω for different values of $\mathcal{I}$ and γ.

case, the normal direction of movement of C aligns with the direction of the image's GVF field, therefore the $Area_2$ term acts as the main energy term. For values of γ close to -1, the value of ω slowly decreases as $\mathcal{I}$ increases. In this case, the normal direction of movement of C is opposite to the direction of the image's GVF field, therefore the $Length_2$ term acts as the main energy term helping C to conform to the object's boundary.

Weight ω allows C to deform in relatively smooth areas even if its normal direction of movement is opposite to the GVF field surrounding C. This is particularly useful when initializing the contour far from the desired boundary, even in regions with intensity inhomogeneities. Figure. 4.4(a)-(b) illustrate this case, where ω approaches 1. Weight ω also minimizes leakages around weak edges by determining the influence of the energy terms in the evolution process according to the average intensities of edge information and the average direction of the GVF field in the inside and outside regions adjacent to C. This is illustrated in Figure. 4.4(c), where the value of ω slowly approaches 0. Finally, weight ω allows C to conform to the desired boundary by assigning a larger weight to the $Length_2$ term where strong edges are encountered in the inside and outside regions adjacent to C. This is illustrated in Figure. 4.4(d), where the value of ω approaches 1.

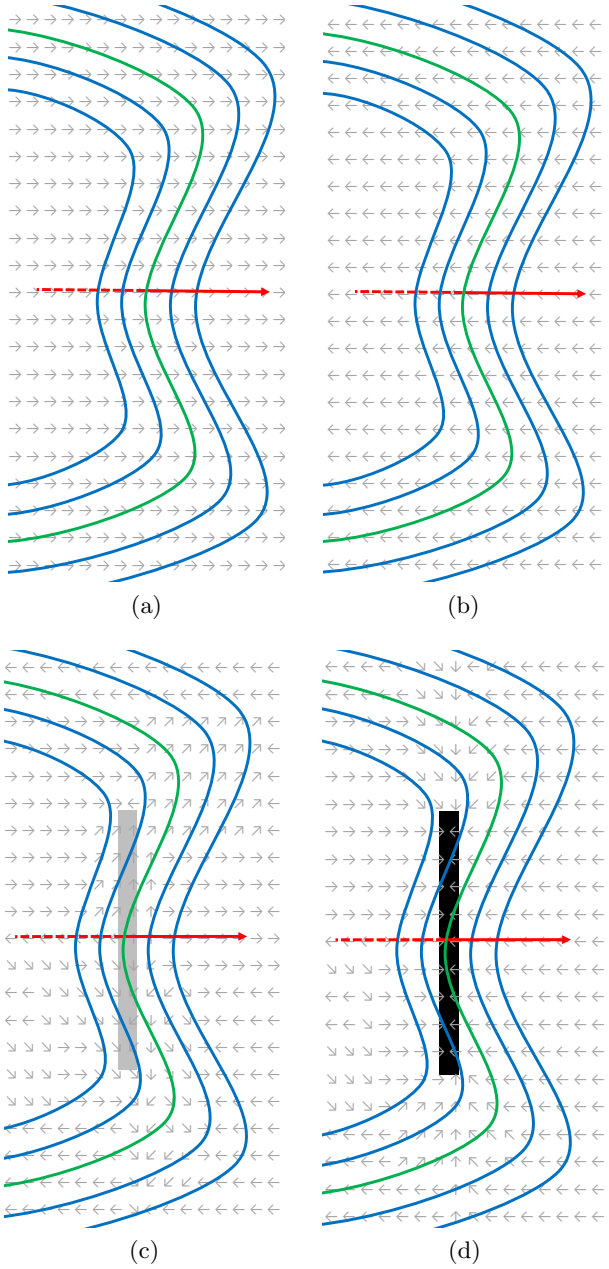

Figure 4.4: The normal direction of movement of C for different cases, represented by the red vector. Gray vectors represent the direction of the image's GVF field. Contour C is represented in green, weak edge information is represented by gray pixels and strong edge information is represented by black pixels. (a) The direction of the GVF field is similar to the normal direction of movement of C in a smooth region. (b) The direction of the GVF field is opposite to the normal direction of movement of C in a smooth region. (c) The direction of the GVF field around weak edges. (d) The direction of the GVF field around strong edges.

Implementation considerations

The proposed method is implemented using the narrowband approach in order to reduce the computational cost associated with the LSE [61]. This narrowband implementation only requires the LSF to be updates for each iteration by using a finite difference equation that discretizes the LSE [103]. This is done by defining the LSF ϕ on a grid and updating the LSF, for each iteration. This update is done on the narrowband, which is also defined on the grid. Let us denote the discretized form of a time-dependent LSF $\phi(x, y, t)$ by $\phi^{\tau}_{i,j}$, where (i, j) denotes the spatial position within a grid and τ denotes a discrete time instant. The finite difference equation that implements the LSE is then:

$$\phi^{\tau+1}_{i,j} = \phi^{\tau}_{i,j} + \Delta t L(\phi^{\tau}_{i,j}),\ \tau{=}0{,}1{,}2{,}\ldots \tag{4.16}$$

where Δt denotes a time step, and L is an approximation of the gradient flow in Equation (4.15) [108]. As previously stated in Sec. 4.3, term $\omega(\phi, k)$ is regarded as a constant value with respect to time. The computation of $\mathcal{I}(\psi(\phi, k))$ and $\gamma(\psi(\phi, k))$ is also done in a discretized manner within a grid. Let us denote the discretized zero level set of $\phi(x, y, t)$ at time instant τ by C_{τ}. The location of C_{τ} within a grid is used to compute the location of the $2k$ adjacent contours. The line integrals in Equation (4.12) and Equation(4.13) are then computed in discretized form as a summation over all grid points along the $2k$ adjacent to C_{τ}, as exemplified in Figure. 4.5. The resulting value of $\omega(\phi, k)$ at time instant τ is then used to update the LSF for the next iteration, i.e., time instant $\tau + 1$, according to Equation (4.16).

4.4 Experimental Results

In this section, we apply our proposed method to segment different regions on various types of real medical images, including a number of synthetic images. The proposed method is compared to state-of-the-art edge-based level-set methods, specifically

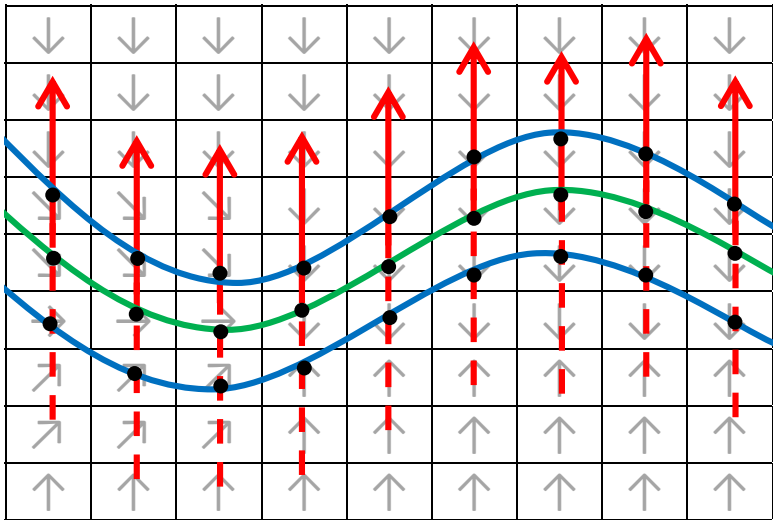

Figure 4.5: Example of an LSF defined on a grid. The green line represents the evolving contour C, i.e., the zero level set $\psi(\phi, 0)$. The blue lines represent the contours adjacent to C according to the k value in Equation (4.11); in this figure $k = 1$. Edge intensity and GVF field values at the the black points along the adjacent contours are used to compute weighting factor ω in Equation (4.10).

(RD) [70], (LSD) [101] and (DRLSE) [103]. Also, the proposed method is compared to Kimmel's method [67], since this method, despite being region-based, shares many similarities with our method.

Four sets of experiments are conducted to evaluate the performance of our proposed method. In all experiments, we set the initial LSF to be a binary function whose values have positive and negative signs inside and outside the initial contour, respectively. Table 4.1 shows the parameters used for the edge-based methods evaluated in this work, including our method. Parameters μ, α and λ are constants that determine the influence of the regularization term, area and length terms, respectively. Let us recall that in our proposed method, the influence of the area and length terms is determined by weight $w(\phi, k)$. Note that the sign of α is responsible for inflation (+) or deflation (-) of the contour.

For images with weak object boundaries and low contrast, a large value of α may cause boundary leakage. In this case the value of α should be chosen relatively small to avoid boundary leakage. DRLSE is not sensitive to the choice of α and λ,

Table 4.1: Parameters used in evaluated edge-based methods

	μ	α	λ	Δt	Δt_2
LSD	0.2	-1	1	0.5	-
RD	-	-1	1	0.8	0.1
DRLSE	0.2	-3	5	1	-
Proposed Method	0.2	-	-	1	-

which can be fixed for most applications. It is important to note that the values of α and λ in LSD and DR are smaller in comparison to DRLSE. This is because LSD and RD use the Dirac function in Equation (4.17), which is different from the Dirac function used in DRLSE [see Equation (4.18)]. The Dirac function affects the energy terms in the energy functional. In order to compensate for the differences in these two Dirac functions, we use smaller values for α and λ in LSD and RD. These values are equivalent to the values selected for DRLSE.

The reason for employing smaller Δt values in LSD than in the other methods is due to its fast deformation speed. Therefore, a large Δt value for the other methods used, so all comparisons are fair in terms of deformation speed.

$$\delta_2(x) = \frac{\varepsilon}{\pi\left(\varepsilon^2 + x^2\right)} \tag{4.17}$$

$$\delta_1(x) = \begin{cases} \frac{1}{2\varepsilon}\left[1 + \cos\left(\frac{\pi x}{\varepsilon}\right)\right], & |x| \leq \varepsilon \\ 0, & |x| > \varepsilon \end{cases} \tag{4.18}$$

In all experiments, the detection accuracy of the evaluated methods is measured by the DSC [see Equation 3.17 in chapter 3].

4.4.1 Analysis of parameter k

The first set of experiments is designed to characterize the effect of parameter k in the boundary detection results and to provide an intuitive interpretation to the tuning of this parameter. Figure 4.6 shows the boundary detection results on a

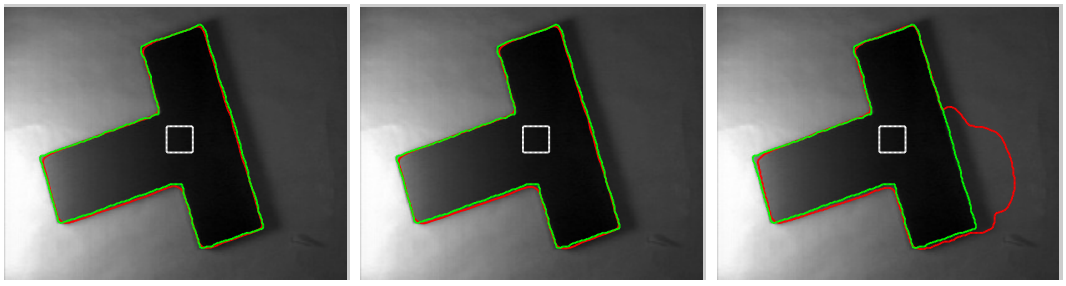

(a) (b) (c)

Figure 4.6: Boundary detection results of the proposed method on a synthetic image with 120 iterations and different values for parameter k. (a) $k = 2$ (DSC=0.9802). (b) $k = 3$ (DSC=0.9798). (c) $k = 6$ (DSC=0.8057). White curves denote the initial contour; red curves denote the final contour, and green curves denotes the ground truth.

synthetic image for different values of k, which results in different values for the weighting term $\omega(\phi, k)$, as the number of contours adjacent to C increases as k increases. It is clear that there is a trade-off between the value of k and the strength of the energy terms, i.e., the area and length terms in Equation (4.14). A large value of k implies collecting local features in a larger region adjacent to C, which may result in an inaccurate description of this region and thus, leakage (see Figure 4.6(c)). Smaller values of k may lead to more accurate segmentation results, as this implies collecting local features in a region very close to contour C (see Figure 4.6(a)) .

We have evaluated the effect of parameter k on a synthetic image with both, different number of iterations and different initial contours. Tables 4.2 and 4.3 tabulate the DSC values for these results. Fig. 4.7 shows the initialization positions on the synthetic image. It is clear that DSC values slowly decrease when the value of k increases. As expected, as the number of iterations increases, DSC values increase. This is due to the fact that with more iterations, the contour gets closer to convergence. Results for $k = 1$ and $k = 2$ are quite similar. However, $k = 2$ provides a better insight of the edge information surrounding the evolving contour. Therefore, we use $k = 2$ in all of our experiments.

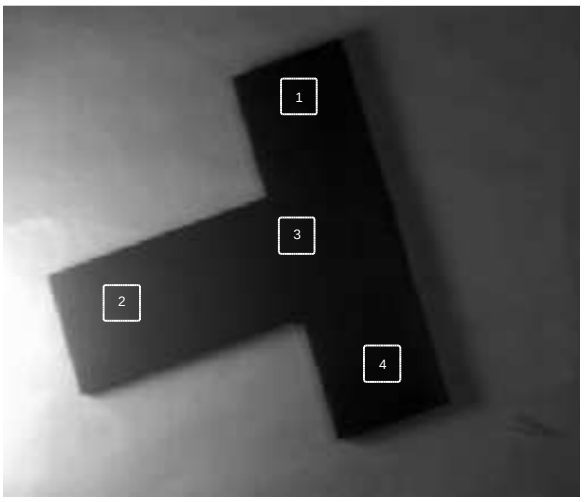

Figure 4.7: Different positions for the initial contour on the test synthetic image.

Table 4.2: DSC values for the synthetic image for $k = 1$

Initial Position	Number of iterations						
	80	100	120	140	160	180	200
1	0.9650	0.9784	0.9808	0.9814	0.9814	0.9810	0.9806
2	0.8320	0.9660	0.9806	0.9809	0.9805	0.9806	0.9804
3	0.8889	0.9566	0.9773	0.9807	0.9816	0.9818	0.9815
4	0.8802	0.9557	0.9770	0.9801	0.9811	0.9814	0.9810

Table 4.3: DSC values for the synthetic image for $k = 2$

Initial Position	Number of iterations						
	80	100	120	140	160	180	200
1	0.9641	0.9778	0.9802	0.9809	0.9811	0.9805	0.9803
2	0.8693	0.9742	0.9806	0.9806	0.9801	0.9802	0.9800
3	0.8932	0.9579	0.9802	0.9804	0.9810	0.9812	0.9811
4	0.8649	0.9498	0.9746	0.9794	0.9806	0.9809	0.9806

In images with regions delimited mostly by well-defined edges, $k = 1$ indeed provides very similar results to the ones obtained by using $k = 2$. However, for images with regions delimited by mostly weak edges, a value of $k = 1$ may result in an less accurate segmentation than that obtained with a value of $k = 2$. This is due to that fact that a value of $k = 2$ increases the analysis region around the zero level-set, allowing to collect more edge features. In order to cover both cases, i.e, those cases where most of the edges are well defined and those where most of the edges are weak, we increase the analysis region around the zero level-set by setting $k = 2$.

In order to show that a value of $k = 2$ indeed results in more accurate segmentation results than those obtained with a value of $k = 1$ for regions delimited by mostly weak edges, we have evaluated our method on two additional MRI slices of lumbar discs, with $k = 1$ and $k = 2$ as shown in Figure. 4.8 and Figure 4.9. Note that the regions to be segmented in these experiments are not well-defined and have mostly weak edges. Results show that our method successfully detects the objects' boundary with $k = 2$. Specifically, the proposed method with $k = 2$ achieves higher DSC values than the case of using $k = 1$. Therefore, we use $k = 2$ in the remaining experiments to define the number of adjacent contours used to collect local features.

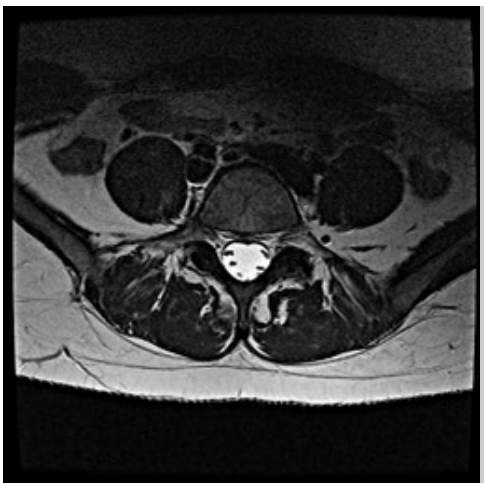

(a)

$k = 1$ $k = 2$

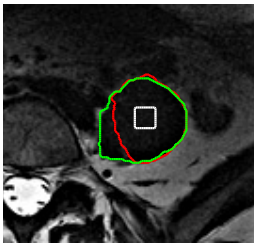
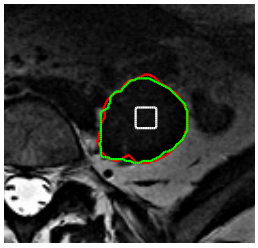

(b) DSC=0.8851,Itr=80 (c) DSC=0.9678,Itr=80

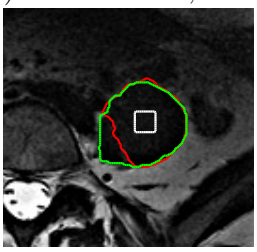
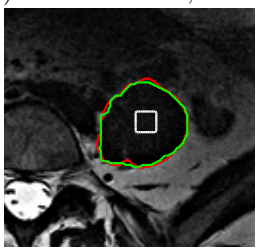

(d) DSC=0.8952,Itr=100 (e) DSC=0.9686,Itr=100

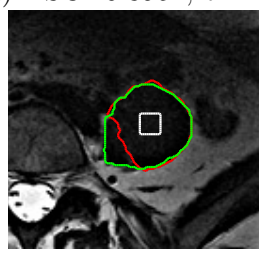
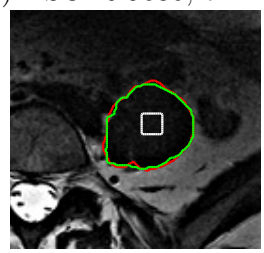

(f) DSC=0.8949,Itr=120 (g) DSC=0.9684,Itr=120

Figure 4.8: MRI slice of an abdominal axial cross sectional view of human body. The white curves denote the initial contours, the red curves represent the final contour and the green curves represent the ground truth.

(a)

$k = 1$ $k = 2$

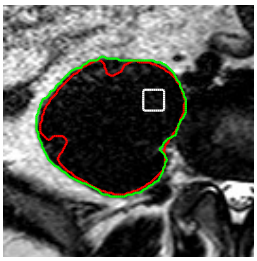
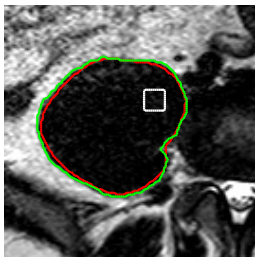

(b) DSC=0.9382,Itr=100 (c) DSC=0.9613,Itr=100

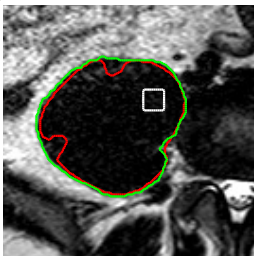
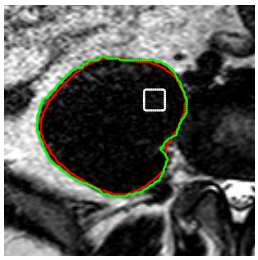

(d) DSC=0.9417,Itr=120 (e) DSC=0.9641,Itr=120

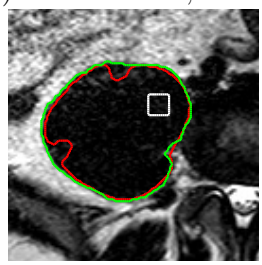
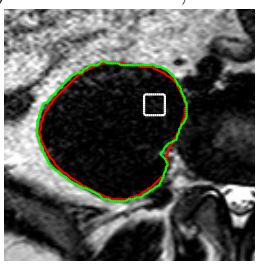

(f) DSC=0.9438,Itr=140 (g) DSC=0.9660,Itr=140

Figure 4.9: MRI slice of an abdominal axial cross sectional view of human body. The white curves denote the initial contours, the red curves represent the final contour and the green curves represent the ground truth.

4.4.2 Results on real medical images

The second set of experiments evaluates the proposed method on real medical images and compares it with LSD, RD and DRLSE. This experiment is divided in two parts. In Part 1, the number of iterations for all evaluated methods is set to the number required to achieve convergence in our method. In Part 2, we increase the number of iterations used in Part 1 in order to evaluate the accuracy of LSD, RD and DRLSE as the number of iterations in Part 1 increases. Table 4.4 tabulates the DSC values for different regions of MRI and CT slices. Images 1-15 represent different regions on different MRI slices of a spinal cord, images 16 represents a region on an MRI slice of a brain (the caudate nucleus is the object to be segmented), images 17 and 18 represent two regions on an MRI slice of a pelvis; images 19 and 20 represent two regions on a CT slice of a skull, and images 21-28 represent different regions on different MRI slices of lumbar discs. These last set of experiments represent challenging cases where the target regions have intensities very similar to those of the surrounding regions, thus making it difficult to clearly delineate the objects' boundaries. It is important to mention that the images used in Chapter 2 are subset of the data-set used in this chapter.

Results in Table 4.4 show that our approach achieves the highest accuracy for the majority of experiments. The methods whose results are underlined in Table 4.4 achieve convergence before the proposed method and thus remain stable as the algorithms iterate further. In images 2, 14-17, Part 1, and images 11,13,15,17, Part 2, the other evaluated methods achieve higher DSC values than our method. In the case of Experiment 2, Part 1, RD does not converge in the tabulated number of iterations, and more iterations cause significant leakage in Part 2. In the case of images 14-17, Part 1, DRLSE achieves convergence before our proposed method (underlined results), thus resulting in higher DSC values. For the case of images 14 and 16, after increasing the number of iterations in Part 2, our method achieves higher DSC values. Our method, in these two cases, requires a larger number of

Table 4.4: Segmentation accuracy of various level set methods for real medical images.

Image	Part 1					Part 2				
	DSC				NO. iterations	DSC				NO. iterations
	LSD	RD	DRLSE	Proposed approach		LSD	RD	DRLSE	Proposed approach	
1	0.9262	0.9468	0.9432	**0.9549**	50	0.7246	0.9203	0.8438	**0.9551**	80
2	0.9370	**0.9437**	0.9016	0.9315	50	0.7868	0.5297	0.8913	**0.9247**	100
3	0.9451	0.9679	0.9501	**0.9686**	50	0.6873	0.5651	0.6082	**0.9686**	100
4	0.9391	0.9560	0.9311	**0.9595**	50	0.7638	0.8676	0.8741	**0.9590**	60
5	0.9368	0.9603	0.9552	**0.9636**	50	0.5563	0.9277	0.9544	**0.9617**	100
6	0.8814	0.9254	0.9166	**0.9340**	50	0.7695	0.8940	0.8205	**0.9352**	100
7	0.9085	0.9330	0.9412	**0.9589**	50	0.7233	0.4730	0.9397	**0.9582**	100
8	0.9417	0.8375	0.9165	**0.9543**	50	0.7041	0.8200	0.7235	**0.9538**	100
9	0.8128	0.8234	0.9445	**0.9472**	50	0.9364	0.9422	0.9461	**0.9479**	100
10	0.9070	0.8745	0.9332	**0.9468**	50	0.8609	0.9067	0.9335	**0.9468**	100
11	0.8821	0.8944	0.9420	**0.9484**	50	0.9218	**0.9541**	0.9434	0.9487	100
12	0.7934	0.8006	0.8123	**0.9565**	50	0.9055	0.8176	0.8152	**0.9569**	100
13	0.7150	0.7081	0.9526	**0.9674**	50	0.7392	**0.9560**	0.9252	0.9538	100
14	0.8875	0.9058	**0.9463**	0.9443	50	0.9015	0.9437	0.9466	**0.9500**	100

Image	Part 1					Part 2				
	DSC				NO. iterations	DSC				NO. iterations
	LSD	RD	DRLSE	Proposed approach		LSD	RD	DRLSE	Proposed approach	
15	0.8496	0.7589	**0.9577**	0.9444	50	0.9466	0.9527	**0.9571**	0.9482	100
16	0.9584	0.7747	**0.9764**	0.9670	50	0.7848	0.9507	0.9776	**0.9791**	100
17	0.9397	0.7643	**0.9641**	0.9516	50	0.6591	0.9294	**0.9767**	0.9727	100
18	0.8643	0.8794	0.8510	**0.9157**	50	0.8076	0.8379	0.8510	**0.9157**	100
19	0.6376	0.6416	0.7355	**0.9565**	100	0.6844	0.7267	0.9480	**0.9648**	140
20	0.7095	0.7388	0.9273	**0.9632**	100	0.7971	0.8418	0.8680	**0.9632**	140
21	0.6792	0.7703	0.8874	**0.9216**	60	0.7812	0.8837	0.8314	**0.9183**	80
22	0.8504	0.8371	0.9032	**0.9290**	60	0.8603	0.8581	0.8877	**0.9270**	80
23	0.6527	0.7080	0.9182	**0.9389**	60	0.7004	0.8524	0.8968	**0.9372**	80
24	0.9057	0.8907	0.8920	**0.9406**	60	0.8852	0.8697	0.8816	**0.9361**	80
25	0.5701	0.6172	0.8365	**0.9385**	60	0.6122	0.6472	0.9099	**0.9319**	80
26	0.6824	0.7349	0.8174	**0.9598**	70	0.7014	0.8119	0.8331	**0.9462**	90
27	0.8605	0.9119	0.8475	**0.9555**	50	0.9009	0.8400	0.7280	**0.9545**	80
28	0.7588	0.7512	0.8280	**0.8864**	100	0.7714	0.6939	0.8345	**0.8844**	130
Average	0.8333	0.8306	0.9046	**0.9466**		0.7812	0.8291	0.8767	**0.9464**	

iterations than DRLSE to accurately detect the desired boundary. In the case of images 15 and 17, Part 2, DRLSE outperforms our method by only 0.670%. For images 11,13, Part 2, RD also outperforms our method by only 0.004%. It is also important to note that RD and LSD tend to result in leakage as the number of iteration increases; see for example images 2, 3 and 4, Part 2. For the challenging cases (Images 21-28), our method achieves convergence before the other evaluated methods and results in higher DSC values.

It is important to mention that leakage in DRLSE may be the result of the distance regularization term and area term forcing the zero level set to continue to evolve when the zero level set is already at the desired boundary. Even though our proposed method also employs the distance regularization employed by DRLSE, it prevents leakage and achieves convergence by weighting the $Length_2$ and $Area_2$ terms according to local image features.

Visual results for Part 1 images are shown in Figure 4.10. Note that the images in the depicted experiments contain several intensity inhomogeneities. The last two columns represent challenging cases where the target objects have intensities very similar to the surrounding regions. It can be seen that our method is capable of detecting regions delineated by weak edges. The other evaluated methods (see Rows 1-3 of Figure 4.10), fail to correctly segment the regions for the same number of iterations required by our method. Although RD and DRLSE attain an accuracy similar to that obtained by our method for Experiment 1 (first column of Figure 4.10), these methods fail when they are allowed to iterate further, as shown in Figure 4.11. Among the most challenging regions are those in Experiment 27 and 28 (last column of Figure 4.10). In this case, our method successfully detects the cecum region (Experiment 27). This region is characterized by very weak edges. Note that all of the methods fail to correctly detect the upper edge of the sacrum region (Experiment 28). However, our method is the one that results in the least amount of leakage and thus, the highest DCS value.

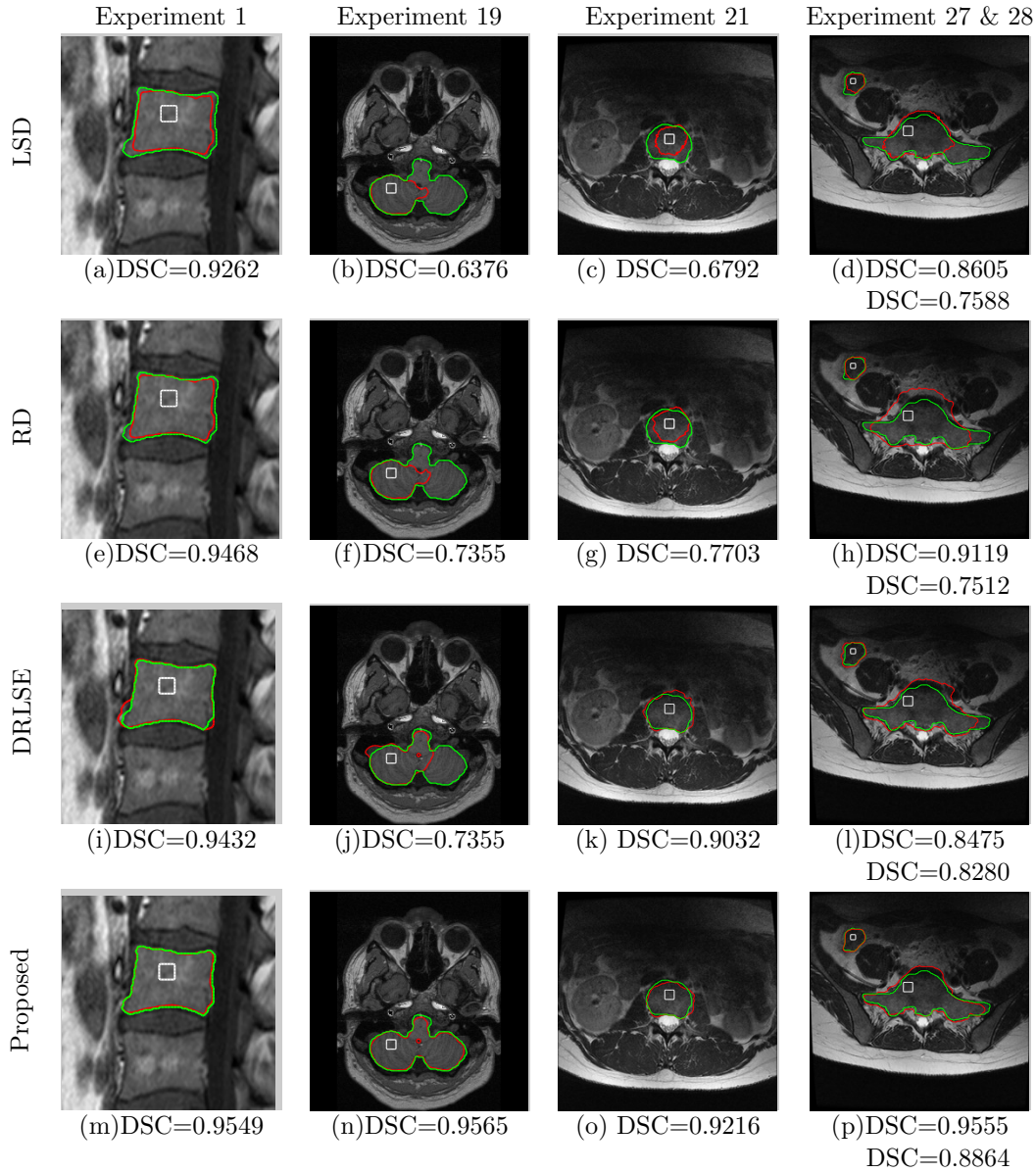

Figure 4.10: Visual results for Part 1 experiments. The white curves denote the initial contours, the red curves represent the final contour, and the green curves represent the ground truth. For images 27 & 28, the first line of DSC values is for the cecum region (upper region - Experiment 27), while the second line is for the sacrum region (bottom region - Experiment 28).

Visual results for Part 2 experiments are shown in Figure 4.11. Note that the other evaluated methods results in significant leakage when they iterate further. These visual results confirm that taking into account the amount of edge information and the direction of the image's GVF field in the adjacent region located inside and outside of the evolving contour to control the influence of various energy terms, can improve segmentation accuracy and minimize leakage.

4.4.3 Comparisons with region-based active contours

The third set of experiments compares our method to Kimmel's method on synthetic images and real medical images. Visual results and DSC values are shown in Figure 4.12. These results show that Kimmel's method outperforms ours for the synthetic image in Figure 4.12 (a). This is mainly due to the fact that Kimmel's method incorporates a region-based force into the model, which increases accuracy when two regions can be easily detected in the image. Our method, however, attains a very similar DSC value to that attained by Kimmel's in this image. For cases where no two regions can easily be detected, Kimmel's method is outperformed by ours. This is evidenced in the synthetic image in Figure 4.12 (b), where it is difficult to delineate two regions due to the weak edges and the intensity inhomogeneities. Similar results are obtained for the real medical images in Figure 4.12 (c) and (d). Our method achieves higher DCS values for these images. It is interesting to note the performance of Kimmel's method on the image in Figure 4.12 (d). As mentioned before, this method attempts to detect two homogeneous regions. Therefore, the detected two regions in this case correspond to those that appear to be the most similar regions in terms of intensities.

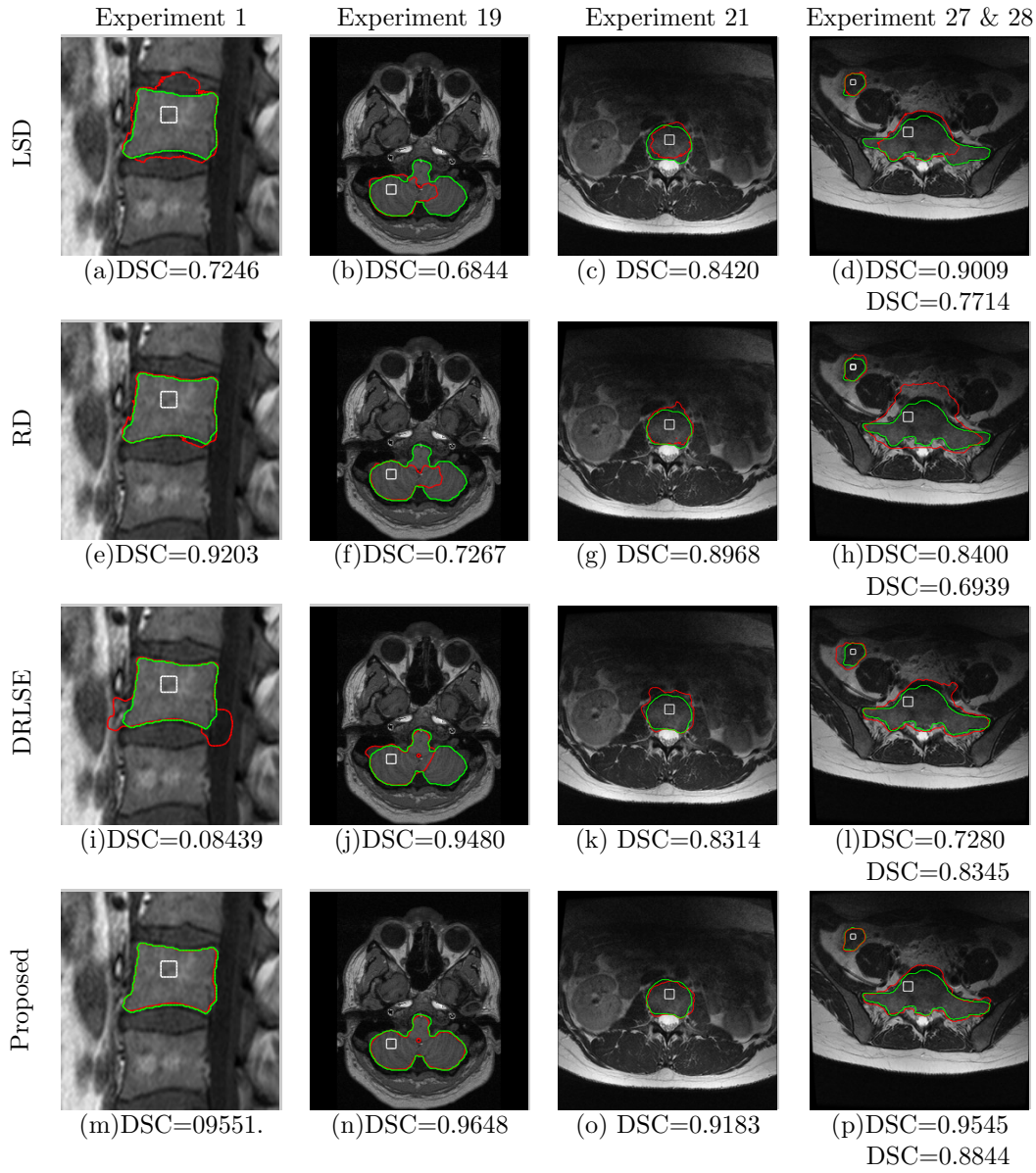

Figure 4.11: Visual results for Part 2 experiments. Rows from top correspond to LSD, RD, DRLSE and our proposed method, respectively. The white curves denote the initial contours, the red curves represent the final contour, and the green curves represent the ground truth. For images 27 & 28, the first line of DSC values is for the cecum region (upper region - Experiment 27), while the second line is for the sacrum region (bottom region - Experiment 28).

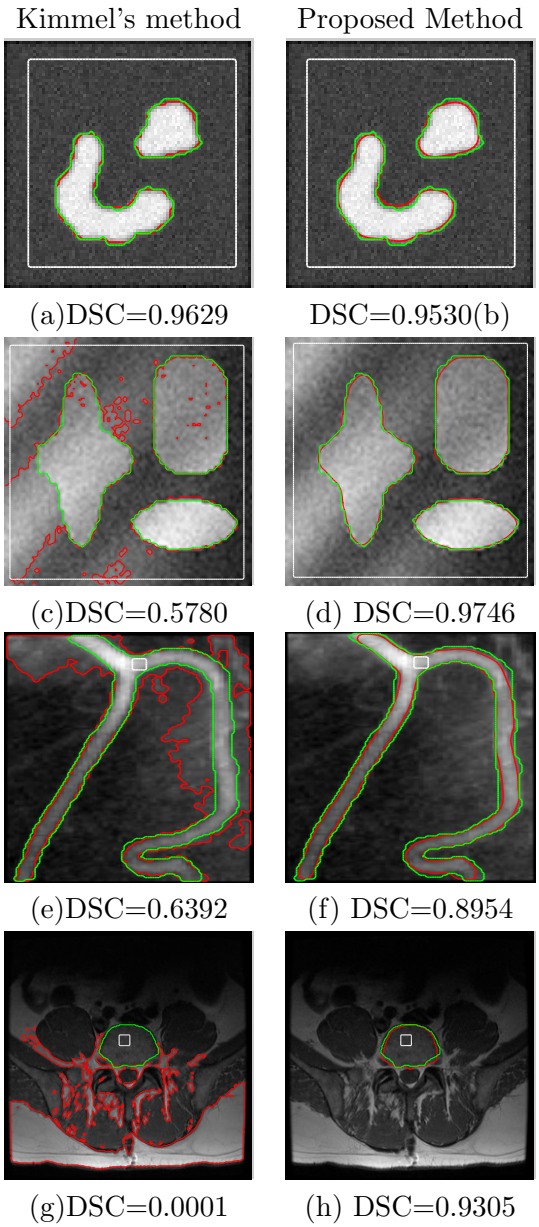

Figure 4.12: Visual results and DSC values for synthetic images (rows 1 and 2) and real medical images (rows 3 and 4). The first column corresponds to Kimmel's method, while the second column corresponds to our method. Column 3 depicts a X-ray vessel image, and column 4 depicts an MRI slice of an abdominal axial cross sectional view of the human body. The white curves denote the initial contours, the red curves represent the final contour and the green curves represent the ground truth.

4.4.4 Sensitivity to position of initial contour

The last set of experiments evaluates the sensitivity to the initial contour's position of all edge-based methods. To this end, different positions for the initial contour are employed on synthetic images and real medical images. Visual results and DSC values are shown in Figure 4.13 and 4.14. All methods have been evaluated with the same number of iterations. In Figure 4.13, we show results for a noisy synthetic image. In this case, we tested the case of initializing the contour inside and outside the target regions. These results show that our method successfully detects the objects' boundary even when the position of the initial contour is located outside the target regions. Our method also achieves the highest DSC values. Figure 4.14 demonstrates the robustness of the proposed method with different initial contours on a real medical image. In this case, RD performs better than LSD and DRLSE, as it is capable to conform to most of the desired boundary regardless of the position of the initial contour. LSD particularly fails when the initial contour is located close to a weak boundary. The proposed method successfully conforms to the desired boundary with high accuracy for all initialization positions. It is interesting to see that the proposed method results in very similar DSC values for this medical image regardless the position of the initial contour. Finally, in order to evaluate the performance on challenging cases, speckle noise with a variance of 0.04 is applied to the same medical image in Figure 4.14. We then tested the same initialization positions as those in Figure 4.14. Results are shown in Figure 4.15. This confirms the effectiveness of weight ω in our method to control the influence of forces according to local features.

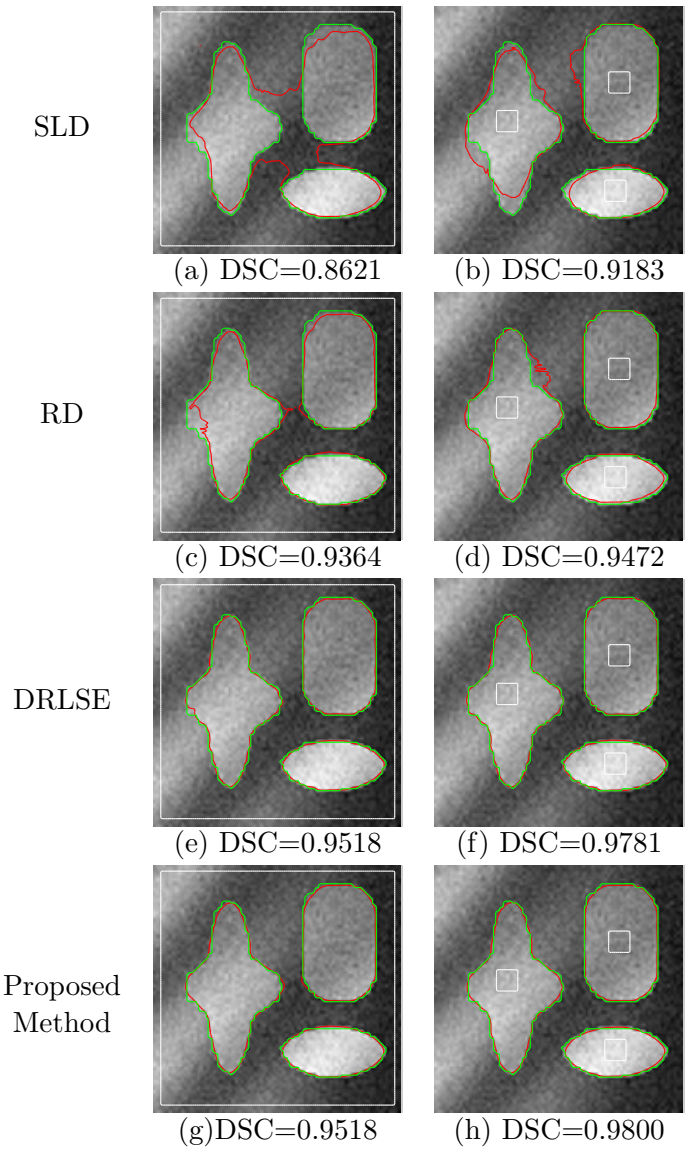

(a) DSC=0.8621 (b) DSC=0.9183

(c) DSC=0.9364 (d) DSC=0.9472

(e) DSC=0.9518 (f) DSC=0.9781

(g)DSC=0.9518 (h) DSC=0.9800

Figure 4.13: Segmentation results on a synthetic image after 100 iterations using different positions for the initial contour. The white curves denote the initial contours, the red curves represent the final contour and the green curves represent the ground truth. Each row shows results for a different initial position.

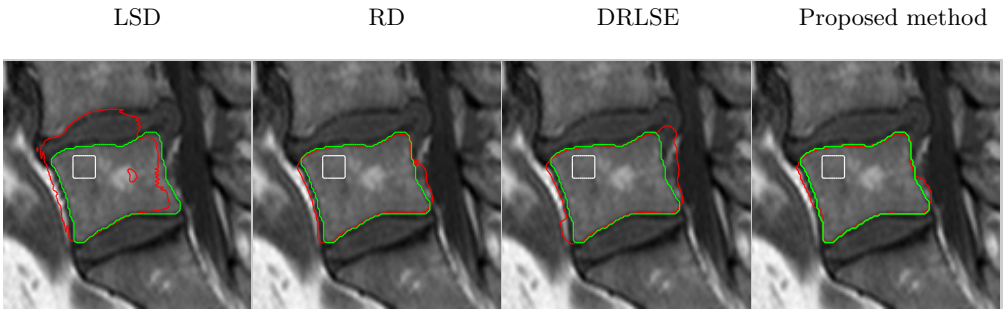

(a) DSC=0.7780 (b) DSC=0.9284 (c) DSC=0.8938 (d) DSC=0.9562

(e) DSC=0.7677 (f) DSC=0.8842 (g) DSC=0.7303 (h) DSC=0.9577

(i) DSC=0.7199 (j) DSC=0.7670 (k) DSC=0.8791 (l) DSC=0.9565

Figure 4.14: Segmentation results on a MRI slice of a spinal cord after 50 iterations using different positions for the initial contour. The white curves denote the initial contours, the red curves represent the final contour and the green curves represent the ground truth. Each row shows results for a different initial position.

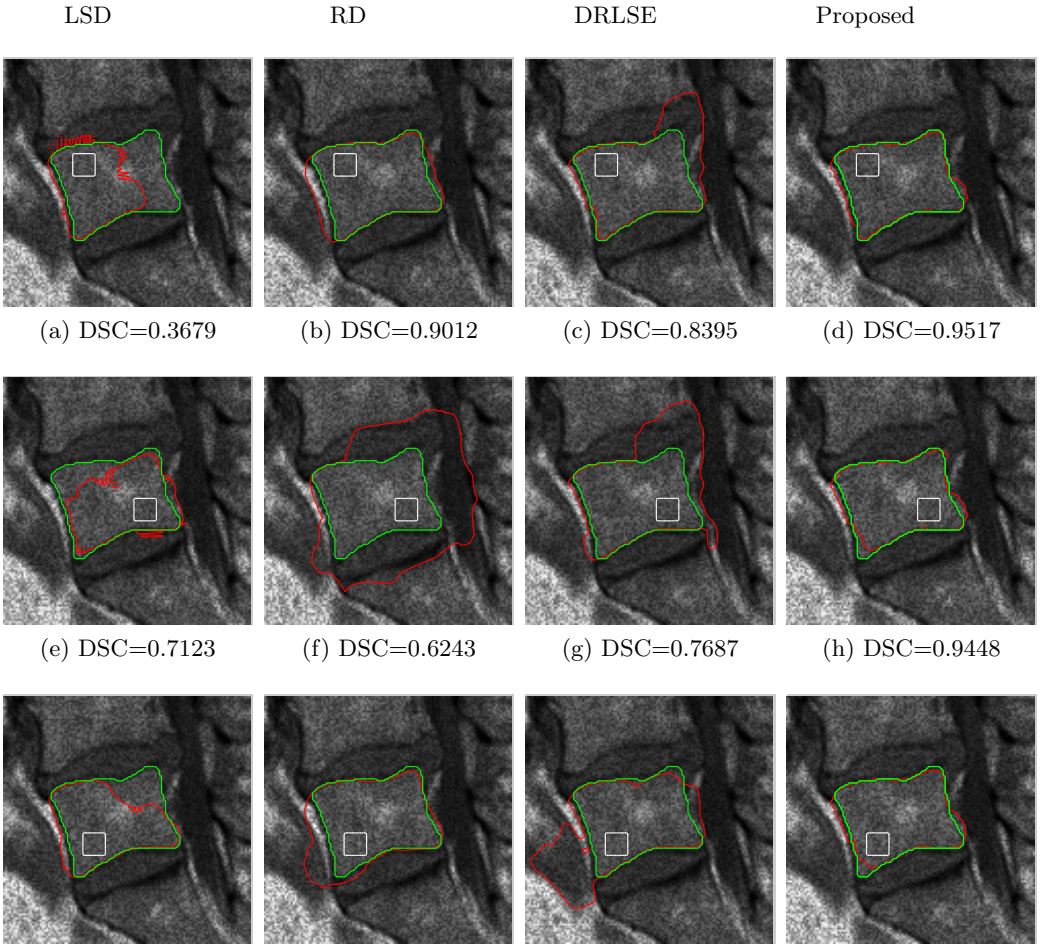

(a) DSC=0.3679 (b) DSC=0.9012 (c) DSC=0.8395 (d) DSC=0.9517

(e) DSC=0.7123 (f) DSC=0.6243 (g) DSC=0.7687 (h) DSC=0.9448

(i) DSC=0.7404 (j) DSC=0.8530 (k) DSC=0.7789 (l) DSC=0.9453

Figure 4.15: Segmentation results on a MRI slice of a spinal cord (with added noise) after 50 iterations using different positions for the initial contour. The white curves denote the initial contours, the red curves represent the final contour and the green curves represent the ground truth. Each row shows results for a different initial position.

Table 4.5: The average CPU time of the four segmentation algorithms.

Method	LSD	RD	DRLSE	Proposed
Time(s)	10.16	9.31	18.49	26.63

4.4.5 Computational complexity

Despite the advantages of the narrowband implementation, the computational cost of our method increases with respect to that of the other evaluated methods. This is mainly due to the fact that the proposed method collects local features from a number of contours adjacent to the evolving contour C, at each iteration.

The CPU time during the experiments is recorded. All methods are implemented in Matlab 8.4 and run on a computer with Intel (R) Core (TM) i5 CPU, 3.20 GHz, 16 GB RAM, with Windows 7. Table 4.5 shows the average CPU time of the 28 images tabulated in Part 1 of Table 4.4. Although LSD and RD attain lower average CPU times than those attained by DRLSE, the accuracy of these methods is, overall, lower than that of DRLSE. As expected, the proposed method takes longer CPU times to detect boundaries. However, these times may be easily reduced by introducing optimizations to the implementation code.

4.5 Summary

This chapter proposed a novel medical image segmentation method based on a level set active contour model that provides improved boundary detection accuracy around weak edges. The method uses a weighting factor to leverage the advantages of incorporating local image features into the objective energy functional. Specifically, the method combines edge intensity information with edge directional information collected from the adjacent region located inside and outside of the evolving contour. This information is then used to determine the importance of various energy terms in an energy functional. As a consequence, the proposed method is able to accurately drive the contour to the desired boundary even around weak edges, thus

minimizing leakages in medical images. The performance of the proposed method was demonstrated on various real medical images and was compared with the performance of various edge-based and region-based methods. Experimental results showed that the proposed method outperforms other state-of-the-art methods, in terms of segmentation accuracy, and is capable to converge to the desired boundary in less iterations.

We have shown that active contour has the potential of segmenting medical images delimited by weak edges, in next chapter, we will explore another way of applying active contour for overlapping cells. We can not apply the proposed the method in this chapter directly because overlapping cells characterised by weaker edges. Instead, we used a patch-based approach where we let an open counter evolves independently within small patches and then we connect them together to assemble the contour of an overlapping cell.

Chapter 5

Patch-Based Segmentation Using Local Information for Overlapping Cervical Cells

5.1 Introduction

Cervical cancer is one of the most common types of cancer among women [109]. Since the discovery of a screening test, namely the Pap test, a significant decrease has been observed in the incidence of cervical cancer and related deaths. The Pap test has been the most effective cancer screening test and remains the most important technique in detecting the precursor lesions for cervical cancer. The test is based on obtaining cells from the uterine cervix and then smearing them onto glass slides for microscopic examination to detect human papillomavirus (HPVs) effects. The Papanicolaou (Pap) method is then used to stain the slides, which makes analysis easier as different components of the cells show different colours.

There are generally three components (types) of cells can be seen on Pap smear images [see Figure 5.1]: 1) the superficial squamous cells, which are the largest of the three types with small nuclei and cytoplasm that usually appear in red; 2) the intermediate squamous cells, which are slightly smaller in size and have larger round nuclei with cytoplasm that usually appear in blue; and 3) the immature

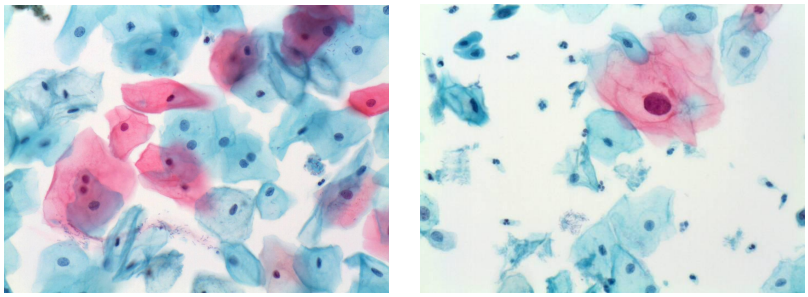

(a) (b)

Figure 5.1: Examples of overlapping cells with inconsistent staining and poor contrast, which corresponds to a more realistic and challenging setting.

cells, which appears smaller in compare with the other two types.

The sensitivity of the test is mainly affected by the number of cells sampled, the overlap among these cells, the poor contrast of the cell cytoplasm, and the presence of mucus, blood cells, and inflammatory cells [110]. Both intra- and inter-observer changes during the interpretation of abnormal smears contribute to the wide variation in false-negative results [111].

The associated difficulties in the manual screening process and the promise of early diagnosis have made the improvement of automated or semi-automated systems that analyse images using a digital camera connected to the microscope a critical research problem in which more robust, consistent, and quantifiable examination of the smears could increase the reliability of the diagnoses [112, 113]. These issues motivated the researchers to improve the techniques being used for both automated cell deposition and slide analysis. Cell deposition techniques purify cells from a significant portion of blood, mucus, and other debris. Also, they reduce the overlap between cells and provide cells that are more likely to occur in a single focal plane, and this makes the analysis of both manual and automated slides much faster and easier [114].

Automated slide analysis techniques improve both the sensitivity and specificity of screening, which involves two main tasks: segmentation and classification. Segmentation mainly focuses on detecting and segmenting cells boundaries, then sep-

arating them from the background, as well as detecting and segmenting the nuclei from the cytoplasm within the cell regions. Automatic thresholding, morphological operations, and active contour models appear to be the most traditional methods in segmentation of the nuclei from isolated or partially overlapping cells [110]. Whereas classification tasks focus on classifying individual cells present on a slide [115–119].

5.1.1 Nuclei Segmentation

Several authors have proposed methods that attempt to detect and segment the nuclei cells from cervical cells. Bamford and Lovell [120] propose a method to segment the nucleus in a Pap smear image using a dual active contour model. They use a Viterbi search-based dual active contour algorithm to find the nuclei boundary with the minimum cost within a bounded space around the darkest point in the image. Plissiti *et al.* [121] propose an automated method for the detection and boundary determination of cervical cells nuclei. This method uses a marker-based watershed segmentation to find the nuclei boundaries and then eliminates the false-positive regions by using a binary classifier with shape, texture, and intensity features. However, their method might be limited in its ability to handle variations in the appearance of nuclei [122]. Fatichah *et al.* [123] propose a combination of Gram-Schmidt method and cluster validation algorithm based Bayesian for nuclei segmentation on microscopic breast cancer image. Gram-Schmidt is applied to identify the cell nuclei on a microscopic breast cancer image and the cluster validation algorithm based Bayesian method is used for separating the touching nuclei. Prasath *et al.* [124] propose unsupervised method for segmenting cell nuclei from glioma histopathology. This method combining a nuclear staining information obtained from color decomposition with fast variational active contours to obtain unsupervised segmentation of nuclei in histopathological images. Xu *et al.* [125] propose a Voting-based algorithms for segmenting cell nuclei in the skin histopathological images. This method, first extracts the candidate nuclei regions using an

adaptive threshold technique, and then separates ellipse-like isolated nuclei using two ellipticity parameters. Voting algorithm is used to detect the seeds of clustered nuclei. Finally, the marked watershed algorithm is used to segment nuclei regions.

5.1.2 Isolated Cell Segmentation

Most of the methods in the previous section focus on the segmentation of only the nuclei for which there is relatively higher contrast around the boundaries. However, as the cytoplasm features have been shown to be very useful for the identification of abnormal cells, the detection of the cytoplasm regions from isolated cervical cells is also crucial [126]. For example, Wu *et al.* [127] propose a parametric fitting algorithm for segmentation of cervical cells. This method uses a parametric cost function with an elliptical shape assumption in order to detect the boundary of an isolated nucleus in a cervical cell image. Yang-Mao *et al.* [119] propose a semi-automatic method to segment the nucleus and cytoplasm from a cervical smear image. This method is based on a trim-meaning filter and gradient direction enhancing for segmentation of both the nucleus and the cytoplasm.

Tsai *et al.* [128] propose a method using K-means to cluster the cell images into two classes: one for nuclei and the other for cytoplasm. Another study by Li *et al.* [117] use k-means clustering with three classes to identify nucleus, cytoplasm, and background regions. They then apply snake active contour to refine the nucleus and cytoplasm boundaries. Harandi *et al.* [129] propose an automatic algorithm to perform the segmentation of cervical cells. This method involves three steps: the active contour algorithm to detect the cell boundaries, thresholding to determine the nuclei of each cell, and another active contour to identify the corresponding cytoplasm of each nucleus within connected cell groups. Yang-Mao *et al.* [119] propose an edge-enhancement nucleus and cytoplast contour (EENCC) detector to enable cutting the nucleus and cytoplast from a cervical smear cell image. This method applies the gradient vector flow (GVF) [36] to cervical cell segmentation by

estimating the orientation of the GVFs in the pixels near an edge. The detection of nucleus and cytoplasm boundaries are also explored using GVF in a radiating field [117]. Although this method provides promising results, it can analyse only free-lying cells.

Kale *et al.* [116] propose a two-phase approach to cell segmentation in Pap smear test images. The first phase consists of segmenting an image by a non-parametric hierarchical segmentation algorithm that uses spectral and shape information and gradient information. The second phase aims to obtain nucleus regions and cytoplasm areas by classifying the segments resulting from the first phase based on their spectral and shape features. Gencctav *et al.* [130] propose an unsupervised approach for the segmentation and classification of cervical cells. This method involves automatic thresholding to separate the cell regions from the background, a multi-scale hierarchical segmentation algorithm to partition these regions based on homogeneity, and a binary classifier to separate the nuclei from cytoplasm within the cell regions. Zhang *et al.* [131] propose a method based on graphcuts. Their method allows delineation of the boundary of a clump of cells and detection of overlapping nuclei from images of both normal and abnormal cervical cells. Instead of providing accurate segmentation of each overlapping cell, these methods are only capable of detecting and segmenting the whole clump of overlapping cells and their nuclei.

5.1.3 Overlapping Cell Segmentation

Recent approaches focus on the complete segmentation of individual cytoplasms and nuclei of overlapping cells with varying degrees of overlap among them. Beliz el al. [132] propose a methodology based on a locally constrained watershed transform. The results shown in that paper present limited evidence of the efficacy of the proposed technique. In particular, it is not clear the extent of cell overlap their methodology can successfully handle when segmenting cytoplasm and the nuclei

of overlapping cells. Another methodology proposed is from Lu *et al.* [110, 133], who propose a method that utilizes a joint optimization of multi-level set functions constrained by the length and area of each cell and the shape of the cell. The method first detects the cell clumps and all nuclei within those clumps, then it involves several levels set functions for each cell within a clump, which interact with each other using both unary (intra-cell) and pairwise (inter-cell) terms. The unary constraints are based on contour length, edge strength, and cell shape, while the pairwise constraint is computed based on the area of the overlapping regions. Nosrati *et al.* [134] propose a continuous variational segmentation framework using directional derivatives to segment overlapping cervical cells in Pap smear images, incorporating a star-shape-prior with the level set method. However, these shape priors are too simplified to approximate the real shape of the cervical cells, this approach is only applied to the segmentation of objects with a well-defined and consistent appearance, and defining a shape prior for overlapping cells is not a straightforward process.

Although the method presented in Chapter 3 and Chapter 4 provided promising results in segmenting medical images, however, we can not apply them directly to overlapping cells. This is because overlapping cells are characterised by weaker edges. Instead, we explore another way of applying edge-based active contour using a patch-based approach where we let an open counter evolves independently within small patches.

This chapter proposes a framework capable of segmenting the cytoplasm of each individual cell depicted within an image of overlapping cervical cells. The proposed framework uses a patch-based approach where an active contour detects, on a patch-by-path basis, the cytoplasm boundary of each overlapping cell. The proposed framework also uses a supervised classifier to separate cell clumps from the background. Moreover, it uses feature detection algorithm, maximally stable extremal regions (MSER) algorithm [135], to detect the nucleus of each cell in each

clumps. The centriod of each detected nuclei is used to define the major possible region of each cell in the clump. Then, the framework proceeds to allocate the cytoplasm region of each cell. The active contour within the patch deforms under the influence of GVF forces computed based on the local edges depicted in each patch region. This is important to reduce the computational cost and to provide precise features instead of computing this over the whole image domain where small edge features are neglected. The main goal of our framework is to provide fully segmented cells with high-accuracy compared to ground truth and other methods that also segment overlapping cervical cells [110, 136].

The detection and segmentation of overlapping cells are complicated tasks because several layers of cervical cells are present on a glass slide, which means that cells in an upper layer can partially obscure cells lying underneath [137]. This makes the automated detection and segmentation of overlapping cells more complicated. The cytologist, in a manual examination, uses the depth cue that focus provides in order to assist in the interpretation of the overlapping cells. However, the separation of transparent layers from different fields of view (FOVs) is both computationally intense and difficult [138], because overlapping cells are subject to poor contrast and are located at similar focal depths. Therefore, extended depth of field (EDF) methods propose to tackle this issue by producing a single image where all objects are in focus [139]. This approach is more efficient than analyzing a stack of image with overlapping cells. The proposed framework analyses a single EDF image where all objects are in focus.

The proposed framework can be divided into two steps: an initial clump segmentation followed by a detailed segmentation of each individual cell. The first step consists of the following stages: (i) detecting cell clumps using a supervised classifier; (ii) using MSER for nuclei detection; and (iii) estimating the maximum cytoplasm region of each cell. The second stage consists of a segmentation using patch-based parametric active contour based GVF forces [36] as the main force for

curve deformation. GVF, in general, is a static force [36] when it is computed over the image domain. However, in the framework, the GVF computed for each patch which is different from that computes over the whole image, for the same patch region. Results show that the proposed methodology for cytoplasm segmentation leads to more accurate segmentation results compared to the current state-of-art methods [110, 136].

The rest of the chapter is organized as follows. Section 2 details the proposed methodology. Our proposed external force is detailed in Section 3. Experimental results for segmentation of real EDF images are presented in Section 4. Discussions of the segmentation results is presented in Section 5. Finally, the summary is set out in Section 6.

5.2 The Proposed Framework

For each multi-layer overlapping cervical cells volume, an image is obtained by a one-pass EDF algorithm [140]. For each EDF image, the segmentation of overlapping cervical cells is performed in two steps. the first step consisting of the segmentation of clumps, nuclei detection of each clump using the maximally stable extremal regions (MSER) algorithm and identify the maximum region of each within the clump. Second step focuses on the segmentation of cytoplasm for each cell in each clump. A diagram of the proposed framework illustrating the methodology followed by a synthetic image of the overlapping cell is shown in Figure 5.2.

This section presents the algorithm to build the EDF images and then detail the proposed framework for segmenting overlapping cervical cells.

5.2.1 Extended Depth of Field Images

In our proposed method, a one-pass algorithm based on the overcomplete discrete wavelet transform is used to generate the EDF image [140]. Briefly, this algorithm performs a wavelet transform on each image in the focal plane stack to select the

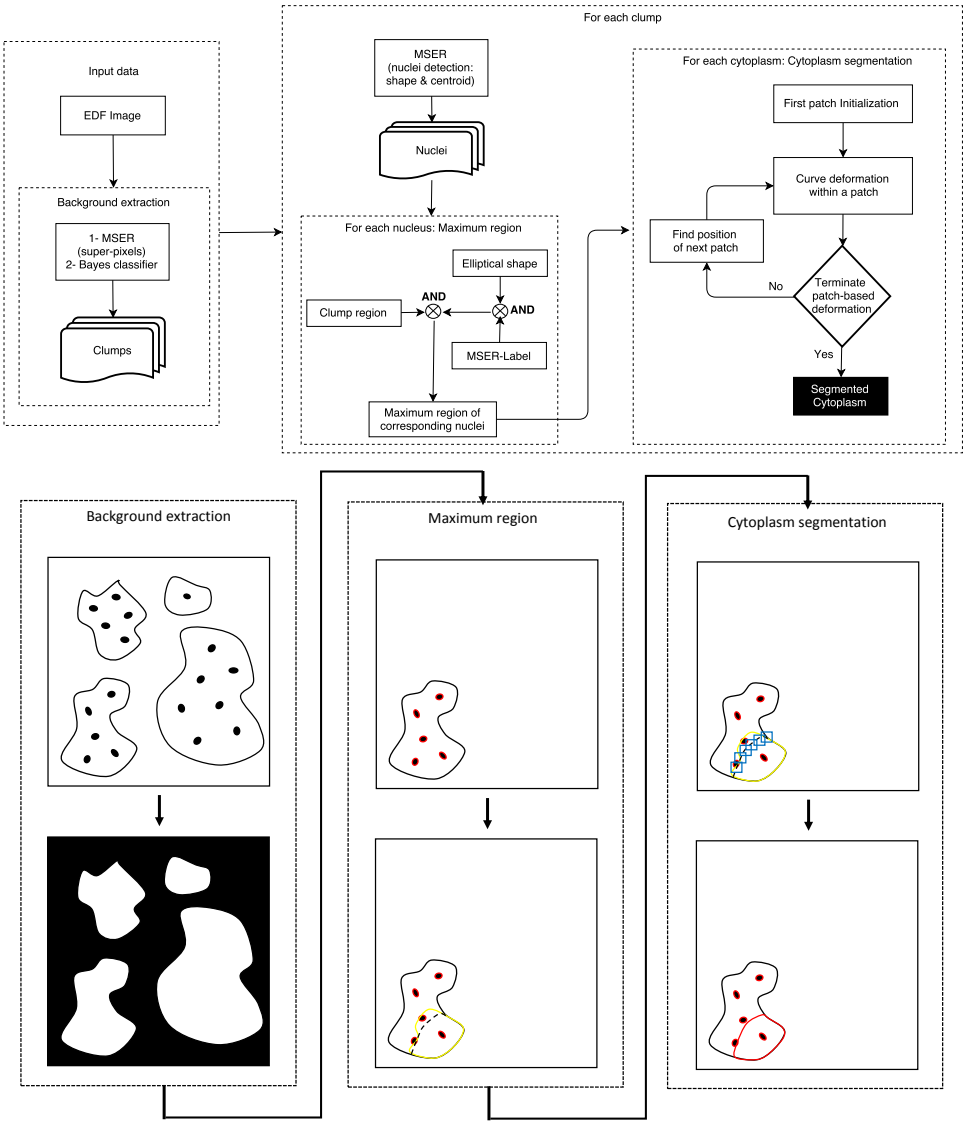

Figure 5.2: The top row is an overview of the proposed methodology. The background extraction step aims to separate the clump regions from the background, then to identify the maximum region of each individual cytoplasm within the clump. The cytoplasm segmentation step aims to segment the cytoplsm of each cell within the clump. The bottom row shows example intermediate outputs of the proposed methodology in a synthetic image depicting overlapping cells.

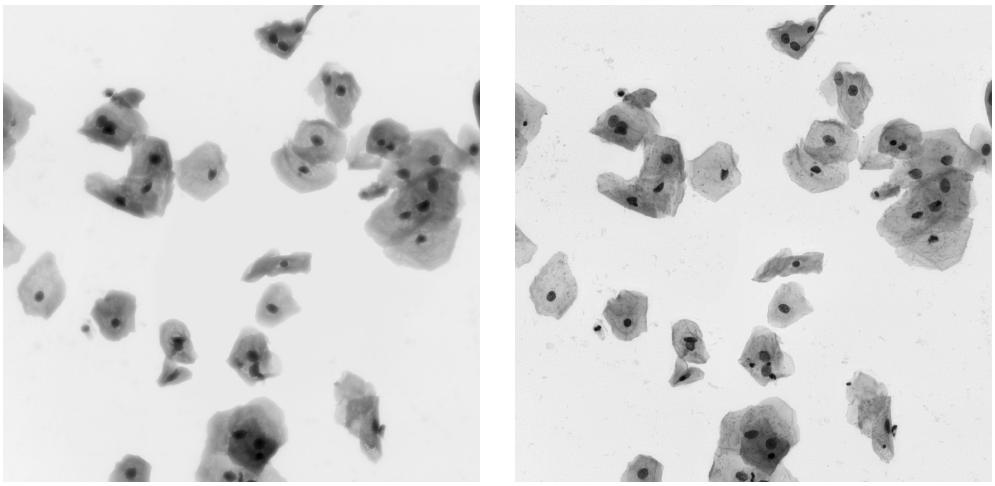

(a) (b)

Figure 5.3: (a) Image generated by MIP. (b) Image generated by EDF.

largest-magnitude wavelet coefficient at each spatial location for each scale. This algorithm uses a simplified contextual constraint based on the maximum coefficient amplitude in a local neighbourhood over all three orientation sub-bands and then implements post-processing to ensure that all output pixel values are on the same scale as those in the original image stack.

It is important to mention that Maximum Intensity Projection (MIP) algorithm can perform the same task to EDF. This algorithm created a single image by the average intensity along the axis of projection at each pixel location. However, the information outside of the focal plane quickly becomes blurred with less defined edges and this blurred region may fail MSER to detect the nuclei. On the other hand, EDF generated a single image with all areas in-focus and with sharper edges. This is illustrated in Figure 5.3.

A pre-processing step is very important for the extraction of the background and the detection of clumps. Pre-processing here helps to reduce the search area in the image. In this step, histogram equalisation is used on EDF image for contrast enhancement and edge sharpening.

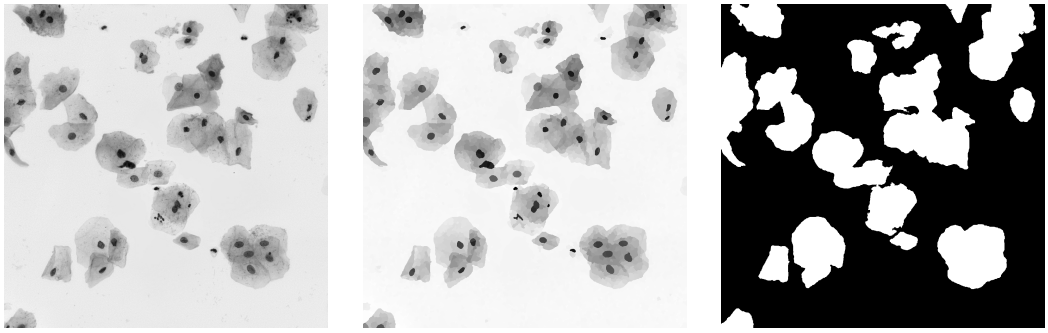

(a) (b) (c)

Figure 5.4: Examples of the original extended depth field (EDF) cervical cytology images: (a) typical cervical cytology image; (b) over-segmented super-pixel map generated by quick shift; (c) binary image representing clump regions.

5.2.2 Background Extraction

The background extraction step aims at dividing an EDF image into cell and background regions, where cell regions correspond to the regions containing cervical cells, or so-called clumps, and background regions correspond to the remaining, empty area. This step reduces the search space for the subsequent stages by concentrating on the regions containing cervical cells.

The clumps including overlapping cells or even isolated cells are detected as follows: on an EDF image a quick shift algorithm [141] is applied to find local maxima of a density function that takes into account gray-value similarities and spatial proximity. The outcome of this step is a map of super-pixels Q_S, which are labelled with gray values in the range [0, 1], representing the respective super-pixel. This is shown in Figure 5.4(b). The second stage consists of running a naive Bayes classifier on this super-pixel map Q_S with two classes, cell clump and background. The connected components in the resulted image with an area smaller than the area of an isolated cell are undesirable and consequently removed. In our images, all areas smaller than 600 pixels are removed. The resulting binary image (see Figure 5.4 (c)) is used as a mask to indicate the clump regions, where each closed region is a clump.

5.2.3 Detection and Segmentation of Nuclei

Detection and segmentation of nuclei is a critical step of our algorithm because each nucleus represents one cell. Nuclei can be characterized by relatively low gray values, homogeneous textures, and well-defined, almost circular borders. Based on the assumption that the nuclei do not overlap the MSER algorithm [135] is used. The MSER algorithm uses pixel gray values and proximity to detect stably connected components. These components are characterized by blobs that represent the candidate nuclei. Some of these candidates are filtered out if the features of the blob detected are larger than a selected threshold. For example, these features can be the size of the blob or mean intensity of the blob. In the experiment, the size of the blob is within the range $\in [200, 600]$ pixels, as the majority of nucleus sizes are located in this range.

5.2.4 Cell Segmentation

Based on our observations, the majority of cytoplasm contours are located on pixels at the same relative distance from their associated nuclei. To segment a cell, the maximum possible region of each cytoplasm in the clump is found based on the orientation of the corresponding nucleus, as observed that the orientation of the nucleus is a good estimator of the orientation of its cytoplasm. Therefore, the geometry of the detected nuclei is used to build an ellipse that represents the majority of the cell (i.e., the maximum region of the corresponding cytoplasm). To find the best ellipse, the contour of the detected nuclei is used as an initial ellipse and then we set the length of its major axis to the nearest nucleus to the cell that we intend to be segmented. The minor axis of the ellipse is then adjusted to ensure that the orientation of the ellipse matches the orientation of the nuclei.

The maximum region of each cell is then given by

$$CM = Q_L \in (Q_L \cap E_{ellipse}) \tag{5.1}$$

where $E_{ellipse}$ is a minimum enclosing ellipse centred in the nucleis centroid c, and Q_L represents regions generated by quick shift. Example of the input image and these regions, which are illustrated in different colours, is shown in Figure 5.5 (a) and (b). Each region in Q_L is labelled with a unique identifier. The outer border of regions that overlap the region depicted by the ellipse represents the maximum possible region of the cell [see the black contour in Figure 5.5 (b)]. The maximum possible region of each cell in the clump is shown in Figure 5.5 (d).

The overlapping between the clump region and CM represents the maximum region of a cell with respect to its clump region. This is shown in Figure 5.5 (c) in the red contour. This border refers by $Line$ with two end points L_0 and L_1, where one of these points represents possible positions for patch initialization. Figure 5.6 shows this in the blue curve.

5.2.4.1 Patch-based Deformation

An image is assumed to consist of small patches, and each observed pixel of the image is the centre of the patch.

Let P_0 be an initial square patch of size $\tau \times \tau$ centred on L_0 or L_1. This is illustrated in Figure 5.7. Then, inside the initial patch, initiate an open curve $C_{P_0}(s) = [x(s), y(s)], s \in [0, 1]$, that is perpendicular to the line connecting the centroid c of the nucleus and the centroid of the patch [see Figure 5.7(b)]. For each cell, the cytoplasm segmentation can be denoted as follows:

$$Cell = E_{patch}(C_{P_0}) \cup \{E_{patch}(C_{P_1}), E_{patch}(C_{P_2}) \dots E_{patch}(C_{P_M})\} \tag{5.2}$$

where M represents the total number of required patches to segment the cell, and $E_{patch}(C_{P_M})$ is the energy function to be minimized for curve $C_{P_M}(s)$. The patch P_0 has the same specification of P_M. However, P_M is initialized based on the result of the deformable open curve from the previous patch, where the last element from

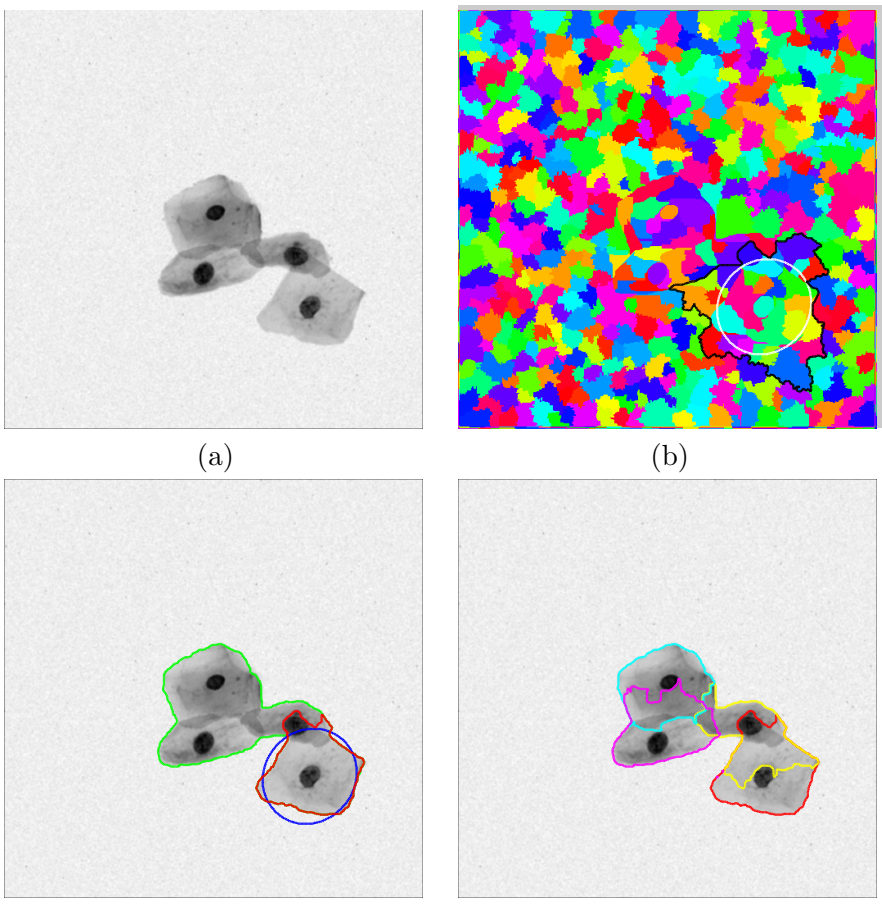

Figure 5.5: (a) Example of a synthetic cervical cytology image with one clump, generated by Lu *et al.* [110]. (b) Corresponding labelled image generated by quick shift; the white curve denotes the elliptical shape $E_{ellipse}$, and the black curve denotes outer border of regions that overlap the region depicted by the ellipse. (c) The result on the cervical image, where the green curve denotes the clump region and the red curve denotes the maximum region of of the cell. (d) The maximum region of each cell in the clump.

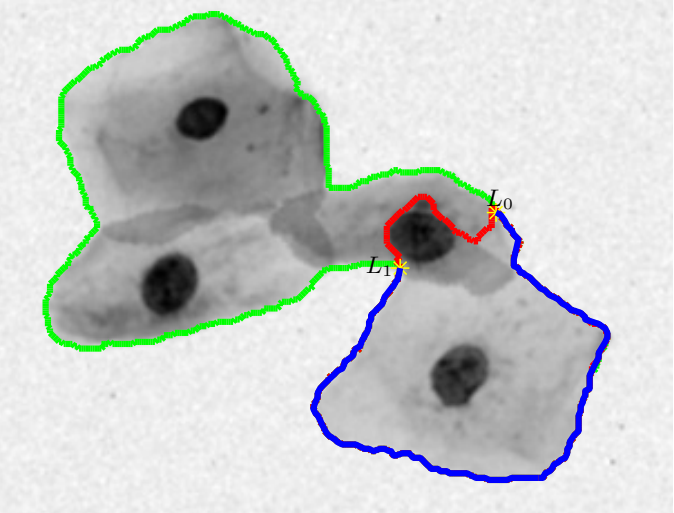

Figure 5.6: Examples of the maximum region of overlapping cell in a clump. The green curve denotes the clump region, the red curve denotes the maximum region of the cell, and blue curve denoted the *Line*. The yellow stars denotes L_0 and L_1, the possible positions for patch initialization.

the curve in the previous patch is the centre of the new patch. It is important to note that the reason for an initial curve perpendicular to c is to provide circular motion of patches around a cell.

The open curve that is initialized in each patch evolves to an object's boundary by minimizing the following energy function:

$$E_{patch}(C_{P_M}) = \frac{1}{2}\int_0^1 (\alpha\left|C'_{P_M}(s)\right|^2 + \beta\left|C''_{P_M}(s)\right|^2)ds + \int_0^1 E_{ext}(C_{P_M}(s))ds \qquad (5.3)$$

where α and β are weighting parameters that control the curve's tension and rigidity, respectively. The first integrand in Equation (5.3) is referred to as the internal energy, which controls the smoothness of C_{P_M}, while the second integrand is referred to as the external energy, which attracts C_{P_M} towards the object's boundary; in this case, to the contour segment of the cytoplasm inside each parch.

The external force in our method consists of the GVF forces [36]. These forces are computed for each patch and change whenever the patch initializes in a different position (i.e. the GVF is computed over the region of each initialized

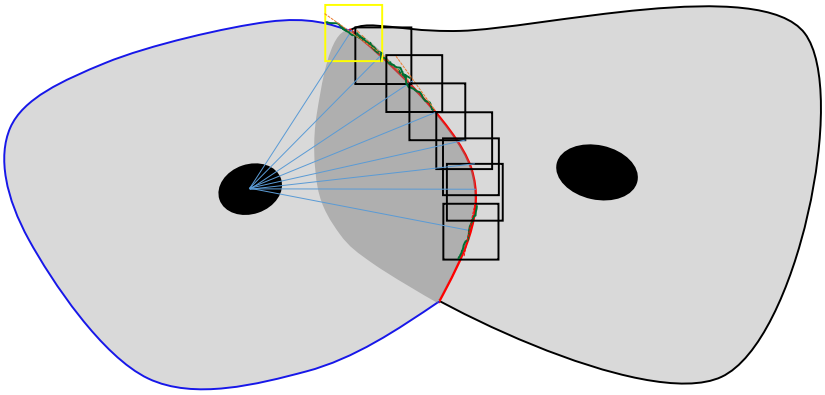

(a)

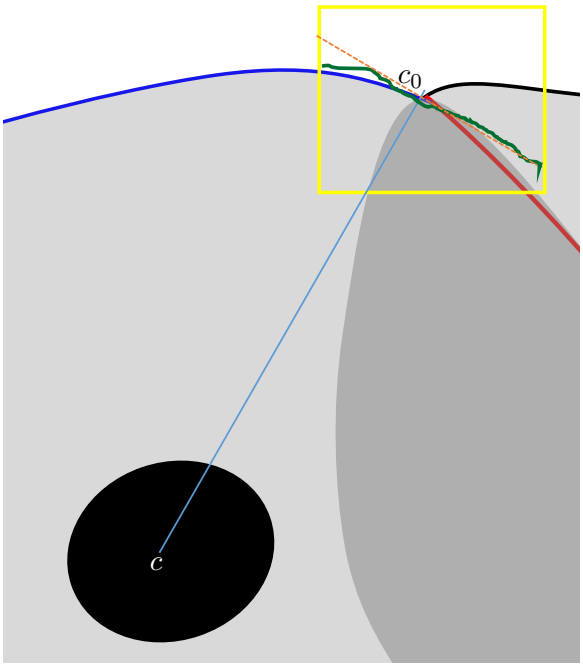

(b)

Figure 5.7: (a) Example synthetic overlapping cells; the red contour denotes overlapping region, the yellow rectangle denotes patch P_0, and the black rectangles denote the following patches. (b) A close-up view of patch P_0; the orange dotted line denotes the initial open curve, which is perpendicular to the light blue line connecting c and c_0; the green contour denotes the result of the deformable curve for this patch.

patch, not over the image domain). Computing GVF over patches provides more accurate gradient which helps the curve to deform smoothly to the desired edges. This also reduces the computational cost, especially with large images.

GVF forces are derived from the diffusion of the gradient vectors of the edge map. Let $\mathbf{v}(x,y) = [u(x,y), \nu(x,y)]$ denote the GVF field, which is set to minimize the following energy function:

$$E_{GVF}(\mathbf{v}) = \iint \mu|\nabla\mathbf{v}|^2 + |\nabla I_{P_M}(x,y)|^2|\mathbf{v} - \nabla I_{P_M}(x,y)|^2 dxdy \tag{5.4}$$

where $I_{P_M}(x,y)$ is the edge map of the patch region. In the proposed method, the Canny edge detector used to compute the edge map. The first term in Equation (5.4) is used to smooth the vector field $\mathbf{v}$, which has the main effect of increasing the capture range of the force field, where μ is a smoothness regularization parameter. The second term is the data fidelity term that makes $\mathbf{v}$ equal to the gradient vector of the edge map ($\nabla I_{P_M}(x,y)$), where ($|\nabla f|$) is relatively large and thus preserves edge information.

The minimization of E_{patch} can be achieved by evolving the curve dynamically as a function of parameter s and artificial time t as follows:

$$C_{P_M}(s,t) = \Big[\alpha C''(s,t) - \beta C''''(s,t)\Big] - \nabla\mathbf{v} \tag{5.5}$$

where the first term and the second term are called the internal force, F_{internal}, and the external force, $F_{external}$, respectively.

5.2.4.2 Termination of Patch-based Deformation

In the proposed methodology, the patch-based deformation is terminated if the angle between the centroid of the new initiated patch L_n and the other end of the *Line* ,L_1 is less than θ_L. This is illustrated in Figure 5.8. To refine the final contour that represents the cell cytoplasm, a live-wire algorithm [142] is applied using the points L_n and L_1. The purpose of this algorithm, in general, is to find the optimal path

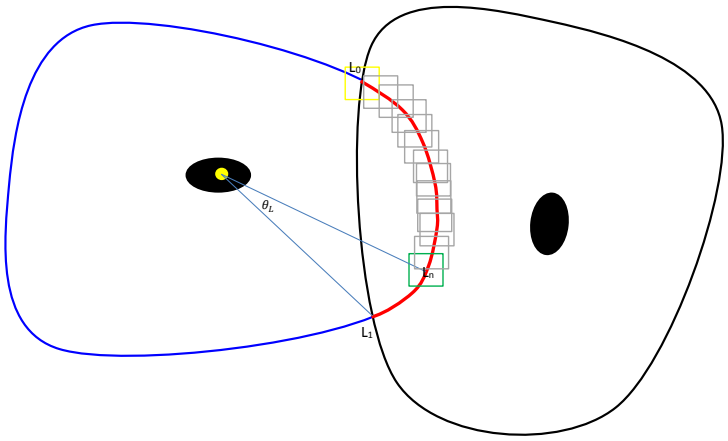

Figure 5.8: Synthetic overlapping cells; the red curve is the detected region of the cell (*Line*), and the yellow rectangle denotes the initialized patch, the gray rectangles denote the deformed patch and the green rectangle denotes the last initialized patch.

between a start node and a set of goal nodes.

The optimal path is defined as the minimum cumulative cost path from a start node to a goal node, where the cumulative cost of a path is the sum of the local costs on the path. The local cost function $L_{cost}(L_n, L_1)$ from the last pixel L_n to pixel L_1 is defined as:

$$L_{cost}(L_n, L_1) = w_C f_C(L_1) + w_M f_M(L_1) + w_D f_D(L_n, L_1) \tag{5.6}$$

where the cost terms for the local 2D live-wire f_C,f_M, and f_D are gradient magnitude, gradient direction, and Canny edge detection, respectively. w_C, w_M, and w_D are weight constants that allow each cost term to contribute to the cost function at different rates. The gradient magnitude cost term for any point L_1 is defined as

$$f_M(L_1) = 1 - \sqrt{\frac{dL_1{}^2}{dx} + \frac{dL_1{}^2}{dx}} \Big/ \max(G) \tag{5.7}$$

where $max(G)$ represents the largest gradient magnitude in the 2D image. The live-wire algorithm searches the minimum cost path between two points of an image, so the gradient magnitude must be inverted such that strong edges correspond to low

costs. The gradient direction cost term point L_n towards point L_1 is defined as

$$f_D(L_n, L_1) = acos\left(\frac{dL_n/dx}{G(L_n)} \times \frac{dL_1/dx}{G(L_1)} + \frac{dL_n/dy}{G(L_n)} \times \frac{dL_1/dy}{G(L_1)}\right)/\pi \tag{5.8}$$

where $G(L_n)$ represents the gradient magnitude for point L_n. The pixels that define the path of the minimum cost are then added to the $Cell$ contour.

5.3 Materials and Experimental Setup

The dataset in this chapter was obtained from [110], contains 8 EDF images, each image has up to 15 clumps and each clump contains varying number of cells with an overlap coefficient in the range $\in [0, 0.9]$, 0 indicate no overlap while 0.9 indicates 90% overlapping. The images in the dataset are in gray level. The specimens were prepared using the AutoCyte PREP technology [143], and so each specimen is around $20\mu m$ thick in the focal-dimension. Images were acquired on an Olympus BX40 microscope with an 40x objective and a four-mega-pixel SPOT Insight camera, with square pixels of a size of $7.4\mu m$ and a 100% fill factor. This gives an image resolution of around $0.185\mu m$ per pixel. The 40x objective has a numerical aperture of 0.75, which gives a depth of field of approximately $1\mu m$. Therefore, for each FOV, a stack of at least twenty focal plane images with a focal depth separation of $1\mu m$ were acquired.

The edge map is computed as described using Canny edge indicator, $\alpha = 0$ and $\beta = 10$ used to control the smoothness of the curve, and a value of $\mu = 0.2$ for the regularization parameter to compute the GVF field, as suggested in [36]. The size of the patch is set to $\tau = 10$. Note that, the curve deforms within each patch for 10 iterations and $\theta_L = 20$ is used to terminate patch-based deformation.

The performance of the proposed framework is compared with state-of-the-art methods available from the literature. To the best of our knowledge, the methods presented in [110,136] provide the best performances proposed in the field of segmen-

tation of overlapping cervical cells. Note that the values of parameters for Nosrati's method and Lu's method selected were as suggested in [110, 136]. A summary of these approaches is as follows:

1. Nosrati *et al.* [136] propose a method for nuclei detection and cytoplasm segmentation. For their method, nuclei detection is based on the union of the output of MSER and a random decision forest with a star-shaped prior. Each cytoplasm and its corresponding nucleus are represented as two signed distance maps. The energy function is optimized with respect to cytoplasm and nuclei level-set functions, where this energy function is given by:

$$E(\phi^c, \phi^n) = \lambda_1 E_R(\phi^c, \phi^n) + \lambda_2 E_D(\phi^c, \phi^n) + \lambda_3 E_S(\phi^c) + \lambda_4 E_O(\phi^c, \phi^n) + R(\phi) \tag{5.9}$$

   where ϕ^c and ϕ^n are two level set functions that represent cytoplasm and its corresponding nucleus, respectively. E_R is the regional term, E_D is the distance prior between the cytoplasm boundary and its corresponding nucleus, E_S is the elliptical shape prior, E_O is an overlap constraint that motivates neighbouring cytoplasms to be excluded from one another, and R is the regularization term that ensures a smooth boundary of the segmented cells. λ_1 to λ_4 are positive weights balancing the contribution of each term in (5.9).

   The regional term uses a trained random forest classifier to measure the agreement of an image pixel with background, cytoplasm, and nucleus. The distance prior term ensures that the nucleus is contained within the corresponding cytoplasm. The E_O term limits the overlapping between two neighbouring cytoplasms, and the regularisation term maintains the desired shape and ensures smooth boundaries.

2. Lu *et al.* [110] propose a joint optimization of multiple level set functions,

where each function represents a cell within a clump. The energy function to be minimized is defined as

$$E_{Lu}(\phi) = \sum_{i=1}^{N} E_u(\phi_i) + \sum_{i=1}^{N} \sum_{j \in N(i)} E_b(\phi_i, \phi_j) \tag{5.10}$$

where E_u denotes the unary energy function defined for each level set function (LSF) independently, E_b represents the binary function defined over pairs of LSFs, and $N(i)$ represents the level set functions ϕ_j such that their zero-level set intersects the zero-level set of ϕ_i.

This method can be summarised as follows: (i) For a given cervical cytology image quick-shift algorithm is used to compute the super-pixels map. (ii) Running an edge detector on this super-pixel map gives a clear edge map. (iii) A convex hull represents the clumps, which is built by running a connected component analysis on the edge map. (iv) An unsupervised classifier classifies the image into two region,clumps and background regions. (v) MSER detects the nucleus in each clump. vi) A level set function for each cell in clump is used to find the cell boundary.

5.4 Experimental Results

5.4.1 Quantitative Assessment

Nuclei Detection: As the proposed framework uses the previously proposed MSER algorithm to detect the nuclei and does not focus on nucleus detection, therefore, there is no comparison presented in this regard. Figure 5.9 shows an example of detected nuclei using an MSER algorithm.

Cytoplasm Segmentation: The quantitative evaluation is based on the performance of the proposed framework in terms of detection and segmentation accuracy on EDF images with the total of 200 cells with overlap coefficient $\in [0, 0.9]$. The quantitative performance of individual cell cytoplasm segmentation is assessed

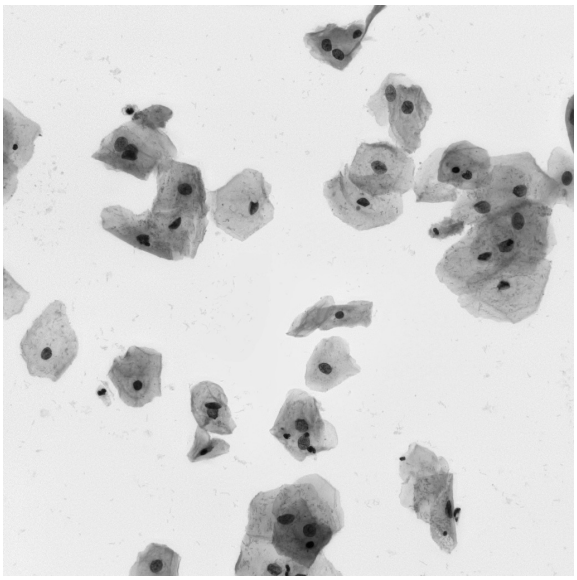

(a)

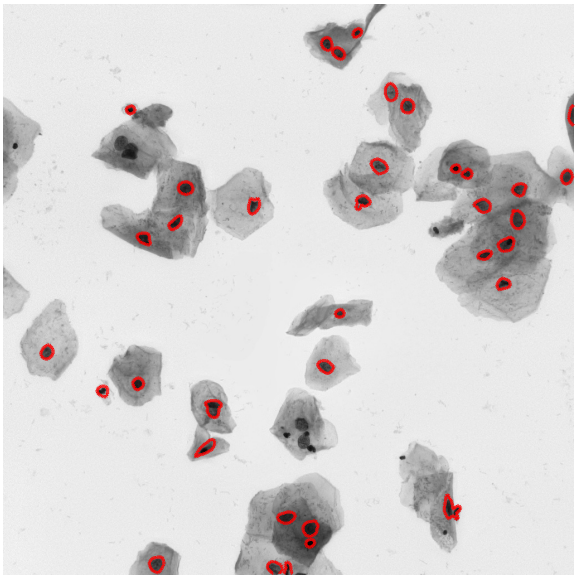

(b)

Figure 5.9: Examples of the original extended depth field (EDF) cervical cytology images: (a) typical cervical cytology image; (b) nuclei detected by MSER.

using the average dice coefficient (DSC) [see Equation 3.17 in chapter 3]. The DSC values above 0.7 are considered to be "good" cell segmentation [144].

Table 5.1 tabulates the quantitative comparison with the other two methods, using the DSC values and also tabulates the pixel-based evaluation using the true-positive (TP) rates. The false-negative (FN) rates and false-positive (FP) rates of this comparison are tabulated in Table 5.2.

Table 5.1: Cytoplasm segmentation evaluation. The highlighted value represents the best results, and the values in parentheses represent the standard deviation.

Method	Dice (Pixel)	Tp (Pixel)
Nosrati *et al.*	0.8600(0.0776)	0.8642(0.1023)
Lu *et al.*	0.8371(0.0818)	0.8702(0.1221)
Proposed	**0.9140(0.0632)**	**0.9239(0.0711)**

Table 5.2: The false positives (FP) and false negative (FN) of the segmentation evaluation. The highlighted value represents the best results, and the values in parentheses represent the standard deviation.

Method	Fp (Pixel)	Fn (Pixel)
Nosrati *et al.*	0.0011(0.0012)	0.1357(0.1023)
Lu *et al.*	0.0019(0.0016)	0.1297(0.1221)
Proposed	**0.0008(0.0009)**	**0.0760(0.0711)**

5.4.2 Qualitative Assessment

Examples of the complete segmentation results for Lu *et al.* method, Nosrati et al method, and the proposed method on real EDF images are shown in Figure 5.10 which shows not only the results obtained by these methods, but also the ground truth. Visual results from the algorithm proposed by Lu *et al.* show more detected cells in comparison to the other approaches. This is mainly due to the good nuclei-detection algorithm, which allows more cells to be analysed. However, this method fails to segment cells with a high degree of overlap with other cells. The method proposed by Nosrati *et al.* has advantages in the overlapping regions,

regardless of the degree of overlap between cells. However, in terms of accuracy, this method is less precise in distinguishing the cells from the background because of the inaccurate random decision forest probability map used [110]. The results of the proposed method verify the quantitative results presented in Table 5.1 and Table 5.2, where the proposed framework provides high DSC values of segmenting overlapping cells.

Ground-truth

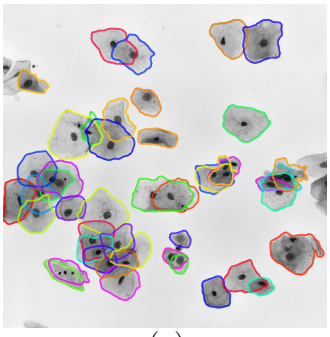

(a)

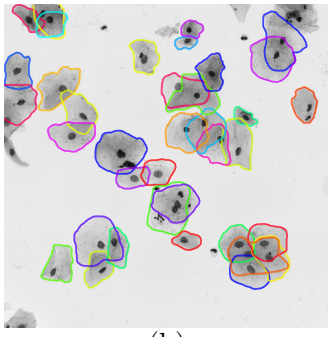

(b)

Lu *et al.*

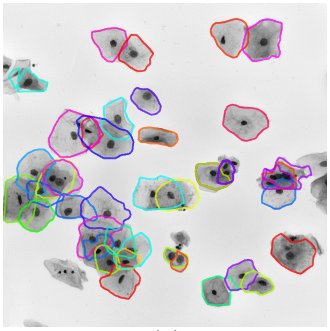

(c)

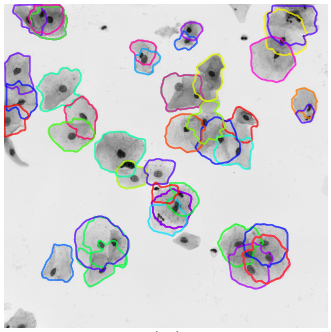

(d)

Nosrati *et al.*

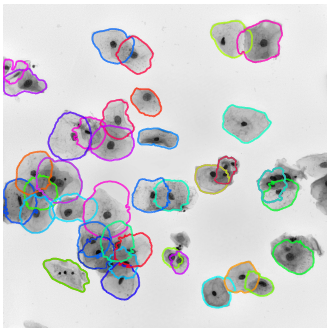

(e)

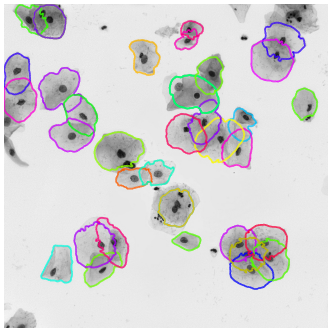

(f)

Proposed Framework

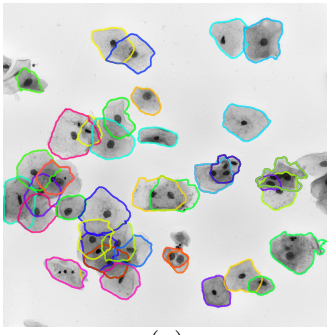

(g)

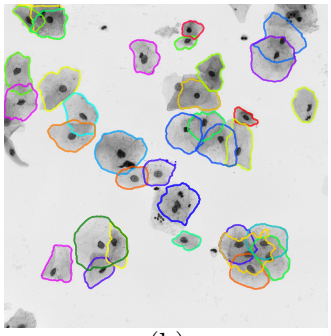

(h)

Figure 5.10: EDF Cervical Cytology Images. In the first row the curves denotes the ground-truth and from the secound row to the end the curves denotes the results obtain from each method.

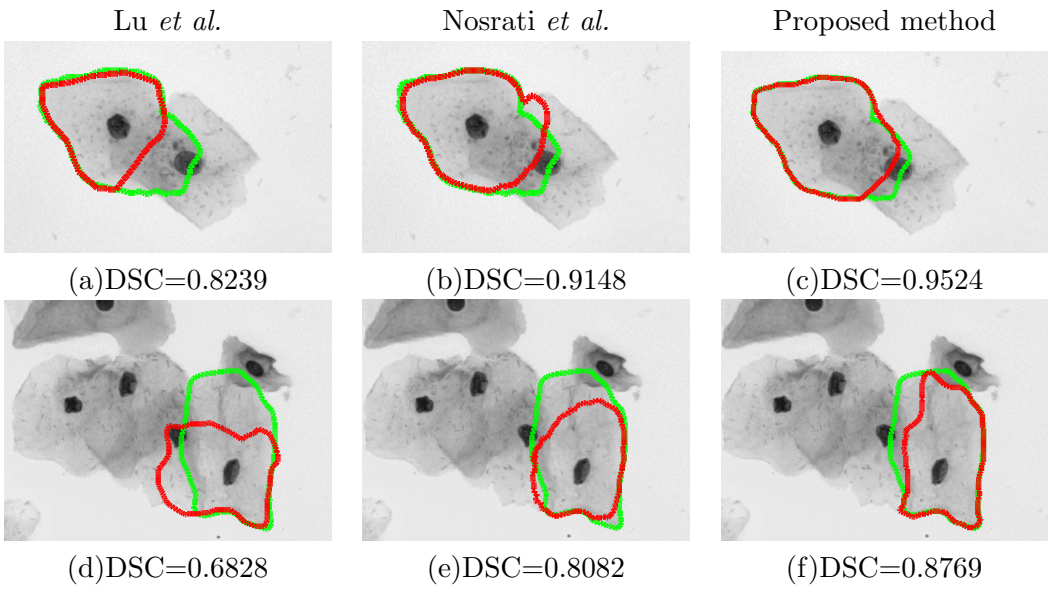

Figure 5.11: Two example of EDF cervical cytology image. Each row represents a case with a comparison between the proposed method and the state-of-art method. The green contour denotes the ground truth, while the red contour denotes the results obtained by a different method.

5.5 Discussion

This chapter presented a quantitative and qualitative assessment of a selection of state-of-the-art methods. The framework proposed in this chapter produces robust results to the problem of segmenting cytoplasm from overlapping cervical cells. The methodology proposed by Lu *et al.* has a better nuclei-detection approach, which gives their method an advantage in segmenting more cytoplasm than Nosrati *et al.* or our proposed method. It is worth mentioning that the quantitative and qualitative comparison based on the visual appearance of the cytoplasm segmentation in the peoposed framework and both approaches proposed by Lu *et al.* and Nosrati *et al.* shows that these methods produce relatively realistic results.

In some cases where the cell is in more of an oval shape than a circular shape, the method proposed by Lu *et al.* fails to accurately segment the cell. For instance, in clumps where there are two cells [see Figure 5.11 (a)] Equation (5.10) enforces the contour to be minimized in the overlapping area between the two cells. The

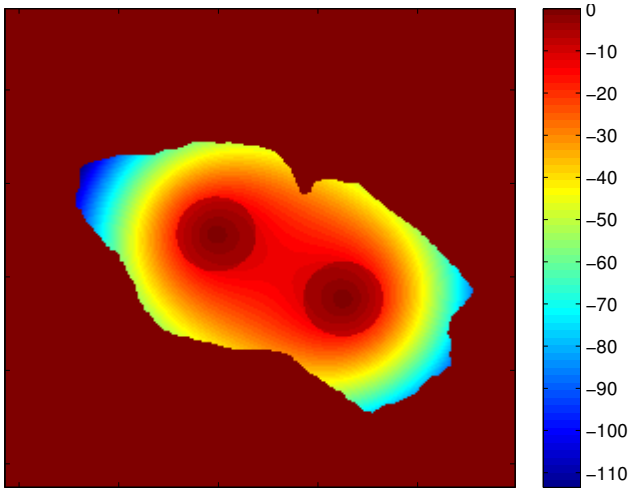

Figure 5.12: A distance map of a clump with two cells.

distance map of the clump with two cells shown in Figure 5.12 illustrates that the overlapping area has a small distance to each nucleus. The area representing the small distance makes the curve deformation very slow, where the deformation speed decreases in area near to the nuclei and overlapping regions. While the method proposed by Nosrati *et al.* provides better result [see Figure 5.11 (b)], this is mainly due to the elliptical-shape prior in term E_s in Equation (5.9). However, the proposed framework shows a better result regarding accuracy compared with the other methods. This is because the patch-based approach provides advantages over the other methods. One of these advantages is that the first patch is always initialized on the edge of the cytoplasm and the following patches are initialized inside a maximum region of the cell to ensure segmenting the corresponding cell. Another advantage is the circular motion of the initialized patches; this makes contour that represents the cytoplasm in a realistic modelling of cell shapes.

The method proposed by Lu *et al.* also fails in other cases where the cell nucleus is not exactly centred in the cell. This is mainly due to the binary function represented by term E_b, where this term defines over pairs of nuclei, usually with the nearest one. This makes the contour limited with the distance of the nearest nucleus especially if the clump has more that two cells [see Figure 5.11 (d)]. While

Nosrati *et al.*'s method again shows better visual results [see Figure 5.11 (e)], the use of the shape prior enforces the contour to be in a circular shape. Because the proposed framework does not rely on a particular shape, it provides better results in both; visual and accuracy value [see Figure 5.11 (f)].

There are certain limitations worth mentioning, such as segmenting cells with large overlap between cells, i.e., where the overlap degree is more than 60%. Another issue is the FN detection of nuclei, where most of the nuclei that were not detected have a blur transition to the cytoplasm or are represented by a light black spot, which means the MSER algorithm fails to detect them. Furthermore, finding the maximum region may fail, especially when the orientation of the nuclei is contrary to the orientation of the corresponding cell. Thus, it is likely that the effectiveness of the proposed method will be severely compromised. Therefore, further work should be done to overcome these limitations. For instance, using the method proposed by Lu *et al.* for nuclei detection instead of MSER to detect more cells. Also, using region growing algorithm could be possible solution to find the maximum region of the cell by starting from small regions around the nucleus.

5.6 Summary

This chapter presented a framework that addresses the problem of segmenting the nucleus and cytoplasm of each individual cell in EDF images depicting overlapping cervical cells. The proposed framework uses a patch-based approach where an active contour detects the cytoplasm boundary of each overlapping cell. The active contour within the patch is deformed under the influence of GVF forces computed based on local edge features collected from the patch region. This force is computed over each each initialized patch to reduce the computational cost and to provides precise features instead of computing this over the whole image domain where small edge features are neglected. The proposed framework also uses a supervised classifier and feature detection algorithm to detect the clumps and the cells nuclei in each clump.

5.6 Summary

The centriod of each detected nucleus is used to define the major possible region of each cell in the clump. Experimental results showed that the proposed framework outperforms other state-of-the-art approaches, in terms of segmentation accuracy. The major advantage of our proposed method is that it is fully automated and is suitable for images with up to 50% degree of cell overlap.

Chapter 6

Conclusions and Future Work

6.1 Conclusions

Although image segmentation is a fundamental problem in image analysis, it has been difficult for traditional image segmentation methods to produce satisfying results on medical images due to several factors that affect the image segmentation process such as: texture, image inhomogeneities, image content, high level of noise and weak edges. Due to these factors, image segmentation remains a major concern in the computer vision and image processing fields.

This thesis presented three different contributions, which produce robust image segmentation results on difficult image segmentation problems. The image segmentation methods in this thesis used a framework of active contour models (snakes and level sets). This chapter summaries the contributions of the thesis and proposes future work.

Chapter 3 proposed a novel external force for parametric snakes that combines balloon and GVF forces. The external force uses a weighting factor to leverage the advantages of these two forces according to local image features. In smooth

areas with little edge information, balloon forces guide the snake to the objects boundary, while in the presence of strong edge information GVF forces make the snake conform to the boundary. The proposed approach is compared to snakes using GVF forces, balloon forces and a combination of GVF and balloon forces based on manual thresholding. The proposed method allows the snake to deform under following conditions:

1. If the snake is located in a smooth region, balloon forces are the main acting external forces driving the snake close to the object's boundary (i.e. the direction of the GVF field is similar or opposite to the normal direction of growth of the snake).

2. If the snake is located in a non-smooth region and its normal direction of growth does not coincide with the local average direction of the GVF field. GVF forces tend to be the main acting external forces, helping the snake conform to the object's boundary.

The proposed method was evaluated for segmentation of various regions in real MRI and CT slices images. Experimental results show that the proposed external force outperforms the other evaluated external forces, and minimizes snake leakages, while offering the advantage of initializing the snake with a single manually selected point inside the desired region.

Chapter 4 proposed a novel medical image segmentation method based on a level set active contour model that provides improved boundary detection accuracy around weak edges in medical images. The method uses a weighting factor to leverage the advantages of incorporating local edge features into the objective energy functional. Specifically, the method combines edge intensity information with edge directional information collected from the adjacent region located inside and outside

of the evolving contour. This information is then used to determine the importance of various energy terms in an energy functional. As a consequence, the proposed method is able to accurately drive the contour to the desired boundary even around weak edges, thus minimizing leakages in medical images. The novelties about how local edge information is used in the proposed method are as follows:

1. The proposed method measures the average alignment between the normal direction of the evolving contour and the image's gradient in the adjacent region located inside and outside of the evolving contour. Other methods that also measure this alignment usually do this only in the region adjacent to the evolving contour in the direction of movement. Moreover, this measurement is often used as an additional energy term in the energy functional.

2. The proposed method also considers the average edge intensity in the adjacent region located inside and outside of the evolving contour. This allows us to minimize the negative effect of weak edges on the segmentation accuracy.

3. The proposed method uses the collected local information to compute a single value that serves as a weight to control the influence of two main forces. This minimizes leakage in areas where weak edges exist. If the desired object is delimited by both weak and strong edges, this weight helps minimize the influence on weak edges if sufficient strong edges exist. As a consequence, the evolving contour tends to converge to the desired boundary even in areas where weak edges exit.

The performance of the proposed method was demonstrated on various regions in real MRI and CT slices, as well as Xray images and was compared with the performance of various edge-based and region-based methods. Experimental results showed that the proposed method outperforms other state-of-the-art edge-based

level-set approaches, in terms of segmentation accuracy, and is capable to converge to the desired boundary in less iterations

Chapter 5 presented a framework that addresses the problem of segmenting the cytoplasm of each individual cell in EDF images depicting overlapping cervical cells. The proposed framework uses a patch-based approach where parametric active contour detects the cytoplasm boundary of each overlapping cell. The active contour within the patch is deformed under the influence of GVF forces computed based on the local edges depicted in each patch region. The propose framework can be divided into two steps:

1. The first step consists of the following stages: (i) detecting cell clumps using a supervised classifier; (ii) using MSER for nuclei detection; and (iii) estimating the maximum cytoplasm region of each cell.

2. The second stage consists of an initial segmentation using patch-based parametric active contour using GVF force [36] as the main external force for curve deformation. GVF, in general, is a static force [36] when it is computed over the image domain. However, in the framework, this force is computed over each patch in order to reduce the computational cost and to provides precise local edge information, instead of computing this over the whole image domain where small edge features may be neglected.

The proposed framework also uses a supervised classifier and feature detection algorithm to detect the clumps and the cells nuclei in each clump. The centroid of each detected nucleus is used to define the major possible region of each cell in the clump. Experimental results showed that the proposed framework outperforms other state-of-the-art approaches, in terms of segmentation accuracy. The major advantage of our proposed method is that it is fully automated and is suitable for

images with up to 50% degree of cell overlap.

6.2 Future Work

Although this thesis has proposed a number of approaches for addressing some challenges in edge-based active contours, more work is yet to be done in order to bring the performance of active contours models to a higher level. Some future research is listed as follows:

- One of the important directions for future work is to extend the methods in Chapter 3 and Chapter 4 which are limited to 2D to operates on 3D images directly, such that a surface is evolved instead of curves on individual slices or placing a series of contours in each 2D slices of the volumetric image. The deformation of the contours may then be controlled through a set of contours and external forces that are placed in the Z dimension.

- The approaches proposed in this thesis are limited to edge-based information. Incorporating different information such as boundary or region of different nature (i.e. texture, motion) could be a possible extension to the existing framework that can increase robustness.

- It would be interesting to investigate the possibility of adopting the weight factor proposed in Chapter 3 and Chapter 4 into active appearance models and active shape models.

- In the proposed framework in Chapter 5, the ellipse shape, which is used to fined the maximum possible region of the cell, have to be in the same orientation of the nucleus to provide the appropriate maximum region. However, if

the orientation of the nucleus is contrary to the orientation of the corresponding cell, the maximum possible region may not include all regions belonging to the corresponding cell, and this will provide false segmentation. This problem can be addressed by applying Voronoi diagram. This diagram can partition the image into regions based on a distance to points in a specific subset of the image. In the cell case, the distance will be counted from the detected nuclei to the ellipse. It will be very interesting to investigate the resulting regions.

Also, in the proposed framework, the parametric active contour used to deform to the cell boundary within the patch. However, as mentioned in Chapter 2, the level set has more advantages over snakes. Therefore, implementing level set in each patch can be a possible extension for this work.

- As the majority of current active contours are in general slow, investigation of a fast implicit contour is needed. Further studies must focus on the development of the proposed methods to achieve better computation and performance. This can be done by combining the deep learning algorithms with proposed methods. Also, as the manual tuning of parameters severely limits the usage of active contour models, deep learning can be use to estimate the parameters avoid manual tuning and hence optimize segmentation results.

References

[1] R. C. Gonzalez and R. E. Woods, "Digital image processing," *Prentice Hall*, 2008.

[2] Y. Y. Boykov and M.-P. Jolly, "Interactive graph cuts for optimal boundary & region segmentation of objects in nd images," in *Computer Vision, 2001. ICCV 2001. Proceedings. Eighth IEEE International Conference on*, vol. 1. IEEE, 2001, pp. 105–112.

[3] Y. Boykov, O. Veksler, and R. Zabih, "Markov random fields with efficient approximations," in *Computer vision and pattern recognition, 1998. Proceedings. 1998 IEEE computer society conference on.* IEEE, 1998, pp. 648–655.

[4] R. A. Brooks, R. Creiner, and T. O. Binford, "The acronym model-based vision system," in *Proceedings of the 6th international joint conference on Artificial intelligence-Volume 1.* Morgan Kaufmann Publishers Inc., 1979, pp. 105–113.

[5] G. J. Brostow, J. Shotton, J. Fauqueur, and R. Cipolla, "Segmentation and recognition using structure from motion point clouds," in *European conference on computer vision.* Springer, 2008, pp. 44–57.

[6] D. Gabor, "Theory of communication. part 1: The analysis of information," *Electrical Engineers-Part III: Radio and Communication Engineering, Journal of the Institution of*, vol. 93, no. 26, pp. 429–441, 1946.

[7] M. Kass, A. Witkin, and D. Terzopoulos, "Snakes: Active contour models," *International Journal of Computer Vision*, vol. 1, no. 4, pp. 321–331, 1988.

[8] R. Brunelli, *Front Matter Template Matching Techniques in Computer Vision: Theory and Practice*. Wiley Online Library, 2009.

[9] R. O. Duda and P. E. Hart, "Pattern classification and scene analysis," *J. Wiley and Sons*, 1973.

[10] N. Otsu, "A threshold selection method from gray-level histograms," *Automatica*, vol. 11, no. 285-296, pp. 23–27, 1975.

[11] X. Chen, Q. Huang, P. Hu, M. Li, Y. Tian, and C. Li, "Rapid and precise object detection based on color histograms and adaptive bandwidth mean shift," in *2009 IEEE/RSJ International Conference on Intelligent Robots and Systems*. IEEE, 2009, pp. 4281–4286.

[12] S. Hojjatoleslami and J. Kittler, "Region growing: a new approach," *IEEE Transactions on Image processing*, vol. 7, no. 7, pp. 1079–1084, 1998.

[13] Y. Boykov, O. Veksler, and R. Zabih, "Fast approximate energy minimization via graph cuts," *IEEE Transactions on Pattern Analysis and Machine Intelligence*, vol. 23, no. 11, pp. 1222–1239, 2001.

[14] C. Rother, V. Kolmogorov, and A. Blake, "Grabcut: Interactive foreground extraction using iterated graph cuts," in *ACM transactions on graphics (TOG)*, vol. 23, no. 3. ACM, 2004, pp. 309–314.

[15] J. Carreira and C. Sminchisescu, "Constrained parametric min-cuts for automatic object segmentation," in *Computer Vision and Pattern Recognition (CVPR), 2010 IEEE Conference on.* IEEE, 2010, pp. 3241–3248.

[16] L. Ladicky, C. Russell, P. Kohli, and P. H. Torr, "Graph cut based inference with co-occurrence statistics," in *European Conference on Computer Vision.* Springer, 2010, pp. 239–253.

[17] O. Oreifej, R. Mehran, and M. Shah, "Human identity recognition in aerial images," in *Computer Vision and Pattern Recognition (CVPR), 2010 IEEE Conference on.* IEEE, 2010, pp. 709–716.

[18] Y. Guo, S. Hsu, H. S. Sawhney, R. Kumar, and Y. Shan, "Robust object matching for persistent tracking with heterogeneous features," *IEEE transactions on pattern analysis and machine intelligence*, vol. 29, no. 5, pp. 824–839, 2007.

[19] Y. Bai, N. Walsworth, B. Roddan, D. Hill, K. Broersma, and D. Thompson, "Quantifying tree cover in the forest–grassland ecotone of british columbia using crown delineation and pattern detection," *Forest Ecology and Management*, vol. 212, no. 1, pp. 92–100, 2005.

[20] R. Lucas, P. Bunting, M. Paterson, and L. Chisholm, "Classification of australian forest communities using aerial photography, casi and hymap data," *Remote Sensing of Environment*, vol. 112, no. 5, pp. 2088–2103, 2008.

[21] D. Hoiem, A. A. Efros, and M. Hebert, "Recovering surface layout from an image," *International Journal of Computer Vision*, vol. 75, no. 1, pp. 151–172, 2007.

[22] X. He, R. S. Zemel, and M. Á. Carreira-Perpiñán, "Multiscale conditional random fields for image labeling," in *Computer vision and pattern recognition,*

2004. CVPR 2004. Proceedings of the 2004 IEEE computer society conference on, vol. 2. IEEE, 2004, pp. II–695.

[23] J. Shotton, J. Winn, C. Rother, and A. Criminisi, "Textonboost: Joint appearance, shape and context modeling for multi-class object recognition and segmentation," in *European conference on computer vision*. Springer, 2006, pp. 1–15.

[24] V. Kolmogorov, "Convergent tree-reweighted message passing for energy minimization," *IEEE transactions on pattern analysis and machine intelligence*, vol. 28, no. 10, pp. 1568–1583, 2006.

[25] C. Russell, P. Kohli, P. H. Torr, *et al.*, "Associative hierarchical crfs for object class image segmentation," in *2009 IEEE 12th International Conference on Computer Vision*. IEEE, 2009, pp. 739–746.

[26] K. McGuinness and N. E. Oconnor, "A comparative evaluation of interactive segmentation algorithms," *Pattern Recognition*, vol. 43, no. 2, pp. 434–444, 2010.

[27] R. Adams and L. Bischof, "Seeded region growing," *IEEE Transactions on pattern analysis and machine intelligence*, vol. 16, no. 6, pp. 641–647, 1994.

[28] S. Beucher and C. Lantuéjoul, "Use of watersheds in contour detection," 1979.

[29] J. B. Roerdink and A. Meijster, "The watershed transform: Definitions, algorithms and parallelization strategies," *Fundamenta informaticae*, vol. 41, no. 1, 2, pp. 187–228, 2000.

[30] G. B. Ederra, "Mathematical morphology techniques applied to anti-personnel mine detection," Ph.D. dissertation, MS Thesis, Department of Electronics and Information Processing, Vrije Universiteit Brussel, 1999.

[31] F. Meyer, "An overview of morphological segmentation," *International journal of pattern recognition and artificial intelligence*, vol. 15, no. 07, pp. 1089–1118, 2001.

[32] S. Beucher *et al.*, "The watershed transformation applied to image segmentation," *SCANNING MICROSCOPY-SUPPLEMENT-*, pp. 299–299, 1992.

[33] H. Digabel and C. LANTUEJOUL, "Iterative algorithms, special issues of practical metallography, vol. 8," pp. 85–99, 1977.

[34] D. Jayadevappa, S. Srinivas Kumar, and D. Murty, "Medical image segmentation algorithms using deformable models: a review," *IETE Technical review*, vol. 28, no. 3, pp. 248–255, 2011.

[35] G. Zhu, S. Zhang, Q. Zeng, and C. Wang, "Gradient vector flow active contours with prior directional information," *Pattern Recognition Letters*, vol. 31, no. 9, pp. 845–856, 2010.

[36] C. Xu and J. L. Prince, "Snakes, shapes, and gradient vector flow," *IEEE Transactions on Image Processing*, vol. 7, no. 3, pp. 359–369, 1998.

[37] L. D. Cohen, "On active contour models and balloons," *CVGIP: Image understanding*, vol. 53, no. 2, pp. 211–218, 1991.

[38] K. Sum and P. Cheung, "Boundary vector field for parametric active contours," *Pattern Recognition*, vol. 40, no. 6, pp. 1635–1645, 2007.

[39] N. Paragios and R. Deriche, "Geodesic active regions: A new framework to deal with frame partition problems in computer vision," *Journal of Visual Communication and Image Representation*, vol. 13, no. 1, pp. 249–268, 2002.

[40] Y. Wu, Y. Wang, and Y. Jia, "Segmentation of the left ventricle in cardiac cine mri using a shape-constrained snake model," *Computer Vision and Image Understanding*, 2013.

[41] M. Zhang, Q. Li, L. Li, and P. Bai, "An improved algorithm based on the gvf-snake for effective concavity edge detection," *Software Engineering and Applications*, 2013.

[42] S. T. Acton and N. Ray, "Biomedical image analysis: segmentation," *Synthesis Lectures on Image, Video, and Multimedia Processing*, vol. 4, no. 1, pp. 1–108, 2009.

[43] L. Qin, C. Zhu, Y. Zhao, H. Bai, and H. Tian, "Generalized gradient vector flow for snakes: New observations, analysis and improvement," *IEEE Transactions on Circuits and System for Video Technology*, vol. 23, no. 5, pp. 883–897, 2013.

[44] Y. Yao, L. Liu, L. Liao, M. Wei, J. Guo, and Y. Li, "Sigmoid gradient vector flow for medical image segmentation," in *11th International Conference on Signal Processing (ICSP)*, vol. 2. IEEE, 2012, pp. 881–884.

[45] Y. Wang, Y. Wu, and Y. Jia, "Shape constraints for the left ventricle segmentation from cardiac cine mri based on snake models," in *Medical Image Analysis in Shape Analysis*, vol. 14. Springer, 2014, pp. 373–412.

[46] J. Montagnat, H. Delingette, and N. Ayache, "A review of deformable surfaces: topology, geometry and deformation," *Image and vision computing*, vol. 19, no. 14, pp. 1023–1040, 2001.

[47] T. McInemey and D. Terzopoulos, "Topology adaptive deformable surfaces for medical image volume segmentation," *IEEE transactions on medical imaging*, vol. 18, no. 10, pp. 840–850, 1999.

[48] V. Caselles, R. Kimmel, and G. Sapiro, "Geodesic active contours," *International Journal of Computer Vision*, vol. 22, no. 1, pp. 61–79, 1997.

[49] S. Osher and J. A. Sethian, "Fronts propagating with curvature-dependent speed: algorithms based on hamilton-jacobi formulations," *Journal of Computational Physics*, vol. 79, no. 1, pp. 12–49, 1988.

[50] R. Malladi, J. A. Sethian, and B. C. Vemuri, "Shape modeling with front propagation: A level set approach," *IEEE Transactions on Pattern Analysis and Machine Intelligence*, vol. 17, no. 2, pp. 158–175, 1995.

[51] E. Niemi, M. Lassas, A. Kallonen, L. Harhanen, K. Hämäläinen, and S. Siltanen, "Dynamic multi-source x-ray tomography using a spacetime level set method," *Journal of Computational Physics*, vol. 291, pp. 218–237, 2015.

[52] R. Fedkiw and S. Osher, "Level set methods and dynamic implicit surfaces," *Surfaces*, vol. 44, p. 77, 2002.

[53] J. A. Sethian, "Tracking interfaces with level sets: An" act of violence" helps solve evolving interface problems in geometry, fluid mechanics, robotic navigation and materials sciences," *American Scientist*, vol. 85, no. 3, pp. 254–263, 1997.

[54] ——, *Level set methods and fast marching methods: evolving interfaces in computational geometry, fluid mechanics, computer vision, and materials science*. Cambridge university press, 1999, vol. 3.

[55] T. F. Chan and L. A. Vese, "Active contours without edges," *IEEE Transactions on image processing*, vol. 10, no. 2, pp. 266–277, 2001.

[56] H.-K. Zhao, T. Chan, B. Merriman, and S. Osher, "A variational level set approach to multiphase motion," *Journal of computational physics*, vol. 127, no. 1, pp. 179–195, 1996.

[57] L. C. Evans and R. F. Gariepy, *Measure theory and fine properties of functions*. CRC press, 2015.

[58] R. Malladi and J. A. Sethian, "Image processing via level set curvature flow," *proceedings of the National Academy of sciences*, vol. 92, no. 15, pp. 7046–7050, 1995.

[59] F. S. Cohen and Z. Fan, "Maximum likelihood unsupervised textured image segmentation," *CVGIP: Graphical models and image processing*, vol. 54, no. 3, pp. 239–251, 1992.

[60] D. Peng, B. Merriman, S. Osher, H. Zhao, and M. Kang, "A PDE-based fast local level set method," *Journal of Computational Physics*, vol. 155, no. 2, pp. 410–438, 1999.

[61] C. Li, C. Xu, C. Gui, and M. D. Fox, "Level set evolution without re-initialization: a new variational formulation," in *Proceedings of IEEE Computer Society Conference on Computer Vision and Pattern Recognition*, vol. 1. IEEE, 2005, pp. 430–436.

[62] J. Weickert and G. Kühne, *Fast methods for implicit active contour models*. Springer, 2003.

[63] B. Vemuri and Y. Chen, "Joint image registration and segmentation," in *Geometric level set methods in imaging, vision, and graphics*. Springer, 2003, pp. 251–269.

[64] A. Belaid, D. Boukerroui, Y. Maingourd, and J.-F. Lerallut, "Phase-based level set segmentation of ultrasound images," *Information Technology in Biomedicine, IEEE Transactions on*, vol. 15, no. 1, pp. 138–147, 2011.

[65] R. Kimmel and A. Bruckstein, "On edge detection, edge integration and geometric active contours," in *Proceedings of ISMM*, vol. 3, 2002, pp. 37–45.

[66] R. Kimmel and A. M. Bruckstein, "Regularized laplacian zero crossings as optimal edge integrators," *International Journal of Computer Vision*, vol. 53, no. 3, pp. 225–243, 2003.

[67] R. Kimmel, "Fast edge integration," in *Geometric Level Set Methods in Imaging, Vision, and Graphics*. Springer, 2003, pp. 59–77.

[68] A. Vasilevskiy and K. Siddiqi, "Flux maximizing geometric flows," *IEEE Transactions on Pattern Analysis and Machine Intelligence*, vol. 24, no. 12, pp. 1565–1578, 2002.

[69] V. Estellers, D. Zosso, X. Bresson, and J.-P. Thiran, "Harmonic active contours," *IEEE Transactions on Image Processing*, vol. 23, no. 1, pp. 69–82, 2014.

[70] K. Zhang, L. Zhang, H. Song, and D. Zhang, "Reinitialization-free level set evolution via reaction diffusion," *IEEE Transactions on Image Processing*, vol. 22, no. 1, pp. 258–271, 2013.

[71] W. Wang, L. Zhu, J. Qin, Y.-P. Chui, B. N. Li, and P.-A. Heng, "Multiscale geodesic active contours for ultrasound image segmentation using speckle reducing anisotropic diffusion," *Optics and Lasers in Engineering*, vol. 54, pp. 105–116, 2014.

[72] M. M. Abdelsamea, G. Gnecco, and M. M. Gaber, "An efficient self-organizing active contour model for image segmentation," *Neurocomputing*, vol. 149, no. 9, pp. 820–835, 2014.

[73] Y. Zhou, W.-R. Shi, W. Chen, Y.-l. Chen, Y. Li, L.-W. Tan, and D.-Q. Chen, "Active contours driven by localizing region and edge-based intensity fitting energy with application to segmentation of the left ventricle in cardiac ct images," *Neurocomputing*, vol. 156, pp. 199–210, 2015.

[74] Z. Ji, Y. Xia, Q. Sun, G. Cao, and Q. Chen, "Active contours driven by local likelihood image fitting energy for image segmentation," *Information Sciences*, vol. 301, pp. 285–304, 2015.

[75] H. Greenspan, B. van Ginneken, and R. M. Summers, "Guest editorial deep learning in medical imaging: Overview and future promise of an exciting new technique," *IEEE Transactions on Medical Imaging*, vol. 35, no. 5, pp. 1153–1159, 2016.

[76] Y. LeCun, Y. Bengio, and G. Hinton, "Deep learning," *Nature*, vol. 521, no. 7553, pp. 436–444, 2015.

[77] F. C. Ghesu, E. Krubasik, B. Georgescu, V. Singh, Y. Zheng, J. Hornegger, and D. Comaniciu, "Marginal space deep learning: efficient architecture for volumetric image parsing," *IEEE transactions on medical imaging*, vol. 35, no. 5, pp. 1217–1228, 2016.

[78] T. Brosch, L. Y. Tang, Y. Yoo, D. K. Li, A. Traboulsee, and R. Tam, "Deep 3d convolutional encoder networks with shortcuts for multiscale feature integration applied to multiple sclerosis lesion segmentation," *IEEE transactions on medical imaging*, vol. 35, no. 5, pp. 1229–1239, 2016.

[79] S. Pereira, A. Pinto, V. Alves, and C. A. Silva, "Brain tumor segmentation using convolutional neural networks in mri images," *IEEE transactions on medical imaging*, vol. 35, no. 5, pp. 1240–1251, 2016.

[80] M. Kallenberg, K. Petersen, M. Nielsen, A. Y. Ng, P. Diao, C. Igel, C. M. Vachon, K. Holland, R. R. Winkel, N. Karssemeijer, *et al.*, "Unsupervised deep learning applied to breast density segmentation and mammographic risk scoring," *IEEE transactions on medical imaging*, vol. 35, no. 5, pp. 1322–1331, 2016.

[81] A. Hoogi, A. Subramaniam, R. Veerapaneni, and D. Rubin, "Adaptive estimation of active contour parameters using convolutional neural networks and texture analysis," *IEEE Transactions on Medical Imaging*, 2016.

[82] C. Rupprecht, E. Huaroc, M. Baust, and N. Navab, "Deep active contours," *Computer Vision and Pattern Recognition*, 2016.

[83] T. A. Ngo, Z. Lu, and G. Carneiro, "Combining deep learning and level set for the automated segmentation of the left ventricle of the heart from cardiac cine magnetic resonance," *Medical Image Analysis*, 2016.

[84] P. Kainz, M. Pfeiffer, and M. Urschler, "Semantic segmentation of colon glands with deep convolutional neural networks and total variation segmentation," *Computer Vision and Pattern Recognition*, 2015.

[85] V. Hadziavdic, "A comparative study of active contour models for boundary detection in brain images," *Diploma Project of Faculty for Mathematical and Natural Sciences University of Tromso (URL: http://www. uib. no/med/avd/miapr/arvid/vedad_diploma. pdf)*, 1999.

[86] B. Li and S. T. Acton, "Active contour external force using vector field convolution for image segmentation," *Image Processing, IEEE Transactions on*, vol. 16, no. 8, pp. 2096–2106, 2007.

[87] J. L. Prince and C. Xu, "A new external force model for snakes," in *Proc. 1996 Image and Multidimensional Signal Processing Workshop*, vol. 3, no. 31. Citeseer, 1996, p. 1.

[88] Y. Wang and J. Yang, "Gradient vector flow snake with embedded edge confidence," in *Pacific Rim International Conference on Artificial Intelligence*. Springer, 2004, pp. 778–786.

[89] G. Xingfei and T. Jie, "An automatic active contour model for multiple objects," in *Pattern Recognition, 2002. Proceedings. 16th International Conference on*, vol. 2. IEEE, 2002, pp. 881–884.

[90] B. Li and S. T. Acton, "Automatic active model initialization via poisson inverse gradient," *IEEE Transactions on Image Processing*, vol. 17, no. 8, pp. 1406–1420, 2008.

[91] T. Xu, M. Mandal, R. Long, I. Cheng, and A. Basu, "An edge-region force guided active shape approach for automatic lung field detection in chest radiographs," *Computerized Medical Imaging and Graphics*, vol. 36, no. 6, pp. 452–463, 2012.

[92] G. P. Nason and B. W. Silverman, "The stationary wavelet transform and some statistical applications," in *Wavelets and statistics*. Springer, 1995, pp. 281–299.

[93] V. Sanchez, R. Abugharbieh, and P. Nasiopoulos, "3d scalable medical image compression with optimized volume of interest coding," *IEEE Transactions on Medical Imaging*, vol. 29, no. 10, pp. 1808–1820, 2010.

[94] L. M. Lorigo, O. Faugeras, W. E. L. Grimson, R. Keriven, and R. Kikinis, "Segmentation of bone in clinical knee mri using texture-based geodesic active contours," in *International Conference on Medical Image Computing and Computer-Assisted Intervention*. Springer, 1998, pp. 1195–1204.

[95] A. Dima, M. Scholz, and K. Obermayer, "Automatic segmentation and skeletonization of neurons from confocal microscopy images based on the 3-d wavelet transform," *IEEE Transactions on Image Processing*, vol. 11, no. 7, pp. 790–801, 2002.

[96] J. E. Fowler, "The redundant discrete wavelet transform and additive noise," *IEEE on Signal Processing Letters*, vol. 12, no. 9, pp. 629–632, 2005.

[97] L. R. Dice, "Measures of the amount of ecologic association between species," *Ecology*, vol. 26, no. 3, pp. 297–302, 1945.

[98] P. Jaccard, *Distribution de la Flore Alpine: dans le Bassin des dranses et dans quelques régions voisines.* Rouge, 1901.

[99] S. Lankton and A. Tannenbaum, "Localizing region-based active contours," *IEEE Transactions on Image Processing*, vol. 17, no. 11, pp. 2029–2039, 2008.

[100] M. Jung, G. Peyré, and L. D. Cohen, "Nonlocal active contours," *SIAM Journal on Imaging Sciences*, vol. 5, no. 3, pp. 1022–1054, 2012.

[101] X. Xie, "Active contouring based on gradient vector interaction and constrained level set diffusion," *IEEE Transactions on Image Processing*, vol. 19, no. 1, pp. 154–164, 2010.

[102] A. Faisal and C. Pluempitiwiriyawej, "Active contour using local region-scalable force with expandable kernel," in *International Conference on Information Science and Technology (ICIST).* IEEE, 2012, pp. 18–24.

[103] C. Li, C. Xu, C. Gui, and M. D. Fox, "Distance regularized level set evolution and its application to image segmentation," *IEEE Transactions on Image Processing*, vol. 19, no. 12, pp. 3243–3254, 2010.

[104] M. Sussman, P. Smereka, and S. Osher, "A level set approach for computing solutions to incompressible two-phase flow," *Journal of Computational Physics*, vol. 114, no. 1, pp. 146–159, 1994.

[105] C. Yu, W. Zhang, Y. Yu, and Y. Li, "A novel active contour model for image segmentation using distance regularization term," *Computers & Mathematics with Applications*, vol. 65, no. 11, pp. 1746–1759, 2013.

[106] K. B. Prakash, S. Zhou, T. C. Morgan, D. F. Hanley, and W. L. Nowinski, "Segmentation and quantification of intra-ventricular/cerebral hemorrhage in

CT scans by modified distance regularized level set evolution technique," *International journal of computer assisted radiology and surgery*, vol. 7, no. 5, pp. 785–798, 2012.

[107] A. Khadidos, V. Sanchez, and C.-T. Li, "Active contours based on weighted gradient vector flow and balloon forces for medical image segmentation," in *IEEE International Conference on Image Processing*. IEEE, 2014, pp. 902–906.

[108] G. Aubert and P. Kornprobst, "Mathematical problems in image processing: Partial differential equations and the calculus of variations," *Applied Mathematical Sciences*, 2002.

[109] W. H. O. R. Health, W. H. O. C. Diseases, and H. Promotion, *Comprehensive cervical cancer control: a guide to essential practice*. World Health Organization, 2006.

[110] Z. Lu, G. Carneiro, and A. P. Bradley, "An improved joint optimization of multiple level set functions for the segmentation of overlapping cervical cells," *IEEE Transactions on Image Processing*, vol. 24, no. 4, pp. 1261–1272, 2015.

[111] H. Z. Noorani, C. Arratoon, A. Hall, C. C. O. for Health Technology Assessment, *et al.*, *Assessment of techniques for cervical cancer screening*, 1997.

[112] E. Bengtsson, "Recognizing signs of malignancy - the quest for computer assisted cancer screening and diagnosis systems," in *Computational Intelligence and Computing Research (ICCIC), 2010 IEEE International Conference on*. IEEE, 2010, pp. 1–6.

[113] B. Ewert, "Computerized cell image analysis- past, present, and future," in *Scandinavian Conference on Image Analysis*. Springer, 2003, pp. 395–407.

[114] I. Dagher and K. El Tom, "Waterballoons: A hybrid watershed balloon snake segmentation," *Image and Vision Computing*, vol. 26, no. 7, pp. 905–912, 2008.

[115] C. Jung, C. Kim, S. W. Chae, and S. Oh, "Unsupervised segmentation of overlapped nuclei using bayesian classification," *IEEE Transactions on Biomedical Engineering*, vol. 57, no. 12, pp. 2825–2832, 2010.

[116] A. Kale and S. Aksoy, "Segmentation of cervical cell images," in *International Conference on Pattern Recognition (ICPR)*. IEEE, 2010, pp. 2399–2402.

[117] K. Li, Z. Lu, W. Liu, and J. Yin, "Cytoplasm and nucleus segmentation in cervical smear images using radiating gvf snake," *Pattern Recognition*, vol. 45, no. 4, pp. 1255–1264, 2012.

[118] M. E. Plissiti, C. Nikou, and A. Charchanti, "Automated detection of cell nuclei in pap smear images using morphological reconstruction and clustering," *IEEE Transactions on Information Technology in Biomedicine*, vol. 15, no. 2, pp. 233–241, 2011.

[119] S.-F. Yang-Mao, Y.-K. Chan, and Y.-P. Chu, "Edge enhancement nucleus and cytoplast contour detector of cervical smear images," *, IEEE Transactions on Systems, Man, and Cybernetics, Part B: Cybernetics*, vol. 38, no. 2, pp. 353–366, 2008.

[120] P. Bamford and B. Lovell, "Unsupervised cell nucleus segmentation with active contours," *Signal Processing*, vol. 71, no. 2, pp. 203–213, 1998.

[121] M. E. Plissiti, C. Nikou, and A. Charchanti, "Combining shape, texture and intensity features for cell nuclei extraction in pap smear images," *Pattern Recognition Letters*, vol. 32, no. 6, pp. 838–853, 2011.

[122] A. N. Basavanhally, S. Ganesan, S. Agner, J. P. Monaco, M. D. Feldman, J. E. Tomaszewski, G. Bhanot, and A. Madabhushi, "Computerized image-based detection and grading of lymphocytic infiltration in her2+ breast cancer histopathology," *IEEE Transactions on Biomedical Engineering*, vol. 57, no. 3, pp. 642–653, 2010.

[123] C. Fatichah, N. Suciati, B. Amaliah, and N. Aini, "Nuclei segmentation of microscopic breast cancer image using gram-schmidt and cluster validation algorithm," in *2015 IEEE International Conference on Control System, Computing and Engineering (ICCSCE)*. IEEE, 2015, pp. 236–241.

[124] V. S. Prasath, K. Fukuma, B. J. Aronow, and H. Kawanaka, "Cell nuclei segmentation in glioma histopathology images with color decomposition based active contours," in *Bioinformatics and Biomedicine (BIBM), 2015 IEEE International Conference on*. IEEE, 2015, pp. 1734–1736.

[125] H. Xu, C. Lu, and M. Mandal, "An efficient technique for nuclei segmentation based on ellipse descriptor analysis and improved seed detection algorithm," *IEEE journal of biomedical and health informatics*, vol. 18, no. 5, pp. 1729–1741, 2014.

[126] Y. Marinakis, G. Dounias, and J. Jantzen, "Pap smear diagnosis using a hybrid intelligent scheme focusing on genetic algorithm based feature selection and nearest neighbor classification," *Computers in Biology and Medicine*, vol. 39, no. 1, pp. 69–78, 2009.

[127] H.-S. Wu, J. Barba, and J. Gil, "A parametric fitting algorithm for segmentation of cell images," *IEEE Transactions on Biomedical Engineering*, vol. 45, no. 3, pp. 400–407, 1998.

[128] M.-H. Tsai, Y.-K. Chan, Z.-Z. Lin, S.-F. Yang-Mao, and P.-C. Huang, "Nucleus and cytoplast contour detector of cervical smear image," *Pattern Recognition Letters*, vol. 29, no. 9, pp. 1441–1453, 2008.

[129] N. M. Harandi, S. Sadri, N. A. Moghaddam, and R. Amirfattahi, "An automated method for segmentation of epithelial cervical cells in images of thinprep," *Journal of medical systems*, vol. 34, no. 6, pp. 1043–1058, 2010.

[130] A. Gençtav, S. Aksoy, and S. Önder, "Unsupervised segmentation and classification of cervical cell images," *Pattern Recognition*, vol. 45, no. 12, pp. 4151–4168, 2012.

[131] L. Zhang, H. Kong, C. T. Chin, S. Liu, Z. Chen, T. Wang, and S. Chen, "Segmentation of cytoplasm and nuclei of abnormal cells in cervical cytology using global and local graph cuts," *Computerized Medical Imaging and Graphics*, vol. 38, no. 5, pp. 369–380, 2014.

[132] N. Beliz-Osorio, J. Crespo, M. Garcia-Rojo, A. Munoz, and J. Azpiazu, "Cytology imaging segmentation using the locally constrained watershed transform," in *Mathematical Morphology and Its Applications to Image and Signal Processing*. Springer, 2011, pp. 429–438.

[133] Z. Lu, G. Carneiro, and A. P. Bradley, "Automated nucleus and cytoplasm segmentation of overlapping cervical cells," in *Medical Image Computing and Computer-Assisted Intervention (MICCAI)*. Springer, 2013, pp. 452–460.

[134] M. S. Nosrati and G. Hamarneh, "Segmentation of overlapping cervical cells: a variational method with star-shape prior," in *IEEE 12th International Symposium on Biomedical Imaging (ISBI)*. IEEE, 2015, pp. 186–189.

[135] J. Matas, O. Chum, M. Urban, and T. Pajdla, "Robust wide-baseline stereo from maximally stable extremal regions," *Image and vision computing*, vol. 22, no. 10, pp. 761–767, 2004.

[136] M. Nosrati and G. Hamarneh, "A variational approach for overlapping cell segmentation," *ISBI Overlapping Cervical Cytology Image Segmentation Challenge*, pp. 1–2, 2014.

[137] M. E. Plissiti and C. Nikou, "Overlapping cell nuclei segmentation using a spatially adaptive active physical model," *IEEE Transactions on Image Processing*, vol. 21, no. 11, pp. 4568–4580, 2012.

[138] Y. Y. Schechner, N. Kiryati, and R. Basri, "Separation of transparent layers using focus," *International Journal of Computer Vision*, vol. 39, no. 1, pp. 25–39, 2000.

[139] X. Bresson, S. Esedolu, P. Vandergheynst, J.-P. Thiran, and S. Osher, "Fast global minimization of the active contour/snake model," *Journal of Mathematical Imaging and Vision*, vol. 28, no. 2, pp. 151–167, 2007.

[140] A. P. Bradley and P. C. Bamford, "A one-pass extended depth of field algorithm based on the over-complete discrete wavelet transform," in *Image and Vision Computing'04 New Zealand (IVCNZ'04)*, 2004, pp. 279–284.

[141] A. Vedaldi and S. Soatto, "Quick shift and kernel methods for mode seeking," in *Computer vision–ECCV 2008*. Springer, 2008, pp. 705–718.

[142] W. A. Barrett and E. N. Mortensen, "Interactive live-wire boundary extraction," *Medical image analysis*, vol. 1, no. 4, pp. 331–341, 1997.

[143] J. W. Bishop, S. H. Bigner, T. J. Colgan, M. Husain, L. P. Howell, K. M. McIntosh, D. A. Taylor, and M. H. Sadeghi, "Multicenter masked evaluation of autocyte prep thin layers with matched conventional smears," *Acta cytologica*, vol. 42, no. 1, pp. 189–197, 1998.

[144] P. Radau, Y. Lu, K. Connelly, G. Paul, A. Dick, and G. Wright, "Evaluation framework for algorithms segmenting short axis cardiac mri," *The MIDAS Journal*, vol. 49, no. 6, 2009.